

Titre:	Sonde Raman multimodale intégrée à une plateforme d'imagerie TRUS-IRM à l'aide d'un capteur électromagnétique pour améliorer le guidage des biopsies de la prostate
Auteur:	Fabien Picot
Date:	2022
Type:	Mémoire ou thèse / Dissertation or Thesis
Référence:	Picot, F. (2022). Sonde Raman multimodale intégrée à une plateforme d'imagerie TRUS-IRM à l'aide d'un capteur électromagnétique pour améliorer le guidage des biopsies de la prostate [Thèse de doctorat, Polytechnique Montréal]. PolyPublie. https://publications.polymtl.ca/10493/
Citation:	

Document en libre accès dans PolyPublie

Open Access document in PolyPublie

URL de PolyPublie: <https://publications.polymtl.ca/10493/>
PolyPublie URL:

Directeurs de recherche: Frédéric Leblond, & Samuel Kadoury
Advisors:

Programme: Génie biomédical
Program:

POLYTECHNIQUE MONTRÉAL

affiliée à l'Université de Montréal

**Sonde Raman multimodale intégrée à une plateforme d'imagerie TRUS-IRM
à l'aide d'un capteur Électromagnétique pour améliorer le guidage des
biopsies de la prostate**

FABIEN PICOT

Institut de génie biomédical

Thèse présentée en vue de l'obtention du diplôme de *Philosophiae Doctor*

Génie biomédical

Août 2022

POLYTECHNIQUE MONTRÉAL

affiliée à l'Université de Montréal

Cette thèse intitulée :

**Sonde Raman multimodale intégrée à une plateforme d'imagerie TRUS-IRM
à l'aide d'un capteur Électromagnétique pour améliorer le guidage des
biopsies de la prostate**

présentée par **Fabien PICOT**

en vue de l'obtention du diplôme de *Philosophiae Doctor*

a été dûment acceptée par le jury d'examen constitué de :

Stephan REUTER, président

Frédéric LEBLOND, membre et directeur de recherche

Samuel KADOURY, membre et codirecteur de recherche

Lucien WEISS, membre

Daniel CÔTÉ, membre externe

DÉDICACE

À mes parents.

REMERCIEMENTS

L'institution Universitaire est le haut-lieu de la recherche scientifique. Au cours de ces dernières années, elle fut aussi pour moi un espace de sociabilité unique où j'ai cotoyé des gens d'exception dont l'influence sur mon doctorat ne saurait être résumée dans une section aussi succincte. Je souhaite exprimer avec ces quelques paragraphes toute la gratitude que je leur dois.

Mon directeur de recherche, le professeur Frédéric Leblond, est la première de ces personnes. En plus de son expérience et sa rigueur scientifique, Frédéric fait invariablement preuve de qualités humaines dans sa direction du LRO. C'est son soutien indéfectible qui m'a permis de faire face avec confiance à chacun des défis majeurs posés par mon doctorat. L'exigence de qualité et de sérieux du travail réalisé sous sa tutelle ne sont en rien des freins à son enthousiasme, et je conserve chacun des bons mots échangés avec lui, comme de précieux souvenirs. Mon deuxième remerciement s'adresse à mon codirecteur, le professeur Samuel Kadoury, et à la Dre Cynthia Ménard. Le chemin emprunté pour tester un système optique en salle opératoire est semé d'embûches. Les difficultés ne sont pas toutes d'ordre scientifique et je ne remercierai jamais assez leur implication et leur soutien qui m'ont permis de les franchir, multipliant l'originalité et l'impact des résultats de ma thèse.

Depuis mon arrivée dans le LRO, j'ai eu le plaisir d'échanger avec de nombreux chercheurs, certains désormais ex-collègues. Je tiens tout particulièrement à remercier mon ami Guillaume Sheehy, qui m'a fait découvrir entre autres le plaisir des bières québecquoises et des whisky de qualité! Je veux remercier aussi spécifiquement pour les travaux et bon moments passés ensemble : Audrey Laurence, Catherine St-Pierre, Tien Nguyen, Émile Beaulieu et Francois Daoust. Je remercie tous les membres du LRO et souhaite témoigner que faire partie de l'équipe avec eux est un privilège. L'accomplissement d'une étude clinique dans le cadre de mon doctorat a nécessité un travail préparatoire de longue haleine. Je dois un remerciement spécial à Roozbeh Shams et David Grajales pour leur dévouement et toutes nos heures dépensées sans compter au département de radio-oncologie du CHUM. Le remerciement est double pour Mirela Birlea et son opiniâtreté dans l'obtention des échantillons, indispensables à l'étude, auprès des pathologistes du CHUM.

À tous mes amis du club Judo Monde, je vous salue et vous remercie pour la passion de ce sport que vous m'avez transmise. Aucune pandémie ne saurait désormais m'empêcher définitivement de retourner sur le tatami. Enfin je veux remercier mes proches dont mes parents Vincent et Muriel, mon grand frère Florian, mes grands-parents Jean-Paul et Colette ainsi que tous mes amis qui n'ont jamais douté de moi et m'ont toujours soutenu.

RÉSUMÉ

La substitution des chirurgies ouvertes par des procédures minimalement invasives constitue une évolution majeure de la médecine moderne. Ce progrès est rendu possible par le développement des systèmes d'imagerie servant à guider en temps réel la navigation des instruments chirurgicaux. Toutefois ces technologies, basées essentiellement sur un contraste anatomique, souffrent de limites de précision dues à la taille ou à l'hétérogénéité des lésions ciblées. Cette thèse vise à répondre à ce problème clinique, dans le cas particulier du guidage des procédures de biopsie de la prostate, grâce au contraste moléculaire que procure la spectroscopie Raman. Le premier objectif est la validation d'une preuve de concept du guidage d'une aiguille de biopsie optique, lors de son insertion dans un modèle animal *in vivo*. Les résultats ont montré la capacité de la sonde tomographique, basée sur la spectroscopie de réflectance diffuse, à retrouver la signature de l'hémoglobine permettant de localiser spatialement les vaisseaux sanguins. Le deuxième objectif vise à concevoir et manufacturer le nouveau prototype de sonde multimodale optimisé pour le guidage de la procédure de biopsie de la prostate. Les contraintes techniques sont majeures car elles imposent de miniaturiser, dans un diamètre inférieur à 1.3 mm, un système de spectroscopie Raman combinant les régions *fingerprint* (FP) et *high wavenumber* (HWN). Un aspect critique est également l'intégration d'un capteur Électromagnétique (EM) sur le nouveau prototype permettant son insertion dans une plateforme de guidage standard TRUS-IRM. Finalement le troisième objectif est de valider la capacité de la spectroscopie Raman à discriminer entre les tissus sains et cancéreux de la prostate. Nous démontrons pour la première fois l'utilisation et le diagnostic *in situ* de tissus cancéreux prostatiques sur 18 patients, avec une précision de 79%, à l'aide d'un système de spectroscopie Raman intégré à une plateforme de navigation TRUS-IRM-EM. Les résultats de cette thèse valident expérimentalement la capacité de la spectroscopie Raman à améliorer le guidage des procédures de biopsie de la prostate en détectant *in situ* les échantillons cancéreux.

ABSTRACT

The transition from open to minimally invasive surgeries represents a major evolution of modern medicine. This improvement is possible thanks to the development of imaging systems, used in real time, for the surgical instruments guidance. However, these technologies, mostly based on anatomical contrast, suffer from accuracy limitations due to the size and heterogeneity of the targeted lesions. This thesis aims to answer the specific clinical problem of the prostate biopsy procedure guidance, by using the molecular contrast provided by Raman spectroscopy. The first objective is to provide a proof of concept for the guidance of an optical biopsy needle, during its insertion in an animal model experiment. The results showed the ability of the tomographic probe, based on diffuse reflectance spectroscopy, to retrieve the hemoglobin signature allowing to spatially locate blood vessels. The second objective is to design and manufacture a new multimodal prototype probe optimized for the prostate procedure biopsy guidance. The technical constraints are significant due to the requirement of miniaturizing, in a 1.3 mm diameter, a Raman spectroscopy system combining fingerprint and high wavenumber spectral regions. A critical aspect is also the Electromagnetic tracker integration on this new prototype to ensure its clean insertion in a standard TRUS-MRI navigation platform. Finally, the third objective is the validation of Raman spectroscopy to discriminate between normal and cancerous prostate tissue. We show for the first time the *in situ* acquisition and diagnosis of cancerous prostate tissue performed on 18 patients, with a 79% accuracy, using our Raman spectroscopy system integrated to a TRUS-MRI-EM navigation platform. The results of this thesis experimentally validate the ability of Raman spectroscopy to enhance the prostate procedure biopsy guidance thanks to an *in situ* detection of cancerous samples.

TABLE DES MATIÈRES

DÉDICACE.....	III
REMERCIEMENTS	IV
RÉSUMÉ.....	VI
ABSTRACT	VII
TABLE DES MATIÈRES	VIII
LISTE DES TABLEAUX.....	XII
LISTE DES FIGURES	XIII
LISTE DES SIGLES ET ABRÉVIATIONS	XVII
LISTE DES ANNEXES	XXI
CHAPITRE 1 INTRODUCTION.....	1
1.1 Mise en contexte.....	1
1.2 Le cancer de la prostate : diagnostic et traitements.....	2
1.3 La procédure de biopsie de la prostate et ses limites	3
1.4 Solution proposée.....	6
1.5 Hypothèses et objectifs du projet	6
CHAPITRE 2 REVUE DE LITTÉRATURE	9
2.1 Spectroscopie par Réflectance Diffuse	9
2.2 Spectroscopie de Fluorescence/Autofluorescence	13
2.3 Spectroscopie Raman	15
2.3.1 Diffusion Raman dans les tissus biologiques.....	15
2.3.2 Applications de la spectroscopie Raman en oncologie	18
2.4 Guidage optique multimodal des biopsies de la prostate	21

CHAPITRE 3 DÉMARCHE SCIENTIFIQUE ET CONTRIBUTIONS	23
3.1 Étude préliminaire sur l'utilisation d'une aiguille optique pour la procédure de biopsie	23
3.2 Conception d'un nouveau prototype de sonde multimodale et évaluation de la stratégie d'acquisition des ensembles de données d'apprentissage	24
3.3 Étude clinique en salle opératoire au CHUM.....	27
CHAPITRE 4 ARTICLE 1: INTERSTITIAL IMAGING WITH MULTIPLE DIFFUSIVE REFLECTANCE SPECTROSCOPY PROJECTIONS FOR <i>IN VIVO</i> BLOOD VESSELS DETECTION DURING BRAIN NEEDLE BIOPSY PROCEDURES.....	30
4.1 Abstract	30
4.2 Introduction	30
4.3 Methods.....	33
4.3.1 Imaging system	33
4.3.2 Tissue phantom experiments	36
4.3.3 Optical reconstruction algorithm.....	36
4.3.4 <i>In vivo</i> data acquisition protocol	38
4.4 Results	40
4.4.1 Tissue phantom experiment	40
4.4.2 <i>In vivo</i> experiment.....	41
4.5 Discussion	44
4.6 Conclusion.....	46
4.7 Disclosures	46
4.8 Acknowledgments	47
CHAPITRE 5 ARTICLE 2: DATA CONSISTENCY AND CLASSIFICATION MODEL TRANSFERABILITY ACROSS BIOMEDICAL RAMAN SPECTROSCOPY SYSTEMS	48

5.1	Abstract	48
5.2	Introduction	48
5.3	Methods.....	50
5.3.1	Imaging systems and acquisition protocol	50
5.3.2	Tissue phantom experiment	53
5.3.3	<i>Ex vivo</i> experiment.....	53
5.3.4	Spectral data processing and statistical analysis	54
5.3.5	Quantification of the intra-system and inter-system variability	56
5.3.6	Quantitative evaluation of model transferability in monkey brain experiment	57
5.4	Results	58
5.4.1	Quantitative comparison between systems	58
5.4.2	Quantitative evaluation of model transferability in <i>ex vivo</i> experiment	60
5.5	Discussion	63
5.6	Conclusion.....	64
5.7	Acknowledgments.....	65
5.8	Conflict of interest.....	65
5.9	Data availability statement.....	65
CHAPITRE 6	ARTICLE 3: IMAGE-GUIDED RAMAN SPECTROSCOPY NAVIGATION SYSTEM TO IMPROVE TRANSPERINEAL PROSTATE CANCER DETECTION. PART 1: RAMAN SPECTROSCOPY FIBER-OPTICS SYSTEM AND <i>IN SITU</i> TISSUE CHARACTERIZATION	66
6.1	Abstract	66
6.2	Introduction	67
6.3	Methods.....	69
6.3.1	Raman system and calibration processing	69

6.3.2 Navigation system.....	70
6.3.3 Patient selection.....	71
6.3.4 Specimen handling and <i>ex vivo</i> measurements	72
6.3.5 Prostate slice reconstruction and registration with optical measurements	73
6.3.6 Surgical workflow and <i>in vivo</i> measurements.....	74
6.3.7 Data processing and machine learning workflow	75
6.4 Results	77
6.4.1 Spectroscopic measurements.....	77
6.4.2 Machine learning detection models.....	79
6.5 Discussion	81
6.6 Acknowledgments	83
6.7 Conflict of interest.....	83
6.8 Code, Data and Materials Availability	83
CHAPITRE 7 DISCUSSION GÉNÉRALE	84
7.1 Buts de l'étude.....	84
7.2 Validation de la spectroscopie Raman <i>in situ</i> pour le guidage des biopsies de la prostate	85
7.3 Développement d'un système multimodal	86
CHAPITRE 8 CONCLUSION ET RECOMMANDATIONS	88
RÉFÉRENCES	91
ANNEXES	114

LISTE DES TABLEAUX

Tableau 2.1 Principaux pics Raman dans les tissus de la prostate associés aux modes vibrationnels et molécules correspondantes [68], [95], [104], [121]	21
Table 5.1 Parameter differences between Raman wide-field system and point probe. systems.	54
Table 5.2 Raman band with molecular assignment, based on the literature, found in the current study on the monkey brain classification model [122], [189]–[191]......	55
Table 6.1 Clinical and pathological characteristics of the patients at radical prostatectomy and at biopsy procedure.	72

LISTE DES FIGURES

Figure 1.1 Schéma de (A) l'aiguille de biopsie de la prostate (Bard Medical, USA), (B) du canevas de guidage, et des étapes de la prise d'échantillon : (C) aiguille située sur la cible avec canules internes et externes rétractées, (D) canule interne relâchée et ouverture de la chambre de prélèvement, (E) canule externe relâchée et fermeture de la chambre de prélèvement.....	5
Figure 2.1 Géométrie de détection semi-infinie de la spectroscopie par réflectance diffuse et diagrammes de Jablonski pour les interactions lumière/matière d'absorption et de diffusion élastique.....	10
Figure 2.2 Spectre des Principaux absorbeurs (Hémoglobine) et spectres de diffusion de plusieurs tissus [46].	12
Figure 2.3 Géométrie de détection semi-infinie de la spectroscopie de fluorescence et diagrammes de Jablonski pour l'interaction lumière/matière de fluorescence.....	14
Figure 2.4 Géométrie de détection semi-infinie de la spectroscopie de Raman et diagrammes de Jablonski pour l'interaction Raman Stokes et Raman anti-Stokes.....	16
Figure 2.5 Illustration des régions spectrales <i>fingerprint</i> et <i>high wavenumber</i> d'un spectre Raman d'un échantillon biologique.....	17
Figure 3.1 Photographie de l'aiguille optique utilisée lors de l'expérience sur modèle porcin au CRCHUM. L'animal est installé sur une table chirurgicale avec un système de tomographie computationnelle (CT scan) utilisé comme étalon standard pour l'expérience.	23
Figure 3.2 Schéma du système optique multimodal pour le guidage des biopsies de la prostate (sonde, sources lumineuses et spectromètres) couplé au système de navigation chirurgical (plateforme guidage EM).	26
Figure 3.3 Photographie du prototype de sonde optique multimodal guidé, grâce à la plateforme TRUS-IRM-EM, lors d'une intervention de biopsie de la prostate sur un patient au CHUM.	28
Figure 4.1 Optical probe design showing the distribution of the optical fibers around the needle as well as the position of the mirror. Only the external cannula of the commercial needle is	

shown, with the optical fibers (in blue) disposed on its exterior surface: (a) transverse view and (b) longitudinal view of the optical needle shown in (c).....	34
Figure 4.2 (a) Schematics of the optical system showing the white-light source and the spectrometer connected to mechanical fiber switches allowing wide-angle interrogation when the needle is immersed in a tissue phantom composed of multiple inclusions (black carbon rods) embedded in a scattering medium (Intralipid TM). (b) Geometrical test configuration around the optical biopsy needle where each of the 9 potentially active fiber sources are identified with an even number while the 9 detection sources are identified with an odd number. Those numbers are associated with the numbering scheme used to identify the optical switches positions in (a).	35
Figure 4.3 Reconstructed diffuse optics images of carbon rods immersed in a diffusive medium. The distances (edge-to-edge) between the optical biopsy needle and inclusion 1 is: a) 0 mm, b) 0.5 mm, c) 1 mm, and d) 2 mm. The other carbon rod (inclusion 2) remained at the same position in all experiments.	40
Figure 4.4 Computed tomography (CT) scan used to locate blood vessels in the vicinity of the biopsy needle: (a) representation of blood vessels (red) surrounding the optical biopsy needle (grey tubular object), (b) 3D reconstruction of the surgical field in semi-transparence showing the needle (in grey), the swine skull (in brown) and the blood vessels (in white).	42
Figure 4.5 (a) Representative <i>in vivo</i> diffuse reflectance spectra and (b) optical sinogram associated with an interstitial measurement in swine brain.....	43
Figure 4.6 Comparison of spatially coincident images: (a) diffuse optical reconstructions, (b) CT scan (x- and y-axis units are in mm).	44
Figure 5.1 Three hand-held probes, one portable wide-field imaging instrument (labeled WF), three spectrometers and one 785 nm laser source were combined to build a total of 10 different Raman spectroscopy systems.	51
Figure 5.2 Quantitative comparison between point probe and wide field systems. Spectra comparison for point probe systems #1 to #9: A, raw spectra, B, processed Raman spectra, C, inter-system normalized root-mean-square deviation (NRMSD) for nylon features. Spectra	

comparison between point-probe system #1 and the wide-field system: D, raw spectra, E, processed Raman spectra, F, inter-system NRMSE for extracted features.	58
Figure 5.3 Classification model compatibility between the point probe systems and the wide-field imaging system. Average sensitivity, A, and specificity, B, of the classification model built with system #1 and tested on data acquired systems #2 to #9. The average and SD were calculated over 100 iterations of the machine learning workflow. C, Quality factor QF(n) depending on number of spectra per acquisition for systems #1 to #9. D, Quality factor QF(n) depending on number of spectra per acquisition for the two classes white/Gray matter. The average and SD were calculated over data measurements acquired per system, C, and per class, D.	60
Figure 5.4 <i>Ex vivo</i> classification experimental results. A, Raman map of white matter (white pixels) and gray matter (black pixels) acquired with the wide-field system (#WF) and classified with the model built using the training system #1. B, White light reflectance image of the monkey brain acquired with the wide-field system (#WF). C, Quality factor map. D, Average and SD white matter spectra for system #1 and the wide-field system. E, Average and deviation gray matter spectra for system #1 and the wide-field system. The average and SD were calculated over data measurements acquired for the white matter, D, and for gray matter, E.....	61
Figure 6.1 Schematic representation of the Raman probe obtaining measurements of the prostate through the guiding template, with a magnified view of the probe's tip. The probe is connected to the laser source and the spectrometer, which are controlled by a computer, and the optical system is combined with a TRUS system to perform the prostate biopsy procedure through the surgical guiding template. The computer displays the fused TRUS-MRI guiding image and the raw optical spectra after spectral acquisition for each site.	70
Figure 6.2 (a) Magnified view of the fresh prostate slice inside the guiding template for incremental Raman point measurements. (b) Four-step methodology for spatial registration of Raman measurements with labelled HPS tissue image reconstruction. Step 1 is a photograph of fresh prostate specimen; Step 2 is a photograph of the fresh prostate specimen through guiding template; Step 3 is HPS-labelled prostate image (cancer and normal tissue are labelled in blue and green, respectively); and Step 4 is the superimposed images of Step 2 and Step 3.....	73

Figure 6.3 <i>Ex vivo</i> dataset: average and standard deviation of processed spectra for each category (normal, cancer border, cancer) with all peaks used by the classification models labeled with their Raman shift in cm^{-1}	77
Figure 6.4 Average and standard deviation of processed spectra for normal and cancer <i>in vivo</i> spectra with all peaks used by the classification models labeled with their Raman shift in cm^{-1} . The <i>ex vivo</i> spectra from normal prostate are shown for comparison.	78
Figure 6.5 Receiver-operating characteristic (ROC) curve for discriminating normal from cancer prostatic tissue using Raman spectroscopy: (a) <i>ex vivo</i> model (b) <i>in vivo</i> model. List of Raman features associated with prostatic Raman-predicted molecular content that are used as inputs for the classification models: (c) <i>ex vivo</i> , (d) <i>in vivo</i> . Features with Raman band intensities higher in the cancer class are highlighted in gray. The molecular assignment of Raman peaks was based on literature findings [68], [95], [104], [190].	80

LISTE DES SIGLES ET ABRÉVIATIONS

ACS	American Cancer Society
ADN/DNA	Acide Désoxyribonucléique
APS/PSA	Anigène Prostatique Spécifique
ARN/RNA	Acide Ribonucléique
AUC	Area Under Curve
CARS	Coherent Anti-stokes Raman Spectroscopy
CCD	Charge Coupled Device
CHUM	Centre Hospitalier Universitaire de Montréal
CIHR	Canadian Institute of Health Research
CMOS	Complementary Metal Oxide Semi-conductor
CRCHUM	Centre de Recherche du Centre Hospitalier Universitaire de Montréal
CT	Tomographie Computationnelle
DOF	Degrees Of Freedom
EM	Electromagnétique
EMCCD	Electron Multiplying Charge Coupled device
FOV	Field oF View
FP	Fingerprint
FWHM	Full Width Half Maximum

GG	Grade Group
HPS	Hematoxylin Phloxine Saffron
ICG	Indocyanine Green
IRM/MRI	Imagerie par Résonnance Magnétique
HWN	High Wavenumber
LDA	Linear Discriminant Analysis
LED	Light-Emitting Diode
LOPOCV	Leave One Patient Out Cross Validation
LRO	Laboratory of Radiological Optics
MPE	Maximum Permissible Exposure
NIR	Near Infrared
NIST	National Institute of Standards and Technology
NRMSD	Normalized Root Mean Square Deviation
NSERC	Natural Sciences and Engineering Research Council of Canada
OCT	Optical Coherent Tomography
OH	Hydroxyl ion
pT	pathological Stage
PBS	Phosphate Buffered Saline
PCa	Prostate Cancer

PCA	Principal Component Analysis
PET	Positrons Emission Tomography
PLS-DA	Partial Least Square Discriminant Analysis
PpIX	Protoporphyrin IX
QF	Quality Factor
RF	Random Forest
ROC	Receiver Operating Characteristic
RP	Radical Prostatectomy
SD	Standard Deviation
SERS	Surface Enhanced Raman Spectroscopy
SF/FS	Spectroscopie de Fluorescence
SFDI	Spatial Frequency Domain Imaging
SNR	Signal to Noise Ratio
SRD/DRS	Spectroscopie de Réflectance Diffuse
SR/RS	Spectroscopie Raman
SRS	Spectroscopie Raman Stimulée
SORS	Spatially Offset Raman Spectroscopy
SVM	Support Vector Machine
TNM	Tumor Nodes Metastasis

TRUS Transrectal Ultrasons

US Ultrasons

UV Ultraviolet

WF Wide-Field

LISTE DES ANNEXES

Annexe A CURRICULUM VITAE.....114

CHAPITRE 1 INTRODUCTION

1.1 Mise en contexte

La chirurgie assistée par systèmes d'imagerie constitue une révolution dans le domaine médical. Elle permet le guidage des instruments chirurgicaux sans le recours à une chirurgie ouverte, lui substituant à la place des procédures minimalement invasives. Ce changement de paradigme conduit à éviter les risques de la chirurgie ouverte, pendant l'intervention et la convalescence, et augmente les chances de survie ainsi que la qualité de vie des patients.

Dans le cas des procédures de chirurgie liées à la prostate, les systèmes d'imagerie utilisés sont principalement l'ultrason (US) [1], [2], et la résonnance magnétique (IRM) [3]. À cause de l'encombrement qu'elle cause, l'IRM est souvent utilisée pour produire des images préopératoire. Ces images sont ensuite fusionnées avec l'imagerie ultrason, utilisée en temps réel pendant l'opération [4], [5], permettant ainsi de bénéficier de la qualité d'image supérieure de l'IRM. Cependant, ces technologies présentent plusieurs inconvénients majeurs. Tout d'abord elles exploitent majoritairement l'information structurelle des tissus ce qui limite leur sensibilité et spécificité. De plus, l'utilisation des images IRM préopératoires est limitée par les changements dynamiques qui surviennent entre l'acquisition des images et leur utilisation à des fins de guidage. En effet les mouvements viscéraux , attribués à la respiration ou au battements cardiaques, suffisent à déplacer la prostate dans le corps du patient. Le ciblage précis des lésions d'intérêts est donc compromis et le risque de prélever un échantillon non représentatif, dans le cas d'une biopsie de tumeur par exemple, est augmenté.

Afin de dépasser la limitation liée à l'information structurelle des tissus, il apparaît naturel de chercher à exploiter l'information liée au contraste moléculaire, entre les tissus sains et pathologiques, pour mieux guider les procédures diagnostiques et thérapeutiques. Ce type d'analyse, comme la génomique, est cependant coûteux et n'est en général pas accessible en temps réel. Des outils de guidage optiques sont développés depuis plusieurs années afin de répondre à cette problématique, avec une emphase particulière sur les applications oncologiques. Parmi ces techniques d'imagerie, les sondes interstitielles constituent une option de choix pour recouvrir ce contraste moléculaire. Elles sont compatibles avec le contexte de la chirurgie minimalement

invasive, et de par leur utilisation en temps réel elles permettent de s'affranchir du défaut de précision lié au mouvement des tissus.

Un état de l'art détaillant ces techniques optiques est inclus dans le chapitre 2 de cette thèse. Le projet de recherche de cette thèse s'appuie sur cette revue de littérature et se concentre sur la détection du cancer appliquée au guidage de la procédure de biopsie de la prostate.

1.2 Le cancer de la prostate : diagnostic et traitements

Au Canada, le cancer de la prostate représente 23.9% des nouveaux cas et 10.1% des décès par cancer [6]. Des chiffres similaires sont disponibles aux États-Unis, faisant de ce type de cancer le plus prévalant chez l'homme en Amérique du Nord [7]. Selon la Société Américaine du Cancer (ACS de American Cancer Society), il existe différents types de cancer de la prostate (e.g. carcinome à petites cellules, tumeurs neuroendocrines, sarcomes) mais l'adénocarcinome à lui seul concerne la quasi-totalité des cas [8]. Il s'agit d'une tumeur se développant à partir des cellules glandulaires qui sont responsables de la production du liquide prostatique contenu dans le sperme. Selon la classification du score de Gleason qui est la plus utilisée, l'adénocarcinome peut être classé en cinq groupes de grade (1 à 5) [9]. Cette classification se base sur le degré de différenciation des cellules cancéreuses ainsi que sur leur modèle de croissance. Les tumeurs de grades bas (grade 1) et intermédiaires (grades 2 et 3) sont moins agressives et leur modèle de développement et de propagation reste lent. À l'inverse, pour les tumeurs de grades élevés (grade 4 et 5) le cancer se développe rapidement et présente des cellules qui sont d'avantages différentes des cellules normales que pour les grades 1, 2 et 3. Les échantillons nécessaires à ce type d'évaluation histologique sont nécessairement obtenus par la chirurgie, biopsie ou prostatectomie.

Le diagnostic du type et du grade du cancer de la prostate est une étape critique dans la prise en charge médicale puisqu'il permet de déterminer le choix optimal de traitement. Des techniques de dépistage existent, allant du toucher rectal lors de l'examen physique aux tests de dosage des marqueurs tumoraux, mais aucune ne permet un diagnostic précoce fiable. Le test sanguin de l'Antigène Prostatique Spécifique (APS), bien que très utilisé, est très critiqué pour son manque de sensibilité et spécificité [10], [11], et la recherche de nouveaux marqueurs biologiques demeure un sujet de recherche très actif [12]. La méthode de diagnostic la plus répandue est l'échographie

transrectale (TRUS) permettant de visualiser les régions d'intérêts afin de guider une série de biopsies transpérinéales. Lorsque le médecin suspecte toujours un cancer malgré un résultat négatif de cette technique, il peut avoir recours à sa version améliorée qui fusionne des images IRM préopératoires avec l'échographie transrectale pour mieux guider la procédure de biopsie. D'autres systèmes d'imagerie peuvent être utilisés. La Tomographie par Émission de Positrons (PET) est souvent employée pour détecter les cas de rémission après traitement et la Tomographie Computationnelle (CT) permet de monitorer la progression du cancer dans le corps à l'aide des rayons X [8], [9], [13].

Il existe plusieurs traitements possibles selon la nature et le grade du cancer diagnostiqué ainsi que les préférences et l'état de santé global du patient. Du fait de la progression lente de nombreux cancers de la prostate, ne causant ni symptômes ou problèmes, la surveillance active peut être utilisée. Pour les cas plus agressifs, la principale méthode de chirurgie demeure la prostatectomie radicale afin de retirer les tissus cancéreux. La radiothérapie est aussi très souvent utilisée pour administrer des rayons de haute énergie détruisant les cellules cancéreuses. Ce traitement peut être accompli de manière externe ou interne en insérant chirurgicalement un radioisotope au voisinage de la tumeur à l'aide de canules de guidage aux dimensions semblables à celles d'une aiguille de biopsie. La radiothérapie interne, aussi appelée curiethérapie, permet d'administrer des doses plus fortes que la radiothérapie externe. L'immunothérapie et l'hormonothérapie se démarquent par les progrès significatifs accomplis ces dernières années. Alors que la première cherche à renforcer le système immunitaire des patients pour lutter contre le cancer, la seconde se base sur l'utilisation de médicaments pour bloquer la production ou les effets d'hormones comme la testostérone. En conjonction avec d'autres traitements, cette méthode permet de réduire ou de ralentir la croissance des cellules cancéreuses. Enfin la chimiothérapie est également un traitement adjuvant utilisé lorsque le cancer se propage au-delà des limites de la prostate, notamment en cas de métastases [8], [9], [13].

1.3 La procédure de biopsie de la prostate et ses limites

L'importance d'un diagnostic précis du cancer fait de la procédure de biopsie de la prostate une étape critique dans la prise en charge du patient. Cette chirurgie minimalement invasive consiste à

récolter un ou plusieurs échantillons représentatifs de la tumeur à l'aide d'une aiguille de biopsie. Ces échantillons permettent d'obtenir l'information histopathologique servant de base aux choix des traitements utilisés. Comme mentionné précédemment, l'approche conventionnelle pour obtenir les échantillons représentatifs consiste en l'insertion d'une aiguille de biopsie par voie transpéritinale avec un guidage TRUS. La figure 1.1 illustre le mécanisme de l'aiguille composée d'une canule externe creuse ainsi que d'une canule interne disposant d'une chambre de prélèvement à son extrémité. Dans un premier temps, l'aiguille est positionnée au contact de la zone d'intérêt (figure 1.C) avec les deux canules rétractées, isolant ainsi la chambre de prélèvement du tissu environnant. Puis la canule interne est déployée dans le tissu en glissant à l'intérieur de la canule externe le long de l'axe de l'aiguille. La pression du tissu environnant est alors suffisante pour remplir la chambre de prélèvement, désormais en contact avec son environnement biologique (figure 1.D). Quasi-immédiatement après, la canule externe glisse selon le même axe pour recouvrir la canule interne et l'isoler à nouveau (figure 1.E) en découpant ainsi l'échantillon contenu dans la chambre. Le passage des étapes entre figure 1.C et figure 1.E se fait en un instant grâce au système de ressorts contenus dans le manche de l'aiguille de biopsie. En plus d'être guidé par un système d'imagerie, le chirurgien peut aussi utiliser un canevas de guidage (figure 1.B) afin d'améliorer le contrôle et la répétabilité de la trajectoire des instruments vers la région d'intérêt.

La précision et l'exactitude du guidage dépend nécessairement des avantages et inconvénients des systèmes d'imagerie utilisés. Ainsi que vu précédemment, la curiethérapie repose sur l'insertion de canules de guidages à l'aide des mêmes systèmes. Il est donc pertinent d'évaluer indifféremment la précision de ces deux procédures, biopsie et curiethérapie. Leur principale limitation réside dans la limite de précision pour déterminer la localisation exacte de la tumeur relative aux instruments [14], [15]. Or l'identification des aiguilles et/ou canules sur des images ultrason (US) est délicate et dépend beaucoup de l'expérience du chirurgien [16]. En conséquence il existe un risque majeur de prélever un échantillon non représentatif de la tumeur suite à une définition erronée du guidage vers la cible. Dans le cas de la procédure de biopsie, l'approche standard TRUS conduit ainsi à des taux de faux négatifs pouvant atteindre les 30% [17], [18]. En plus d'endommager la qualité du diagnostic, cela conduit à une ou plusieurs répétitions de la procédure de biopsie elle-même, multipliant ainsi les risques chirurgicaux associés. Dans le cas de la curiethérapie le manque de précision dans le guidage des instruments se transforme en un manque de précision dans la localisation de l'administration du rayonnement de haute énergie. Non

seulement la tumeur ne reçoit pas la dose prévue de radiation, mais les tissus sains environnants se retrouvent surexposés.

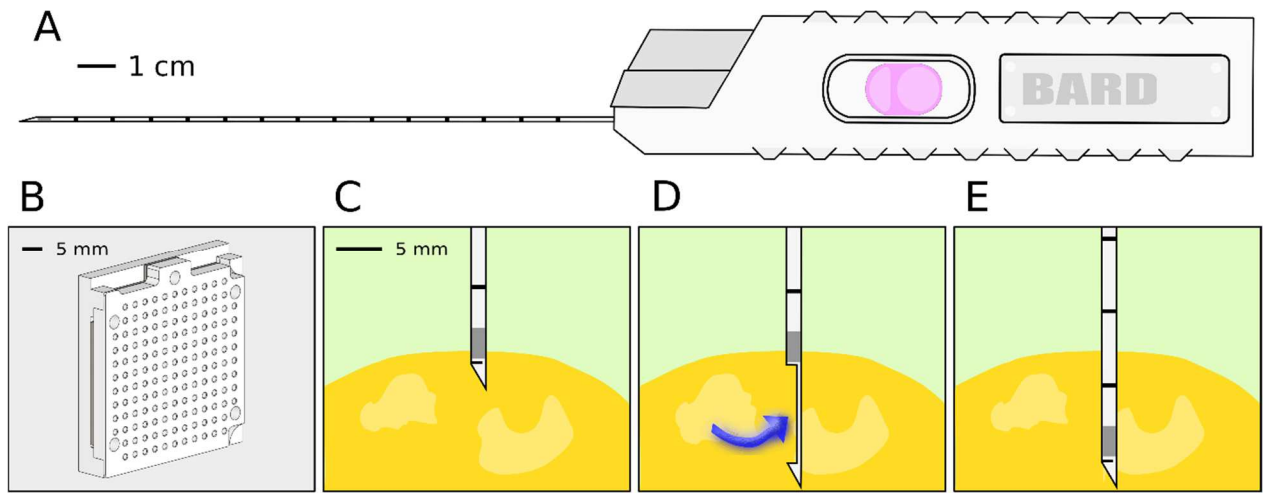


Figure 1.1 Schéma de (A) l'aiguille de biopsie de la prostate (Bard Medical, USA), (B) du canevas de guidage, et des étapes de la prise d'échantillon : (C) aiguille située sur la cible avec canules internes et externes rétractées, (D) canule interne relâchée et ouverture de la chambre de prélèvement, (E) canule externe relâchée et fermeture de la chambre de prélèvement.

Le guidage électromagnétique (EM) s'est révélé être une réponse prometteuse pour palier à ce problème. Il s'agit d'introduire un équipement parcouru d'un courant électrique dans un champ électromagnétique contrôlé et généré par un caisson externe. L'interaction entre le courant et le champ crée une perturbation mesurable par l'équipement qui permet de le repérer spatialement. Ainsi des études utilisant ce type d'équipement lors de procédures de curiethérapie ont mis en évidence son potentiel pour améliorer le guidage des instruments chirurgicaux [19]–[21]. Une autre méthode très utilisée repose sur l'IRM et sa capacité à exploiter le spin de certains noyaux atomiques afin de distinguer les tissus. L'IRM seule est associée à une sensibilité et une spécificité supérieure à la biopsie guidée par TRUS [22], [23], avec notamment une sensibilité de 85% pour les tumeurs de largeur >10mm [24]. Le manque d'accessibilité intraopératoire de l'IRM a donc poussé à son usage préopératoire et sa fusion avec le guidage TRUS [25], [26] avec pour but de cumuler la sensibilité de l'IRM et la spécificité du TRUS. À cause des déformations dynamiques

des tissus provoquées par les instruments chirurgicaux, le recalage entre les images des différents systèmes demeure problématique et un domaine de recherche très actif [27]–[29].

1.4 Solution proposée

Afin de répondre à ce problème clinique associé aux biopsies de la prostate et aux procédures de curiethérapie, la solution proposée repose sur la combinaison de plusieurs modalités d'imagerie optique afin de mieux localiser les tumeurs de la prostate. La spectroscopie Raman, la spectroscopie de fluorescence et la tomographie optique diffuse peuvent être intégrées en milieu clinique et utilisées en synergie afin de recouvrir la signature moléculaire des tissus biologiques et donc de les différencier [30]–[32]. Ces trois techniques sont basées sur différentes interactions entre la lumière et la matière, notamment l'absorption, la diffusion élastique/inélastique et la fluorescence. Dans chaque cas, il s'agit d'une approche visant à obtenir le contraste moléculaire et non plus morphologique comme le fait la procédure de guidage standard TRUS-IRM. Le principal défi de cette intégration repose sur la préservation des performances du standard de guidage. À cet effet, le système optique proposé devra donc aussi intégrer un capteur EM servant à optimiser la plateforme de navigation basée sur le TRUS-IRM en améliorant la précision du recalage d'images entre le TRUS et l'IRM. Le détail théorique de ces modalités d'imagerie optiques est présenté avec l'état de l'art dans le chapitre suivant.

1.5 Hypothèses et objectifs du projet

La question centrale du projet de recherche faisant l'objet de cette thèse porte sur l'amélioration de l'efficacité du guidage des procédures de biopsie de la prostate grâce à l'intégration de mesures de spectroscopie optique, réflectance diffuse, autofluorescence et spectroscopie Raman en particulier. Mon projet se base ainsi sur les 2 hypothèses scientifiques suivantes :

1. La spectroscopie Raman permet de discriminer entre les tissus sains et les tissus cancéreux, avec une précision de diagnostic suffisante permettant de répondre au problème clinique du guidage de la procédure de biopsie de la prostate.

2. Un système optique multimodal intégrant la spectroscopie Raman combiné avec une plateforme de navigation incluant l'imagerie TRUS-IRM et le guidage Électromagnétique peut permettre le guidage de l'aiguille de biopsie vers la zone représentative de la tumeur de la prostate, tout en minimisant les perturbations causées à la chirurgie.

Pour tester ces 2 hypothèses, les objectifs du projet de recherche sont énoncés comme suit :

Objectif 1 : Établir une preuve de concept sur la faisabilité de l'intégration d'une sonde optique à la procédure de biopsie de la prostate.

Sous-objectif 1.1 : Acquérir des données optiques interstitielles, à l'aide d'une sonde basées sur la spectroscopie de réflectance diffuse, au cours d'une expérience sur un modèle animal porcin.

Sous-objectif 1.2 : Évaluer les choix de designs du prototype de sonde utilisé afin d'optimiser la conception d'un nouveau prototype compatible avec l'acquisition de spectres Raman au cours de procédures de biopsie de la prostate sur des êtres humains.

Objectif 2 : Concevoir et manufacturer un système optique multimodal optimisé pour le guidage chirurgical permettant de classifier entre tissus cancéreux et tissus sains.

Ce nouveau prototype de sonde doit être compatible avec les contraintes cliniques associées à la procédure de biopsie de la prostate, et doit permettre de combiner la spectroscopie Raman (régions spectrales *fingerprint* et *high wavenumber*), la spectroscopie d'autofluorescence, la spectroscopie de réflectance diffuse, et le guidage Électromagnétique.

Objectif 3 : Effectuer une étude clinique (patients humains) impliquant le prototype conçu et fabriqué dans le cadre de l'Objectif 2 afin d'établir ses performances de diagnostic.

Sous-Objectif 3.1 : Effectuer une étude clinique sur des échantillons *ex vivo* mettant en évidence la capacité du système Raman à diagnostiquer les tissus sains des tissus cancéreux.

Sous-Objectif 3.2 : Effectuer une étude clinique *in vivo* au cours de procédures de biopsie de la prostate, mettant en évidence la capacité du système Raman à diagnostiquer les tissus sains des tissus cancéreux.

L'ensemble de cette étude porte sur la conception, la fabrication et l'évaluation d'une sonde optique multimodale assistant le guidage de la procédure de biopsie de la prostate. Cette thèse présente le travail de développement de ce système optique et le test des hypothèses scientifiques via les objectifs de recherche formulés ci-dessus. La présente introduction est suivie par un chapitre de revue de littérature détaillant les différentes techniques optiques considérés pour l'étude ainsi que leur application au diagnostic de cellules cancéreuses dans le cadre d'interventions chirurgicales. Le chapitre 3 présente en détail la méthodologie et la démarche scientifique de l'ensemble du travail de recherche. Les chapitres 4, 5 et 6 portent sur les trois articles scientifiques publiés dans le cadre de ma thèse de doctorat. Finalement, les chapitres 7 et 8 contiennent respectivement la discussion générale du projet ainsi que les conclusions et recommandations pour les perspectives futures.

CHAPITRE 2 REVUE DE LITTÉRATURE

Les molécules qui composent les tissus biologiques sont caractérisées par les niveaux énergétiques (électroniques, vibrationnels et rotationnels) sur lesquels leur nuage électronique est distribué. Lors d'une interaction lumière/matière, la distribution énergétique des électrons peut se trouver modifiée selon la nature de la lumière i.e. sa longueur d'onde, son état de polarisation etc. La mesure de ces modifications par des techniques spectroscopiques permet de retrouver les niveaux énergétiques des molécules ayant interagis avec la lumière et donc de les caractériser. On distingue ainsi deux types d'interactions lumière/matière, celle dites résonantes (absorption, fluorescence, phosphorescence) et celles dites non résonnantes (diffusion élastique et diffusion inélastique). Dans ce chapitre nous ferons une revue détaillée de ces différentes interactions ainsi que les techniques les exploitant pour caractériser les tissus dans un cadre d'applications oncologiques.

2.1 Spectroscopie par Réflectance Diffuse

Comme mentionné précédemment, une molécule est caractérisée par ses niveaux énergétiques. Lorsque la différence d'énergie entre son état fondamental et un état excité correspond exactement à l'énergie d'un photon incident, l'interaction résonante d'absorption peut se produire. Le photon est ainsi absorbé et son énergie est emmagasinée par le nuage électronique de la molécule impliquée dans le processus. Une autre interaction majeure, cette fois-ci dite non résonante, est la diffusion. Il s'agit d'un processus au cours duquel des photons incidents changent de direction de propagation en interagissent avec la matière. Lorsque ce phénomène survient, la molécule impliquée voit sa distribution d'énergie transiter par un état virtuel avant la réémission rapide des photons diffusés. Dans le cas d'une diffusion élastique (Rayleigh, Mie), l'interaction lumière/tissu généralement dominante, l'énergie des photons diffusés est conservée. Le diagramme de Jablonski sur la figure 2.1 illustre ces transitions énergétiques lors d'événements d'absorption et de diffusion entre un photon incident et une molécule.

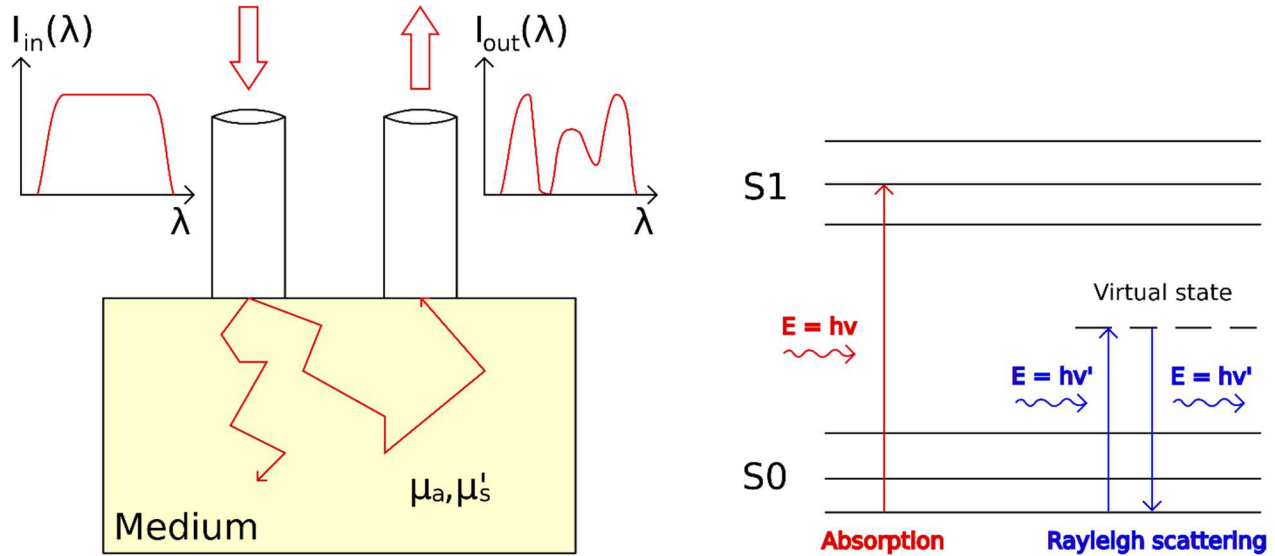


Figure 2.1 Géométrie de détection semi-infinie de la spectroscopie par réflectance diffuse et diagrammes de Jablonski pour les interactions lumière/matière d'absorption et de diffusion élastique.

La spectroscopie par réflectance diffuse (SRD) exploite ces deux interactions, absorption et diffusion élastique, afin de recouvrir en guise de contraste spatial les coefficients d'absorption μ_a et de diffusion μ_s du milieu sondé et généralement exprimés en cm^{-1} . En pratique on utilise le coefficient de diffusion réduit μ'_s défini par $\mu'_s = \mu_s(1 - g)$ où g est le coefficient d'anisotropie du milieu. Dans la mesure où ces propriétés sont reliées au contenu biologique, elles permettent de détecter certaines pathologies. Comme illustré sur la figure 2.1, la géométrie de détection standard consiste en la juxtaposition d'une voie d'illumination et de détection dans le cas d'une modélisation de milieu semi-infini. De la lumière, au spectre large et connu, se propage dans le milieu déclenchant une multitude d'événements d'absorption et de diffusion. La superposition de toutes ces interactions conduit à la rétrodiffusion de certains photons dans la voie de détection menant ainsi à la mesure du spectre de réflectance diffuse. En combinant le spectre d'illumination et le spectre mesurée il est ainsi en théorie possible de retrouver les coefficients d'absorption et de diffusion qui servent de marqueurs biomoléculaires.

Afin de déterminer la propagation des photons dans le milieu, plusieurs outils ont été adaptés au domaine biomédical. L'équation de Boltzmann ci-dessous permet ainsi de décrire cette propagation de la lumière en tenant compte de l'anisotropie [33].

$$\left(\frac{1}{c} \frac{\partial}{\partial t} + \hat{s} \cdot \nabla + \mu_{tr}(r) \right) \Phi(r, \hat{s}, t) = \mu_s(r) \int_{S^{n-1}} \theta(\hat{s} \cdot \hat{s}') \Phi(r, \hat{s}', t) d\hat{s}' + q(r, \hat{s}, t)$$

Où r et \hat{s} sont respectivement les vecteurs position et unité dans l'espace S^{n-1} . μ_s et μ_{tr} sont respectivement les coefficient de diffusion et d'extinction, ce dernier définie par la somme de μ_s et de μ_a le coefficient d'absorption. $\theta(\hat{s} \cdot \hat{s}')$ représente la probabilité de diffusion depuis la direction \hat{s} vers la direction \hat{s}' , $\Phi(r, \hat{s}, t)$ est le nombre de photons par unite de volume à la position r se propageant dans la direction \hat{s} , et c est la celerite de la lumiere dans le vide. Finalement $q(r, \hat{s}, t)$ est le nombre de photons de source par unité de temps à la position r se propageant dans la direction \hat{s} .

Pour les tissus très diffusant et peu absorbants, l'équation de la diffusion, qui dérive de l'équation de Boltzmann, offre des solutions analytiques sous la forme d'harmoniques sphériques [34]. Toutefois ces solutions ne sont pas adaptées aux domaines de propagation discontinus ainsi qu'aux domaines comportant des régions non diffusantes [35], [36]. De plus cette approximation n'est pas valide près de la source [37], [38], ce qui est une limite majeure dans le cas des mesures interstitielles dont l'utilisation est anticipée dans le cadre du projet.

Il existe plusieurs méthodes numériques pour pallier aux faiblesses des méthodes analytiques et approximer la solution de l'équation de Boltzmann. L'une des plus courantes est d'estimer la propagation des photons à l'aide de simulations de type Monte-Carlo [39]–[41]. Ces dernières reproduisent fidèlement les caractéristiques du milieu à quelques hypothèses simplificatrices près, comme la non-interaction des photons entre eux ou les effets non-linéaires qui sont négligés [34]. L'erreur associée à ces estimations diminue avec l'augmentation du nombre de photons simulés, elles sont ainsi coûteuses en temps de calcul (possiblement plusieurs heures) mais présentent l'avantage de pouvoir simuler le transport de la lumière dans des domaines complexes et hétérogènes, notamment grâce à l'utilisation de maillages tétraédriques [42]–[44].

Mathématique, le recouvrement des propriétés optiques passe par la résolution du problème inverse posé comme suit [33]:

On appelle Ω le domaine de propagation considéré, avec une surface $\partial\Omega$ le délimitant. Le problème direct est défini par :

Soit $\{q\}$ une liste de sources disposées sur $\partial\Omega$, avec μ_a et μ'_s connus à l'intérieur de Ω , trouver $\{y\}$, la mesure des photons collectés sur $\partial\Omega$.

Et le problème inverse est défini par :

Soit $\{q\}$ une liste de sources disposées sur $\partial\Omega$, avec $\{y\}$, la mesure des photons collectés sur $\partial\Omega$, trouver μ_a et μ'_s à l'intérieur de Ω .

Ainsi la résolution du problème inverse correspond à la résolution de l'équation suivante :

$$\{y\} = f(q(\partial\Omega), \mu_a(\Omega), \mu'_s(\Omega))$$

Où $\mu_a(\Omega)$ et $\mu'_s(\Omega)$ sont les inconnues recherchées et f est définie par le problème direct grâce aux méthodes, analytiques ou numériques, citées précédemment. Très souvent, il s'agit d'un problème non-linéaire et surtout mal posé puisque associé à une non-unicité des solutions. Parmi les méthodes de résolution proposées, on trouve des algorithmes de rétroprojection qui consistent à projeter un contraste optique mesuré sur un parcours optique estimé [45].

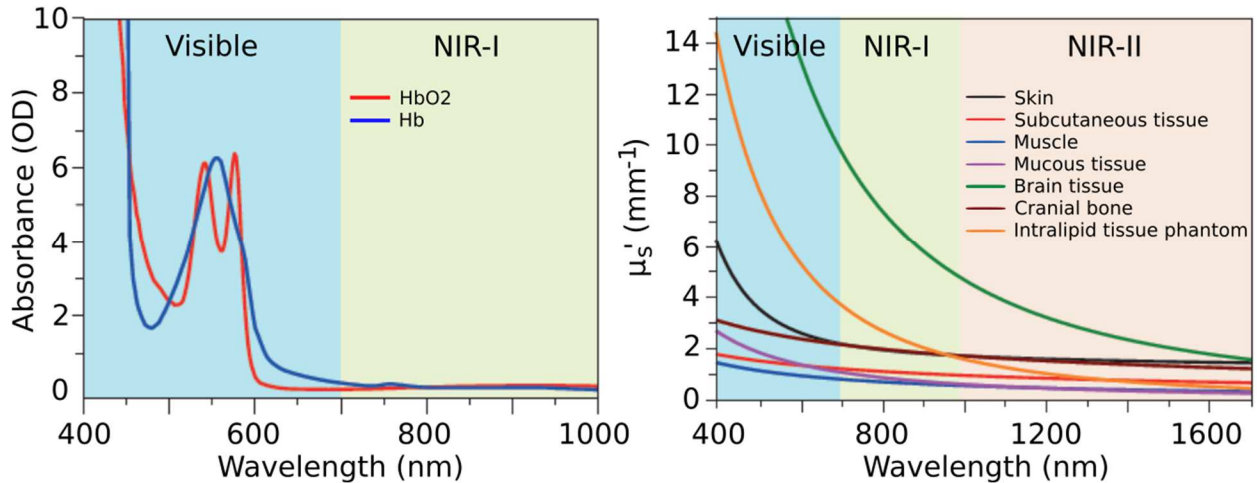


Figure 2.2 Spectre des Principaux absorbeurs (Hémoglobine) et spectres de diffusion de plusieurs tissus [46].

Afin d'augmenter la spécificité de la reconstruction des propriétés optiques, il est possible de corrélérer la signature spectrale obtenue à des éléments biologiques connus. Les coefficients $\mu_a(\Omega)$ et $\mu'_s(\Omega)$ sont ainsi calculés sur toute une plage spectrale, dans le visible et/ou le proche IR.

Ensuite un modèle biophysique du milieu sondé est estimé à partir de ces résultats et des principaux éléments absorbants et diffusants du corps humain illustrés sur la figure 2.2. Enfin, mis à part les algorithmes de rétroprojection, les algorithmes d'optimisation sont également à présenter. À partir d'une première estimation, la solution proposée du problème inverse se rapproche itérativement de l'optimum en réduisant à chaque pas l'erreur calculée. La méthode du gradient en est un exemple, tout comme la méthode de Newton présentée en détails dans [47], [48].

La SRD présente plusieurs applications chirurgicales dont l'imagerie fonctionnelle du cerveau [49], [50] ainsi que la détection du cancer du sein [51], [52], du col de l'utérus [53] et de la peau [54]. Cependant elle trouve un plus fort impact dans les applications de diagnostic lorsque utilisée en synergie avec la spectroscopie par fluorescence. Ce type de spectroscopie, présentée en détails dans la section suivante, est en effet plus sensible et spécifique pour l'identification des tissus biologiques.

2.2 Spectroscopie de Fluorescence/Autofluorescence

La fluorescence est une interaction lumière-matière permettant de sonder les tissus biologiques. Lorsqu'un photon suffisamment énergétique est absorbé par une molécule, le processus d'absorption peut être suivi d'une transition non radiative comme illustrée sur le diagramme de la figure 2.3. La molécule se désexcite ensuite par la réémission d'un photon moins énergétique que le photon incident, i.e. le photon réémis est d'une longueur d'onde plus élevée. On appelle les molécules qui présentent ce type d'interaction des fluorophores. Le spectre d'émission total d'un tissu est ainsi la somme pondérée des spectres des fluorophores qui le composent. Grâce à la connaissance a priori du spectre d'émission de ces molécules que l'on cherche dans un tissu, il est possible de retrouver leurs concentrations respectives et ainsi classer le tissu selon son contenu moléculaire. Les fluorophores peuvent être induit dans le milieu grâce à une autre drogue externe qui n'est elle-même pas un fluorophore. L'acide aminolevulinique (ALA) permet par exemple l'accumulation de protoporphyrin IX (PpIX), qui est un fluorophore, dans les tissus pathologiques ce qui permet le guidage d'opérations de résection dans le cerveau [55], [56]. Lorsqu'aucun élément externe n'est introduit et que le signal capté est uniquement dû à la fluorescence intrinsèque, on parle alors d'autofluorescence des tissus.

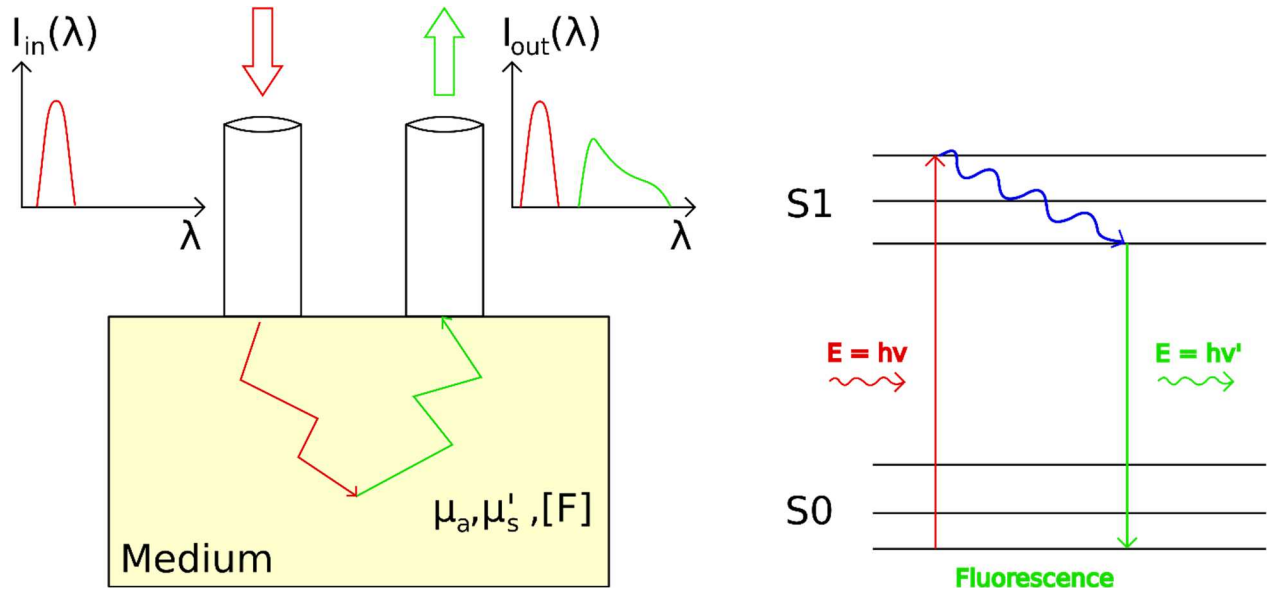


Figure 2.3 Géométrie de détection semi-infinie de la spectroscopie de fluorescence et diagrammes de Jablonski pour l’interaction lumière/matière de fluorescence.

La spectroscopie par autofluorescence permet la détection des fluorophores endogènes, ce qui inclut des enzymes, acides aminés et protéines [57]. Cette technique présente l’avantage de ne pas nécessiter l’injection d’une drogue externe tout en étant plus spécifique en contraste moléculaire que la SDR. De plus les reconstructions des coefficients d’absorption et de diffusion issues de la SDR peuvent être utilisées pour extraire une mesure quantitative de la fluorescence. À partir des mesures brutes, la concentration des fluorophores du milieu est obtenue en corrigeant pour les distorsions causées par les propriétés optiques du milieu selon l’équation suivante [58].

$$F_C(\lambda) = \frac{F_{meas}(\lambda)}{R_x(R_m)^{-0.7}}$$

Où $F_C(\lambda)$ est le signal de fluorescence corrigée, $F_{meas}(\lambda)$ le signal brut, R_x et R_m les valeurs de reflectance diffuse aux longueurs d’onde d’excitation et d’émission respectivement. Le coefficient de puissance -0.7 est ajouté pour tenir compte de l’atténuation du coefficient de diffusion aux longueurs d’onde d’émission. Les valeurs R_x et R_m sont directement issues de mesures faites avec la SDR ce qui conduit à construire des systèmes d’imagerie optiques combinant deux sous systèmes, un dédié à la fluorescence et l’autre aux mesures de réflectance diffuse. Le succès de la

spectroscopie de fluorescence est ainsi d'autant plus grand qu'il intègre des méthodes de correction d'atténuation basées sur le recouvrement des propriétés optiques d'absorption et de diffusion [59], [60].

Plusieurs exemples d'applications oncologiques sont disponibles dans la littérature. La spectroscopie d'autofluorescence a notamment été utilisée pour la détection du cancer du sein [61], du poumon [62] et du larynx [63]. Cependant cette technique demeure limitée en précision [64], [65] et apparaît plus comme un complément utile à une méthode plus sensible et spécifique telle que la spectroscopie Raman [57].

2.3 Spectroscopie Raman

2.3.1 Diffusion Raman dans les tissus biologiques

La spectroscopie Raman (SR) repose sur la diffusion Raman, une interaction inélastique entre la lumière et la matière. Contrairement à une diffusion élastique, cette interaction entre les photons incidents et la molécule déforme le nuage électronique de ladite molécule. La direction de cette distorsion dépend de la polarisation de la lumière et son amplitude est proportionnelle à la polarisabilité de la molécule, i.e. la capacité d'une distribution de charge à se polariser. Ainsi, seuls les axes de vibration des composantes nucléaires qui induisent une variation de polarisabilité peuvent participer à un événement de diffusion Raman. Cette règle de sélection de base permet d'identifier les modes de vibrations, et leurs transition énergétique associées, qui sont actifs en Raman. Au niveau quantique, lorsqu'un photon de fréquence v_0 interagit avec une molécule biologique, il existe une probabilité de l'ordre de 10^{-7} qu'il soit diffusé à une fréquence v_1 différente de v_0 , i.e. qu'un transfert d'énergie se produise entre le photon et la molécule. Si $v_1 < v_0$ alors une partie de l'énergie du photon est transférée à la molécule sous forme d'énergie vibrationnelle, on parle alors de diffusion Raman Stokes. Un phénomène de diffusion moins courant encore est la diffusion Raman Anti-Stokes caractérisé par le fait que $v_0 < v_1$, i.e. une partie de l'énergie de la molécule est transmise au photon. Vu que ce type de transition ne peut se produire que si la molécule impliquée est déjà dans un état vibrationnel excité, sa probabilité d'occurrence est liée à la distribution de Maxwell-Boltzmann décrite ci-dessous [66]:

$$\frac{N_1}{N_0} = \frac{g_1}{g_0} e^{\frac{-h(v_1-v_0)}{kT}}$$

Avec N_1 et N_0 le nombre de molécules dans le niveau d'énergie vibrationnel excité et fondamental respectivement. g_1 et g_0 représentent les dégénérescences des niveaux 1 et 0. $h(v_1 - v_0)$ est la différence d'énergie entre les niveaux, T la température de l'échantillon, h et k sont les constantes de Planck et Boltzmann respectivement. À température ambiante, la probabilité d'une diffusion Raman Stokes est donc plus grande de plusieurs ordres de grandeur qu'une diffusion Anti-Stokes. La figure 2.4 illustre sur un diagramme de Jablonski ces deux types de transition énergétiques ainsi que la géométrie de détection d'un système Raman standard.

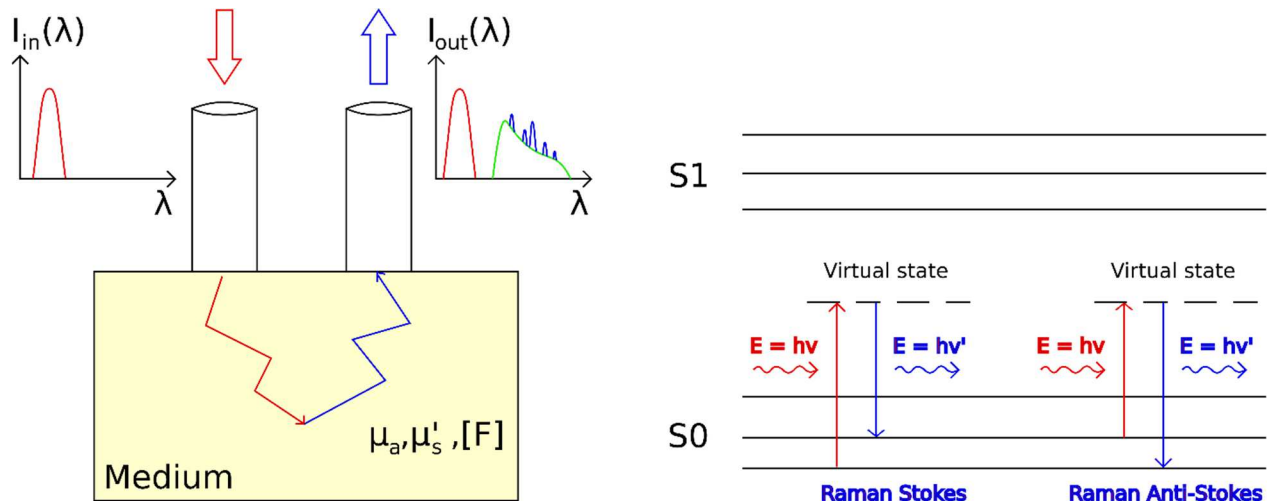


Figure 2.4 Géométrie de détection semi-infinie de la spectroscopie de Raman et diagrammes de Jablonski pour l'interaction Raman Stokes et Raman anti-Stokes.

En pratique pour construire un système Raman Stokes spontané, on combine une source laser monochromatique, de longueur d'onde λ_0 , pour illuminer un échantillon et on mesure la lumière diffusée avec un spectromètre. L'intensité lumineuse mesurée dans l'intervalle de longueur d'onde $[\lambda_0; \lambda_1]$ contient la superposition du spectre d'émission d'autofluorescence ainsi que le spectre Raman de l'échantillon. La signature Raman d'une molécule se compose de la somme des contributions de tous ses modes vibrationnels actifs en Raman. La signature Raman d'un échantillon est ainsi caractérisée de façon unique par la somme pondérée des signatures de chacune

des molécules qui le composent. Cette technique utilise d'avantages d'éléments en guise de contraste que la spectroscopie de fluorescence, limité aux fluorophores. Les molécules actives en Raman incluent en effet des acides-aminés, des protéines, des lipides et des acides nucléiques. Typiquement le spectre mesuré n'est jamais représenté sur une échelle de longueurs d'onde mais plutôt selon le nombre d'onde, i.e. le décalage entre le photon émis et le photon incident. Ce nombre d'onde exprimé par la formule ci-dessous permet de comparer les spectres obtenus indépendamment de la longueur d'onde d'excitation utilisée.

$$K \text{ (cm}^{-1}\text{)} = \frac{1}{\lambda_0} - \frac{1}{\lambda_1}$$

L'utilisation du nombre d'onde comme échelle met en évidence deux plages spectrales distinctes pour lesquelles les échantillons biologiques présentent un signal d'intérêt. Tout d'abord la plage spectrale entre 400 et 1800 cm⁻¹ qui est couramment appelée “fingerprint” étant la plus riche en information sur le contenu biomoléculaire. Puis la plage entre 2400 et 3800 cm⁻¹ appelée en conséquence “high wavenumber” [67]–[69]. Entre les deux la signature Raman est typiquement nulle comme illustré sur la figure 2.5.

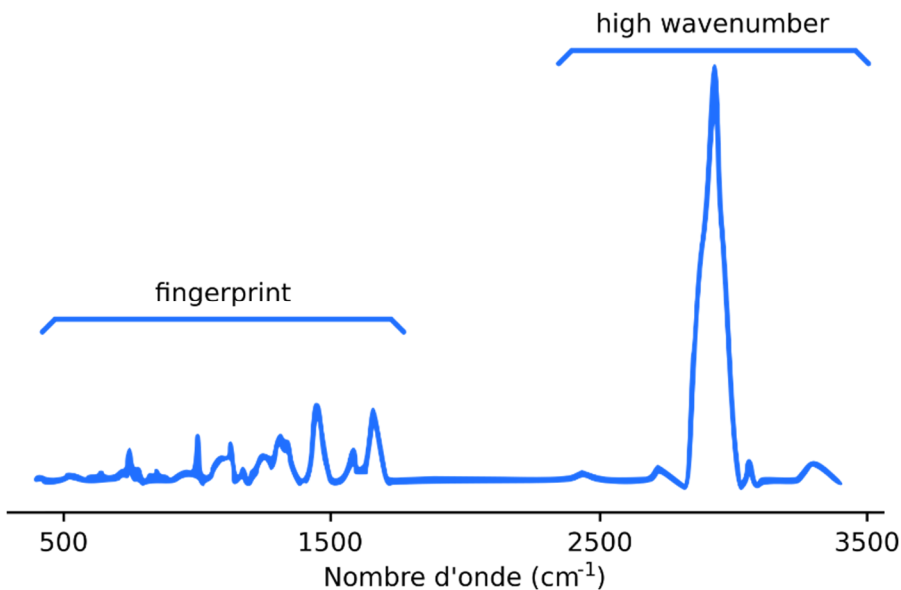


Figure 2.5 Illustration des régions spectrales *fingerprint* et *high wavenumber* d'un spectre Raman d'un échantillon biologique.

Le choix de la longueur d'onde lambda de la lumière incidente est un compromis entre plusieurs facteurs afin d'optimiser la qualité du signal Raman collecté. Tout d'abord les tissus biologiques sondés imposent de choisir une longueur d'onde dans la fenêtre thérapeutique comprise environ entre 600 et 1200 nm afin de maximiser le signal. Cette plage spectrale présente en effet une faible absorption pour les chromophores couramment rencontrés dans les tissus tel que l'hémoglobine, la mélanine et l'eau [31], [66]. De plus la section efficace de la diffusion Raman est inversement proportionnelle à λ^4 [70], d'où un intérêt à choisir lambda plus proche de l'UV. Cet avantage doit cependant être exploité avec précaution car l'autofluorescence des tissus a également tendance à augmenter avec la diminution de la longueur d'onde [71], [72]. Le signal brut étant la somme des signaux Raman et d'autofluorescence, le choix de λ est donc un équilibre pour maximiser le ratio du premier sur le second. En conséquence, les longueurs d'onde d'excitation usuellement utilisées dans la spectroscopie Raman sont 633, 785, 830 et 1064 nm [73].

2.3.2 Applications de la spectroscopie Raman en oncologie

Comme vu dans la section précédente, la signature Raman d'un échantillon est constituée de la somme pondéré des signatures Raman des molécules qui le composent. Toutefois au vu de la multitude des composantes d'un échantillon biologique, il devient hasardeux de retrouver les proportions respectives des molécules présentes, même en connaissant au préalable leur spectre Raman. En revanche, grâce à des méthodes de classification, il est possible d'exploiter les différences plus globales pour distinguer un tissu sain d'un tissu malade au sein d'un même organe [74]. La spectroscopie Raman est ainsi une technologie émergente et prometteuse dans le domaine médical pour la caractérisation des tissus [30], [31]. Une difficulté majeure de cette technique d'imagerie est la faible proportion de ce type de diffusion inélastique. Le signal utile est en effet en compétition avec d'autres phénomènes (diffusion Rayleigh, autofluorescence des tissus) qu'il convient de mitiger par des équipements optiques adaptés et par des traitements numériques. Cependant les dernières décennies ont vu des progrès significatifs dans les éléments nécessaires dans la conception d'un système Raman. Des diodes lasers stables ainsi que des spectromètres à haute résolution incluant des détecteurs plus sensibles peuvent notamment être cités en exemple (CCD et EMCCD). Ce n'est que depuis une vingtaine d'années que ces progrès technologiques ont permis l'utilisation de la spectroscopie Raman dans le domaine biomédical.

Plusieurs techniques existent pour augmenter significativement le signal Raman par rapport à la technique classique qui repose sur la diffusion inélastique spontanée. L'utilisation de nanoparticules en contacts avec l'échantillon sondé est une méthode répandue pour augmenter la section Raman efficace de plusieurs ordres de grandeur. Cette méthode, appelée SERS (Spectroscopie Raman de Surface Améliorée), présente toutefois l'inconvénient d'utiliser un agent exogène [75]–[82]. Deux techniques se distinguent par leur capacité à augmenter le signal Raman sans présenter un tel désavantage. La spectroscopie Raman Cohérente Anti-Stokes (CARS) [83]–[88] et la spectroscopie Raman Stimulée (SRS) [89]–[94] permettent d'amplifier la mesure de spectres Anti-Stokes et Stokes respectivement, au prix de l'utilisation de sources lasers supplémentaires.

Au-delà de l'amélioration de la quantité et qualité du signal, d'autres techniques sont également à citer dans les progrès de cette technologie. La microscopie confocale s'est montrée parfaitement compatible à une utilisation couplée avec la spectroscopie Raman [31], [95]–[97], permettant d'obtenir des images 3D avec une résolution spatiale de l'ordre du micromètre. De plus l'usage de fibres optiques a permis de répandre très largement son usage dans des applications chirurgicales, y compris oncologiques pour détecter les cellules cancéreuses [31], [57], [98]–[100]. Le système repose alors sur l'utilisation d'un endoscope ou d'une sonde dans lesquels sont contenus les fibres optiques servant à illuminer le milieu et à collecter la lumière diffusée. Cependant le silicium dont sont faites les fibres possède une très forte réponse Raman et d'autofluorescence dans la région *fingerprint* du spectre. Il est donc indispensable, pour capturer la réponse de l'échantillon sans artefacts, de combiner des filtres optiques à l'extrémité distale des fibres afin de supprimer la signature de la silice causée par la source laser du système. Cet artefact n'étant présent que dans la région *fingerprint*, il est possible de construire un système Raman HWN sans filtres, uniquement avec la source laser, un spectromètre et une sonde fibrée [100]. L'utilisation des fibres permet en outre de concevoir des systèmes résolus en profondeur grâce à un éloignement contrôlé (ou *Spatial Offset*) entre la fibre d'illumination et la fibre de détection. Ce type de spectroscopie Raman, appelé SORS, utilise la distance de parcours des photons dans le milieu de propagation, variant en fonction de cet éloignement contrôlé, pour collecter les photons Raman provenant de diverses profondeurs. L'association entre l'information optique et l'information de profondeur permet d'obtenir une résolution de l'ordre de 1 mm sur quelques

millimètres de profondeur et se révèle particulièrement critique dans la caractérisation des marges dans des chirurgies de résection tumorales [101], [102].

La dernière décennie a vu une explosion des études portant sur les applications de la spectroscopie Raman en oncologie. L'importation d'un système optique en environnement clinique passe généralement en premier lieu par des expériences *ex vivo*. Ainsi, plusieurs études ont montré la capacité de la spectroscopie Raman à discriminer entre les tissus sains et tumoraux pour les cancers du sein [103], [104], de la prostate [68], [105], du col de l'utérus [106] et du colon [107], [108]. Les applications sur des tests *in vivo* se sont multipliées à toute une série d'organes toujours dans le but d'améliorer la détection du cancer pour le guidage de chirurgie. On dénombre ainsi des études sur le cancer du cerveau [57], [98], [109], du col de l'utérus [110], [111], du colon [69], gastro-intestinal [112]–[114], du poumon [115], [116], de la gorge [67], [117] et de la peau [118]–[121].

Dans le cas du cancer de la prostate, plusieurs études *ex vivo* ont été menées afin de discriminer entre les tissus sains et cancéreux [68], [96], [105]. Une étude avec acquisition de mesures *in vivo* a également été conduite mais n'a pas abouti à un modèle de classification [122]. À ce jour, il n'existe aucune étude clinique portant sur la détection *in situ* du cancer de la prostate à l'aide la spectroscopie Raman.

2.4 Guidage optique multimodal des biopsies de la prostate

Tableau 2.1 Principaux pics Raman dans les tissus de la prostate associés aux modes vibrationnels et molécules correspondantes [68], [96], [105], [122]

Raman shifts (cm^{-1})	Lien associé	Famille de molécules	Molécules
528	S-S	Phospholipides	Phosphatidylserine
622	C-C	Protéines	Phénylalanine
657	N-C	ADN/ARN	Adénine, Guanine
720	C-S, C_6H_5	ADN/ARN, Protéines	Adénine
820	O-P-O, C_6H_5	ADN/ARN, Protéines	Tyrosine
854	C-O-C	Protéines	Tyrosine
940	C-C	Protéines	Proline, Collagène
1004	C-C	Protéines	Phénylalanine
1035	C-H	Protéines	Phénylalanine
1078	C-C, C-O	ADN/ARN, Phospholipides	Amides II
1252	NH ₂	ADN/ARN	Guanine, Cytosine
1307	CH ₂ /CH ₃	Protéines, Lipides	Collagène
1398	CH ₂ /CH ₃	Protéines, Lipides	β -carotène
1444	CH ₂ /CH ₃	Protéines, Lipides	Collagène
1566	CN/NH	Protéines	Tyrosine, Tryptophane
1615	C=C	Protéines	Tyrosine, Tryptophane
1650	C=C	Protéines, Lipides	Amide I
2879	CH ₂ /CH	Lipides	
2930	CH ₂ /CH ₃	Protéines	

Le guidage des procédures de biopsie de la prostate *in situ* à l'aide d'une sonde optique apparaît comme une solution prometteuse. Ce type d'approche fournit à l'utilisateur des informations sur le contenu moléculaire des tissus et permet ainsi non seulement de détecter les régions cancéreuses mais aussi d'éviter l'échantillonnage d'une zone non représentative de la tumeur. Avec les progrès des techniques de miniaturisation il devient aussi possible d'adapter les prototypes aux contraintes de l'environnement clinique tout en combinant différentes modalités de guidage optique.

Le but de ces combinaisons n'est pas une simple juxtaposition des données optiques mais leur utilisation en synergie afin d'extraire l'information intrinsèque des tissus avant de l'utiliser à

des fins de diagnostic. En pratique il s'agit d'utiliser dans un premier temps les spectres de réflectance diffuse afin d'extraire les propriétés optiques d'absorption et de diffusion qui servent à obtenir le signal de fluorescence corrigé du milieu [57], [58]. Puis dans un second temps les modes vibrationnels des molécules sont extraits des spectres Raman fournissant le cœur de l'information biomoléculaire à laquelle s'ajoute celle du signal de fluorescence corrigé. Les principaux pics Raman connus des tissus de la prostate, associés à ces modes vibrationnels, sont listés dans le Tableau 2.1. Ils proviennent majoritairement de la famille des lipides, protéines et acides nucléiques et servent de base à l'interprétation des spectres Raman acquis *in situ* dans la prostate.

Au cours des dernières années, le Laboratoire de Radiologie Optique (LRO), dirigé par le professeur Frédéric Leblond, a publié plusieurs études mettant en évidence la capacité de la spectroscopie Raman à détecter les cellules cancéreuses *in situ*, avec une emphase sur le cancer du cerveau [57], [68], [98], [123]. Ces travaux constituent une base solide pour la détection d'autres types de cancer, y compris le cancer de la prostate, au cours d'interventions chirurgicales. Il s'agit toutefois d'un problème clinique différent avec son lot de contraintes liées aux spécificités de la procédure de biopsie de la prostate. De plus, le tissu prostatique possède un coefficient de diffusion réduit μ_s' de l'ordre de 1 mm^{-1} dans la plage spectrale thérapeutique [124] alors qu'il est plus d'un ordre de grandeur supérieur dans le cerveau [46], [125], [126]. La conséquence attendue est une difficulté plus grande à collecter le signal Raman dans la prostate avec un haut niveau de signal sur bruit, ce qui est confirmé par les études *ex vivo* présentant des performances de diagnostic plus faibles dans la prostate [68], [105] que dans le cerveau [32], [98], [100], [123].

CHAPITRE 3 DÉMARCHE SCIENTIFIQUE ET CONTRIBUTIONS

3.1 Étude préliminaire sur l'utilisation d'une aiguille optique pour la procédure de biopsie

Le premier objectif du projet était d'établir une preuve de concept sur l'intégration d'une sonde optique à la procédure de biopsie de la prostate. Afin de réaliser cet objectif une aiguille optique conçue et fabriquée par Andréanne Goyette dans le cadre de sa Maîtrise [127] a été utilisée au cours d'une expérience reproduisant une biopsie cérébrale sur un porc au Centre de recherche du Centre Hospitalier de l'Université de Montréal (CRCHUM). L'instrument optique (figure 3.1) était un prototype de sonde tomographique basée sur la spectroscopie de réflectance diffuse directement intégrée sur un modèle commercial d'aiguille de biopsie cérébrale.



Figure 3.1 Photographie de l'aiguille optique utilisée lors de l'expérience sur modèle porcin au CRCHUM. L'animal est installé sur une table chirurgicale avec un système de tomographie computationnelle (CT scan) utilisé comme étalon standard pour l'expérience.

Son but premier était de permettre la visualisation des vaisseaux sanguins, en détectant la signature spectrale d'absorption de l'hémoglobine, afin de contrôler les risques d'hémorragie pendant les phases d'insertion de l'aiguille et de collecte de l'échantillon de biopsie.

Mon premier article intitulé “Interstitial imaging with multiple diffusive reflectance spectroscopy projections for *in vivo* blood vessels detection during brain needle biopsy procedures” (*Neurophotonics*, facteur d’impact = 3.593) porte sur la caractérisation de cette aiguille optique à l'aide d'expériences *in vitro* sur des mires anthropomorphiques, ainsi que sur sa validation *in vivo* au cours d'une expérience animale. L'obtention d'une signature spectrale de réflectance diffuse et sa déconvolution pour retrouver les propriétés optiques des tissus étaient une étape préliminaire du projet de recherche au vu de la stratégie de sonde optique multimodale. Bien que le guidage des biopsies cérébrales et de la prostate constituent des problèmes cliniques bien distincts, il s'agit dans les deux cas de l'acquisition de mesures optiques interstitielles. Par conséquent les défis rencontrés lors de cette preuve de concept d'intégration en milieu clinique, et les réponses développées pour y faire face, constituent une expérience précieuse pour le travail de recherche poursuivi.

Ma contribution à cet article est constituée de la prise des mesures optiques *in vitro* en laboratoire sur les mires anthropomorphiques. Les mesures *in vivo* en salle opératoire sur l'animal ont été faites grâce à la collaboration du Dr Gilles Soulez (chercheur au CRCHUM) et du Dr Sami Obaid (résident en neurochirurgie au CHUM). J'ai aussi réalisé le traitement des données brutes pour reconstruire les images de tomographie interstitielle. J'ai développé les simulations de Monte-Carlo nécessaires à la méthode de déconvolution spectrale. Et je les ai implémentées pour extraire les propriétés optiques, définies en fonction de la longueur d'onde, des mesures de réflectance diffuse. Je suis également le contributeur principal au développement des figures et à la rédaction/publication de l'article.

3.2 Conception d'un nouveau prototype de sonde multimodale et évaluation de la stratégie d'acquisition des ensembles de données d'apprentissage

L'approche proposée pour la détection des cellules cancéreuses reposait sur un système multimodal à l'aide d'un nouveau prototype de sonde compatible avec la combinaison des sous-systèmes suivants :

- Spectroscopie par réflectance diffuse pour corriger les données de fluorescence, à l'aide d'une fibre optique sans filtre ajouté.
- Spectroscopie de fluorescence pour ajouter une source de contraste biomoléculaire, à l'aide de la même fibre optique.
- Spectroscopie Raman pour apporter le cœur de l'information biomoléculaire permettant de distinguer les tissus sains et cancéreux. Ce sous-système comprend une fibre d'illumination et neuf fibres de collection auxquelles sont apposées les filtres adéquats pour pouvoir mesurer les régions spectrales *fingerprint* et *high wavenumber*.

Le design de cette nouvelle sonde (figure 3.2) et sa fabrication ont été fait en collaboration avec Eric Marple (EmVision LLC). Les principales contraintes étaient d'inclure le capteur EM à l'extrémité distale de la sonde tout en conservant un maximum d'espace pour les fibres optiques et en assurant que le diamètre total externe soit inférieur à 1.3 mm. La première était liée au besoin clinique d'inclure la sonde dans le flux chirurgical de la procédure en la connectant à la plateforme de navigation TRUS-IRM grâce au guidage EM. La seconde était liée directement au matériel commercial utilisé pour la biopsie de la prostate, notamment les dimensions du canevas de guidage (figure 1.1) et de ses canules de guidage associées dont le diamètre interne est exactement 1.3 mm. Le développement du système EM, intégrant la sonde à la plateforme TRUS-IRM, fut réalisé par Roozbeh Shams (laboratoire MediCAL, Polytechnique Montréal).

Un défi majeur du projet de recherche était la difficulté à mener en parallèle le développement de trois sous-système optique indépendants, tout en les amenant au même niveau de maturité pour des tests en salle opératoire sur patients humains. Or la spectroscopie Raman était le sous-système principal, i.e. celui jugé avec le meilleur potentiel pour le diagnostic des tissus. La décision fut donc prise d'abandonner le développement des sous-systèmes de réflectance diffuse et de fluorescence ainsi que leur évaluation en salle opératoire. Les objectifs 2 et 3 furent redéfinis pour se concentrer sur l'intégration de la spectroscopie Raman, bien que le prototype final ait conservé la fibre optique sans filtre ajoutée nécessaire à ces deux autres sous-systèmes.

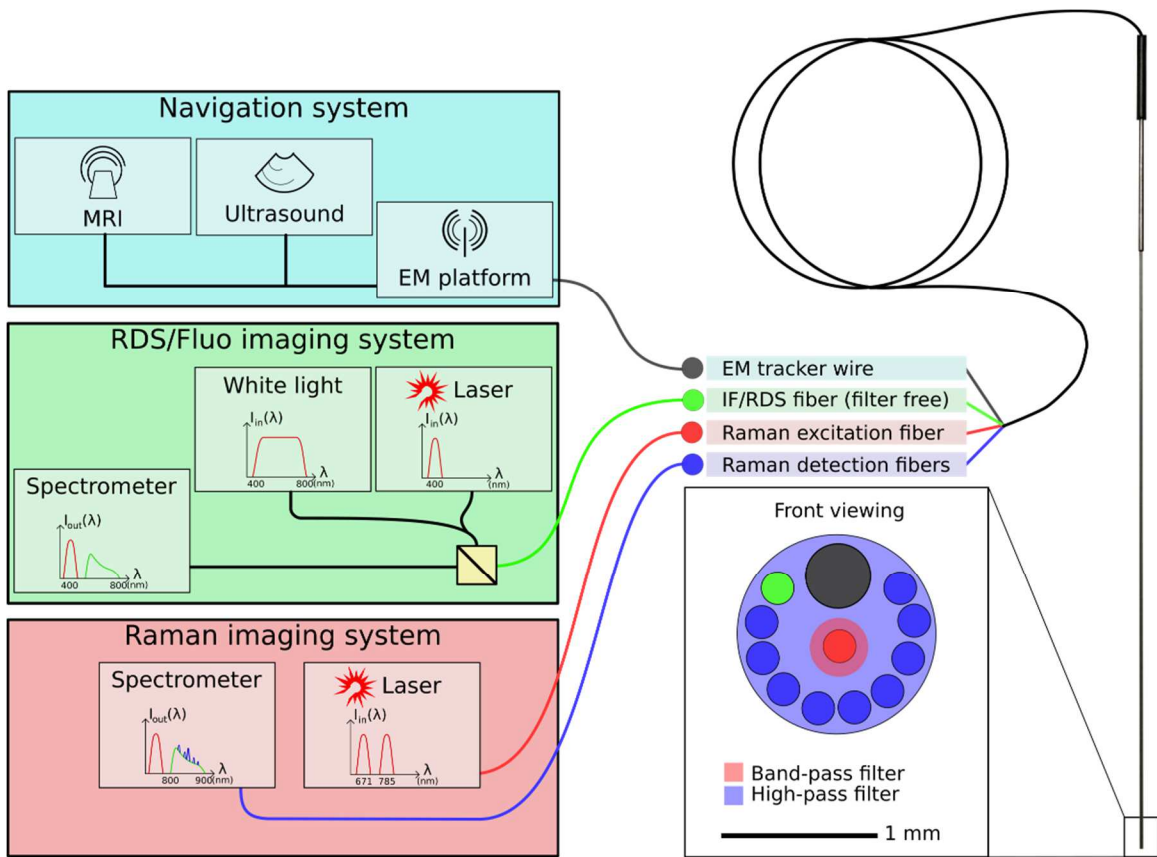


Figure 3.2 Schéma du système optique multimodal pour le guidage des biopsies de la prostate (sonde, sources lumineuses et spectromètres) couplé au système de navigation chirurgical (plateforme guidage EM).

Finalement la question de la taille prévue des ensembles de données s'est posée afin de pouvoir anticiper cette contrainte clinique sur le long terme. Une stratégie efficace pour le diagnostic des tissus à l'aide de la spectroscopie Raman est de construire une base de données d'apprentissage associant pour chaque signature Raman collectée, le diagnostic de l'échantillon dont elle est issue. Ce diagnostic, ou étiquette, est typiquement obtenu par l'étude histopathologique du tissu sondé et qui constitue alors l'échantillon standard. Or dans le cas de la procédure de biopsie de la prostate, l'obtention de ces deux informations, signature optique et échantillon pour étude histopathologique, est très coûteuse en temps et en argent. En collaboration avec la Dre Cynthia Ménard (Département radio-oncologie, CHUM), le nombre de mesures indépendantes, aussi appelées "points" de l'ensemble de donnée, a été prévu d'être compris entre

1 et 5 par patient. Avec une cohorte d'une vingtaine de patients cela conduit à un ensemble de données, pour l'apprentissage des modèles de diagnostic, d'une cinquantaine de points environ. Cela est suffisant pour une étude préliminaire mais pas pour une validation robuste de la spectroscopie Raman comme une solution au problème clinique.

Mon deuxième article intitulé “Data consistency and classification model transferability across biomedical Raman spectroscopy systems” (*Translational Biophotonics*) visait à répondre à ce problème en levant la limitation sur la possibilité d'études multicentriques basées sur les systèmes développés dans le LRO. Le but était de montrer que des sondes manufacturées par une méthode non industrielle induisait une différence de signal brute que notre méthode de traitement de données pouvait corriger. La réussite de cette étude rendrait alors possible l'utilisation de multiples prototypes afin de multiplier la vitesse d'acquisition des données et ainsi la taille des ensembles de données d'apprentissage. De plus, il est à noter que le prototype de la nouvelle sonde a été fabriqué en deux exemplaires, dans le but notamment de pouvoir augmenter le rythme des tests en salle opératoire. La validation de l'utilisation de multiples prototypes au sein d'une même étude était donc autant un objectif de long-terme que de court-terme. Ce deuxième article se concentre sur deux expériences, l'une sur une mire anthropomorphique et l'autre sur des échantillons *ex vivo* de cerveaux de singe, pour mettre en évidence la convergence des signaux Raman extraits d'un même échantillon avec différents systèmes.

Ma contribution à cet article est constituée de la prise des mesures optiques *in vitro* en laboratoire sur la mire anthropomorphique et *ex vivo* sur les échantillons de cerveaux de singe fournis par le centre de recherche CERVO de l'université Laval. J'ai réalisé le traitement des données ainsi que la construction des modèles de classification basées sur des algorithmes d'apprentissage machine. Je suis également le contributeur principal au développement des figures et à la rédaction/publication de l'article.

3.3 Étude clinique en salle opératoire au CHUM

L'objectif final de mon projet de recherche était de mener une étude préliminaire afin de détecter, grâce à des spectres Raman acquis *in situ*, le cancer de la prostate. Les deux premiers articles ont servi de préparation pour cette expérience. Le premier en étant une preuve de concept de

l'introduction d'une aiguille optique en milieu clinique, et le deuxième en optimisant les techniques de traitement de données ainsi que les méthodes statistiques de classification utilisées dans notre laboratoire. Ce troisième et dernier objectif est séparé en deux sous-objectifs testés indépendamment à l'aide deux expériences, *ex vivo* et *in vivo*. Dans les deux cas la méthodologie d'ensemble reste identique : il s'agit de collecter des spectres Raman sur des tissus de prostate humain et de les associer avec un diagnostic de référence obtenu grâce à une analyse histopathologique des échantillons sondés. Cet ensemble de données est par la suite utilisé pour entraîner un modèle de classification discriminant entre tissus sains et tissus cancéreux.

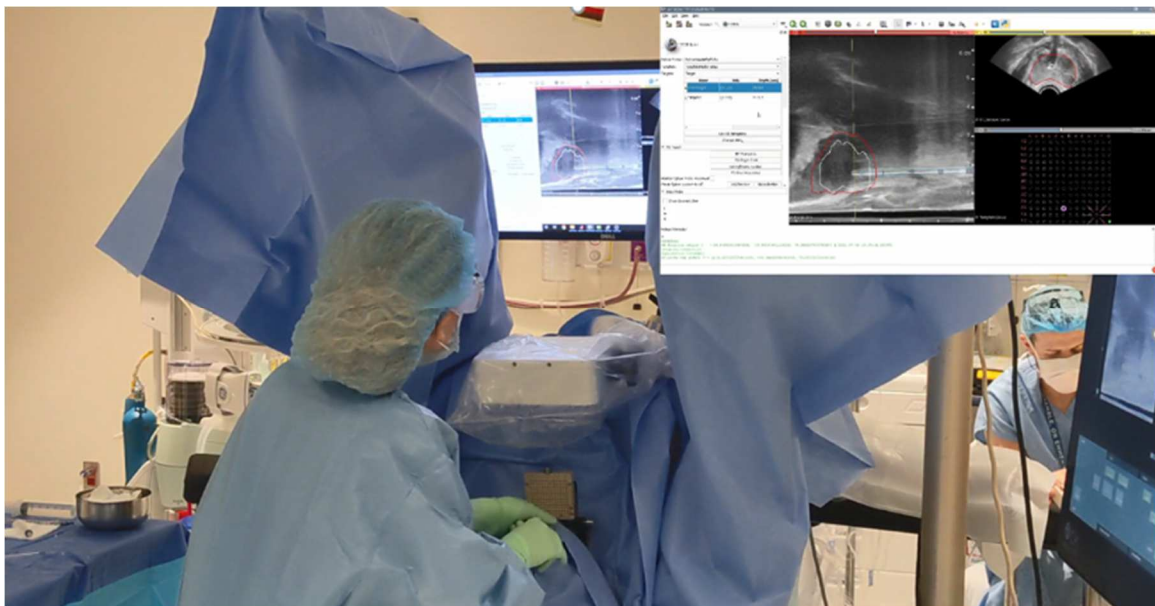


Figure 3.3 Photographie du prototype de sonde optique multimodal guidé, grâce à la plateforme TRUS-IRM-EM, lors d'une intervention de biopsie de la prostate sur un patient au CHUM.

Du fait de la nature et la forme des échantillons, les défis rencontrés se révèlent être très différents pour ces deux expériences. La première dans l'ordre chronologique, sur échantillons *ex vivo*, fut menée sur des coupes de prostate à la suite d'opérations de prostatectomie radicale. La seconde reposait sur une acquisition des spectres *in situ* (figure 3.3) suivie par la collecte d'échantillons de biopsie. Cette différence a introduit, dans le cas *ex vivo*, la problématique du recalage spatial entre la position de la mesure optique et celle de l'échantillon. De plus, les

contraintes liées à l'environnement étant moindre en laboratoire qu'en salle d'opération, l'expérience *ex vivo* fut également mis à profit pour optimiser le logiciel contrôlant le système. En collaboration avec Guillaume Sheehy (étudiant au doctorat du LRO), ce logiciel fut ainsi adapté pour permettre l'acquisition automatique des spectres Raman sur les deux régions spectrales d'intérêt, *fingerprint* et *high wavenumber*.

Mon troisième article intitulé “Image-guided Raman spectroscopy navigation system to improve transperineal prostate cancer detection. Part 1: Overview of Raman spectroscopy fiber-optics system and in-situ tissue characterization” (*Journal of Biomedical Optics*, facteur d'impact = 3.73) rassemble les résultats de ces deux expériences et constitue le résultat final de ma thèse. Ma contribution à cet article est constituée de la conception du système Raman, de la prise des mesures optiques *ex vivo* ainsi que de la méthode et la réalisation du recalage spatial entre les données optiques et les images histopathologiques servant au diagnostic de référence. L'acquisition des données *in situ* en salle opératoire a été faite avec la participation de Roozbeh Shams et David Grajales (laboratoire MediCAL, Polytechnique Montréal) et en collaboration avec la Dre Cynthia Ménard (chercheur au CRCHUM). Le traitement des données Raman et l'entraînement des modèles de classification pour les deux expériences a été fait en collaboration avec Frédéric Dallaire (postdoc du LRO). Je suis contributeur majoritaire au développement des figures et à la rédaction/publication de l'article.

CHAPITRE 4 ARTICLE 1: INTERSTITIAL IMAGING WITH MULTIPLE DIFFUSIVE REFLECTANCE SPECTROSCOPY PROJECTIONS FOR *IN VIVO* BLOOD VESSELS DETECTION DURING BRAIN NEEDLE BIOPSY PROCEDURES

Fabien Picot, Andréanne Goyette, Sami Obaid, Joannie Desroches, Simon Lessard, Marie-André Tremblay, Mathias Strupler, Brian Wilson, Kevin Petrecca, Gilles Soulez, Frédéric Leblond

Publié dans NEUROPHOTONICS, 23 avril 2019

4.1 Abstract

Blood vessel injury during image-guided brain biopsy poses a risk for hemorrhage. Approaches that reduce this risk may minimize related patient morbidity. We present here, a new intra-operative imaging device that has the potential to detect the brain vasculature *in situ*. The device uses multiple diffuse reflectance spectra acquired in an outward-viewing geometry to detect intravascular hemoglobin, enabling construction an optical image in the vicinity of the biopsy needle revealing proximity to blood vessels. This optical detection system seamlessly integrates into a commercial biopsy system without disruption to the neurosurgical clinical workflow. Using diffusive brain tissue phantoms, we show that this device can detect 0.5mm diameter absorptive carbon rods up to approximately 2 mm from the biopsy window. We also demonstrate feasibility and practicality of the technique in a clinical environment to detect brain vasculature in an *in vivo* model system. *In situ* brain vascular detection may add a layer of safety to image-guided biopsies and minimize patient morbidity.

4.2 Introduction

The standard-of-care for malignant brain tumors includes open-cranium surgery [128]–[135] to achieve maximal resection of cancer tissue followed by adjuvant therapies such as chemotherapy and radiotherapy [128]–[135]. However, surgery is not always the optimal treatment choice

because the risks associated with this procedure can outweigh potential benefits. This is especially important for patients with poor health or when lesions are difficult to access either because they are deeply seated or they are associated with multiple focal sites [128]–[135]. In those cases a brain needle biopsy can be performed to assess potential benefits of a surgical resection procedure by providing clinicians with a more precise diagnosis. During the biopsy procedure bleeding can occur in 0.3% to 59.8% of cases [136]–[141]. While most of these instances of tissue damage are asymptomatic or can lead to minor transient effects (e.g. dizziness, headaches), more serious consequences can result from brain biopsy procedures because of damage incurred to larger and more critical blood vessels. For example, there is a small yet non-negligible mortality risk (up to 3.9% in some studies) associated with this procedure [136], [142]–[144].

Several optical imaging techniques are currently being developed for intraoperative blood vessels detection. Methods were developed using the fluorescence from Indocyanine green (ICG) to help guide procedures in the ocular fundus, in laparoscopic surgery, in stereotactic brain surgery, for robot-assisted cardiac procedures and for esophagectomy [145]–[149]. A promising method for intraoperative blood vessels detection is optical coherence tomography (OCT) which has been successfully developed for visualization of retinal vasculature as well as for blood vessel detection in rodent brain [150]–[152]. Although OCT cannot interrogate areas larger than a few millimeters across, whereas fluorescence can be used for macroscopic imaging (several centimeters across), advantages of OCT are its volumetric imaging capabilities (up to 1-2 mm depth sampling mostly depending on tissue absorption) and the fact it does not rely on the administration of an exogenous contrast agent. Fluorescence and OCT were also combined in some studies to enhance the visualization of blood vessels [153]–[155] and more recently an OCT imaging needle successfully demonstrated its ability to detect blood vessels in humans brain surgery. In that study [156] OCT can provide high-resolution images in real time and in particular Doppler OCT can provide specific blood vessels detection due to its inherent ability for motion detection. However, the requirement to provide imaging capabilities (e.g. possibly using a mechanical scanning device) makes it difficult to integrate OCT technology into existing commercial biopsy devices, thereby typically requiring an extra step to the procedural biopsy sample harvesting workflow. Other optical imaging techniques that could be developed for interstitial and intraoperative blood vessels detection include laser Doppler imaging. For this technique light scattering from moving molecules result in a frequency shift and collecting Doppler-shifted scattered photons interacting with blood vessels

provide blood flow information [157], [158]. This method was already successfully implemented in human brain [159]. And another study introduces a new Doppler probe embedded on a needle to fit the requirements for blood vessels detection during brain biopsy procedures [160]. In a similar way, speckle imaging uses the fluctuation in interference light patterns to reconstruct movement in the scattering medium. This technique has shown it can detect superficial blood flow in animals and humans *in vivo* studies [161], [162].

In previous work, we have introduced interstitial diffuse optical tomography and demonstrated its ability to detect highly absorbing inclusions in tissue-simulating diffusing phantoms [45], [163]. The technique was first introduced in [163] where a proof-of-concept study was presented using a realistic brain tissue phantom to demonstrate optical tomography can detect several 1 mm diameter high-contrast absorbing objects located <2 mm from the edge of a needle. Following our initial work, [45] presented a more detailed sensitivity analysis establishing the intrinsic detection limits of the method based on simulations and experiments using brain tissue phantoms. It was demonstrated that absorbers can be detected with diameters >300 μm located up to >2 mm from the biopsy needle core for bulk optical properties consistent with brain tissue. The clinical need to improve safety requires the detection of blood vessels within up to 2 mm from the outer surface of the needle, since this distance is representative of the volume of tissue that is aspirated during tissue extraction. This preliminary work was a proof-of-principle providing evidence this new method could be used for the detection of blood vessels (either large vessels or areas containing high densities of small micro-vessels) during brain needle biopsy procedures in order to minimize hemorrhage risk. Here we are presenting the next step in this research where a protocol was developed and implemented for *in vivo* swine brain diffuse optical imaging during a brain biopsy procedure. This animal proof-of-principle demonstrates that multiple projection diffuse reflectance spectroscopy could be used to guide the insertion of brain biopsy needles by using hemoglobin as a surrogate for blood vessels detection prior to sample harvesting. Specifically, we are presenting the development of an intraoperative biopsy needle with an integrated multi-projections diffuse optical fiber optics spectroscopy system to detect blood vessels in the vicinity of the biopsy window with the objective of improving procedural safety of the procedure. We first detail the design and fabrication method for the needle probe that is directly integrated onto a commercial brain biopsy system. An *in vitro* proof-of-concept study using phantoms made of carbon rods and IntralipidTM is then presented to demonstrate the feasibility of

absorptive inclusions detection in a scattering medium. Finally, we present intraoperative blood vessel detection *in vivo* during one swine brain biopsy procedure using the diffuse optics imaging system to demonstrate feasibility and practicality of the technique in a clinical environment. The algorithms for light transport modeling and imaging are also briefly detailed.

4.3 Methods

4.3.1 Imaging system

4.3.1.1 Optical brain biopsy needle

The diffuse reflectance fiber optics system was integrated directly onto the outer cannula of a commercial brain biopsy needle (model 9733068, Medtronic, CO, USA) as shown in Figure 4.1. The commercial brain biopsy needle is composed of two hollow tubes herein labeled as the inner and the outer cannulas (Figure 4.1). The outer cannula is 20 cm in length with an outer diameter of 2 mm. At the distal end of each cannula, there is a small rectangular opening (henceforth referred to as the biopsy window) of dimensions 1.5 mm x 8 mm through which a sample can be aspirated, cut (through rapid rotation of the inner cannula relative to the outer cannula) and then harvested for pathology analyses. A requirement for the design of the optical biopsy needle was to ensure the imaging system could be integrated directly on a commercial biopsy needle for minimal disruption of the surgical workflow. The integrated probe consisted of 18 optical fibers (NA 0.22, Low-OH, 105 μ m core diameter, FG105LCA, Thorlabs, USA) disposed circumferentially around a 200° portion of the outer cannula of the commercial brain biopsy needle, leaving a blind spot (Figure 4.1). The fibers were disposed opposite the biopsy window and the angular range they cover was limited in order to leave the later unobstructed. As a result, imaging could be achieved on the opposite side of the window, hence the need to rotate the probe by 180° between optical measurement and tissue collection. The probe design was compatible with the use of a standard stereotactic frame used for needle guidance, which allowed to precisely control its rotation angle to ensure spatial registration between imaging and tissue harvesting locations. A custom metallic angled aluminum mirror (45° inclination) was fixed at the tip of the probe to allow tissue illumination and light detection perpendicular to the needle. The optical fibers were glued with fast curing optical adhesive (NOA81, Thorlabs, USA) on a thin open-ended hollow metallic tube (2.11

mm internal diameter, 2.24 mm external diameter) that could fit onto the external cannula of the commercial brain biopsy needle (2.11 mm external diameter). The diameter of the resulting assembly was 2.49 mm, including the external cannula, the hollow tube and the fibers covered by a layer of optical glue for protection. The center-to-center distance between adjacent optical fibers was approximately 100 μm .

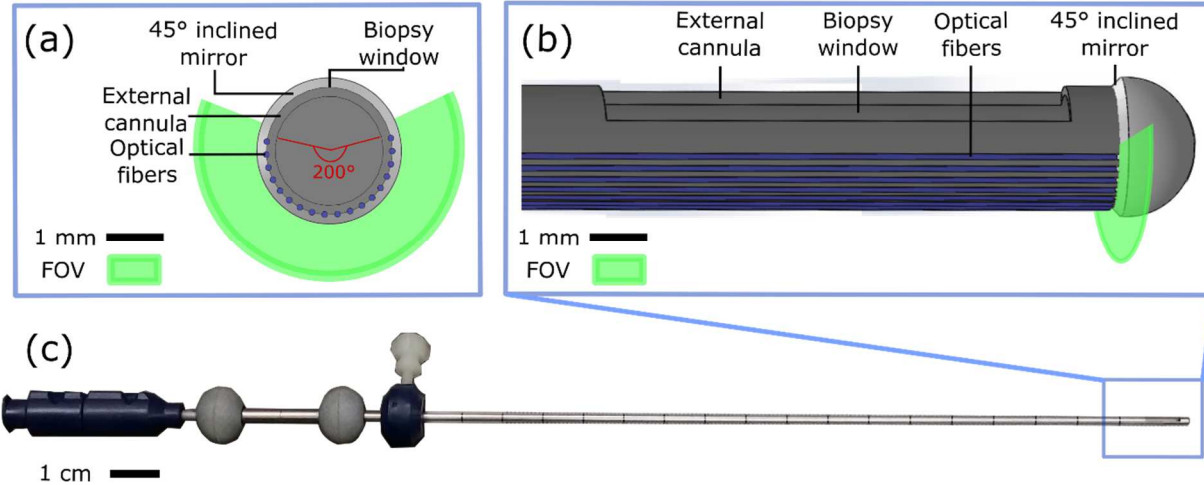


Figure 4.1 Optical probe design showing the distribution of the optical fibers around the needle as well as the position of the mirror. Only the external cannula of the commercial needle is shown, with the optical fibers (in blue) disposed on its exterior surface: (a) transverse view and (b) longitudinal view of the optical needle shown in (c).

4.3.1.2 Illumination/detection system

A fibered illumination/detection system was connected to the 18 optical fibers of the needle through SMA connectors (Figure 4.2). A white light source (HL-2000 HP232, 450-1100 nm, Ocean Optics, USA) was coupled to 9 of the biopsy needle fibers using a mechanical optical switch (16-to-1 switch, MPM-2000, Ocean Optics, USA). The illumination fibers (labeled with even numbers) alternated with the 9 detection fibers on the biopsy needle (labeled with odd numbers). The latter were linked to another mechanical optical switch conducting the incoming light to a high-sensitivity spectrometer (QE65 Pro, Ocean Optics, USA). The system was controlled using a custom Labview (National Instruments, USA) program, automatically acquiring and storing

reflectance spectra for all combinations of the illumination and detection fibers. Since there were 9 detection fibers and 9 illumination fibers, 81 spectra in total could be acquired with the system. The acquisition time was the sum of the integration times for each spectrum plus an overall 500 ms delay associated with the motion of the mechanical components in the optical switches. In total, 13 mW was delivered to the distal end of the fibers for each illumination point.

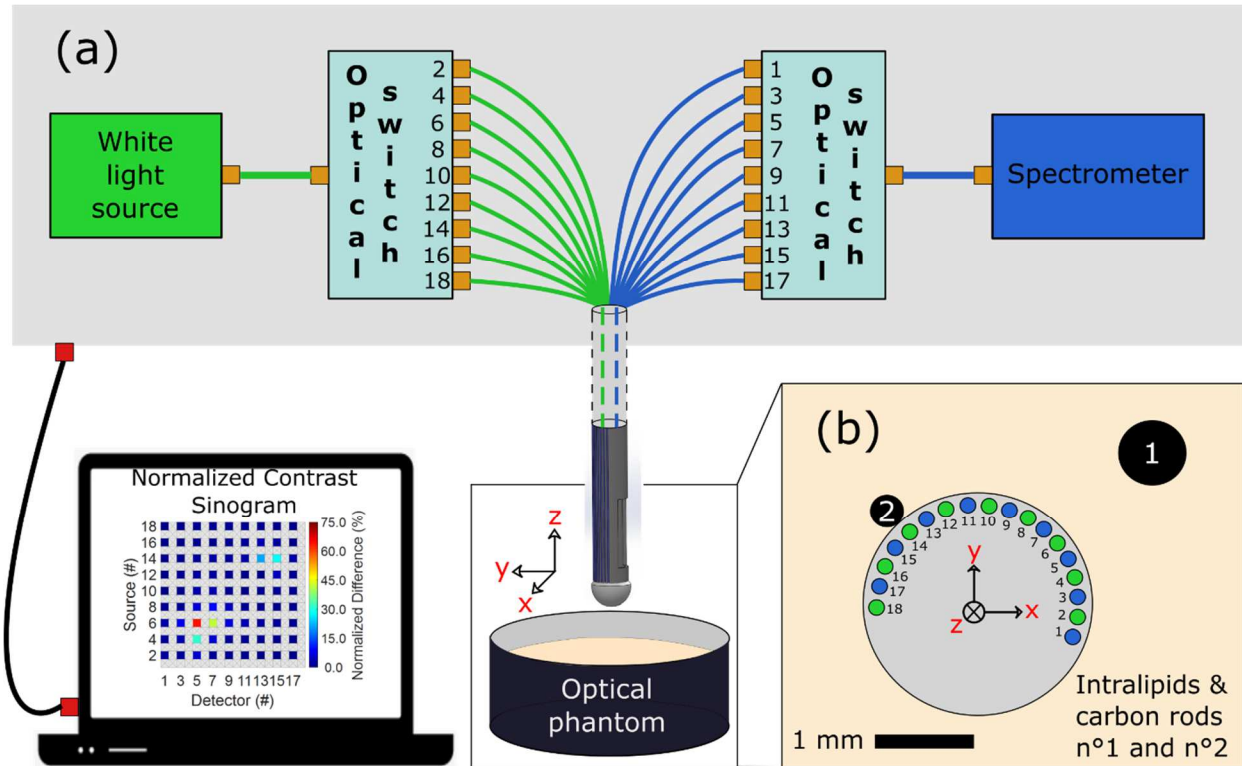


Figure 4.2 (a) Schematics of the optical system showing the white-light source and the spectrometer connected to mechanical fiber switches allowing wide-angle interrogation when the needle is immersed in a tissue phantom composed of multiple inclusions (black carbon rods) embedded in a scattering medium (Intralipid™). (b) Geometrical test configuration around the optical biopsy needle where each of the 9 potentially active fiber sources are identified with an even number while the 9 detection sources are identified with an odd number. Those numbers are associated with the numbering scheme used to identify the optical switches positions in (a).

4.3.2 Tissue phantom experiments

An experimental protocol was developed to test whether or not the new system was able to perform at the same level as the previous interstitial probe based on a stand-alone design that was not integrated onto a commercial biopsy needle [163]. To this end, optical phantoms were fabricated to reproduce the geometrical and optical properties of human brain under the assumption absorption was mostly due to hemoglobin (Hb), and that scattering was approximately two orders of magnitude larger than absorption [126], [164]. The bulk medium associated with the diffusive phantoms was composed of a solution of Intralipid™ to emulate scattering (20%, 1:4 V/V) and blue coloring dye diluted in water for background absorption (1:1000 V/V). Two high absorption carbon rods (outer diameters: 720 μm for inclusion 1, 310 μm for inclusion 2; see Figure 4.2) were used to provide optical contrast to model blood vessels. The biopsy needle was affixed to a support allowing its position in the bulk medium to be controlled using a 3-axis translation stage (PT3, Thorlabs, USA). Several parameters were allowed to vary in the experiments: 1) images were acquired with a varying distance between inclusion 1 and the needle, with a fixed distance between inclusion 2 and the probe, 2) an image was acquired with the bulk medium composed only of Intralipid™ (no blue dye) as a reference for data normalization. For each dataset, the edge-to-edge distances between inclusion 2 and the optical biopsy needle were: 0, 50, 100, 200, 500, 1000 and 2000 μm . This resulted in 7 images reconstructed using 81 reflectance spectra (i.e., all possible combinations of illumination/detection fibers) with an integration time for the reflectance spectra increasing from 1 to 5 s, with larger imaging times used for larger source-detector distances. The optimal integration time was estimated for each pair of fibers to maximize usage of the dynamical range of the sensor.

4.3.3 Optical reconstruction algorithm

The reconstruction algorithm developed in [45] was used to image variations in optical absorption from a heterogeneous medium based on differences between data acquired in the heterogeneous medium (targeted for reconstruction) and calibration data acquired in a homogeneous medium. The technique was inspired from modeling approaches developed in diffuse optical tomography when solving the diffusion equation in the Rytov or Born approximation under the assumption that local

variations in optical properties (μ_a , μ_s') can be treated as perturbations [33], [165]. Briefly, input data for each source/detector (S/D) pair associated with a spectral band of width $\Delta\lambda$ (between wavelengths λ_i and λ_f) was modeled using the following equation, where the approximation was made that the reduced scattering coefficient was constant across the imaging domain:

$$I_{S/D}^{homogeneous} - I_{S/D}^{heterogeneous} = \int J(\vec{r}, \vec{r}_S, \vec{r}_D) \delta\mu_a(\vec{r}) d\vec{r} \quad (1)$$

where $I_{S/D}$ is the signal intensity, $\delta\mu_a(\vec{r})$ is the local difference in absorption coefficient between homogeneous and heterogeneous media, and $J(\vec{r}, \vec{r}_S, \vec{r}_D)$ is the numerical sensitivity function between source S and detector D obtained using Monte Carlo light transport simulations [43], [166]. The latter function was obtained for the S/D geometry associated with the fibers distribution around the needle for a homogenous background. Then for each S/D pair an estimate was computed for the variation $\delta\mu_a$ with respect to the homogenous background. This was achieved based on Eq. (1) under the approximation that optical properties variations are constant across the imaging domain:

$$\delta\mu_a^{S,D} = \frac{I_{S/D}^{homogeneous} - I_{S/D}^{heterogeneous}}{\int J(\vec{r}, \vec{r}_S, \vec{r}_D) d\vec{r}} \quad (2)$$

Physically, this formula was used to assign to each S/D measurement a weight quantifying its relative contribution with respect to other measurements when contributing to variations in optical properties. Finally, a reconstructed image was computed by superposing the sensitivity function for all S/D pairs, each weighted by the estimate for $\delta\mu_a^{S,D}$.

Reconstruction process can be achieved for any spectral band by using intensities in Eqs. (1, 2) associated with the integral of the diffuse reflectance spectra over the desired spectral domain between λ_i and λ_f . Integrals of the whole diffusion spectra was used for the tissue phantom experiments (section 4.3.2) but a spectral band around the 575 nm ($\Delta\lambda = 10$ nm) hemoglobin peak was used for the *in vivo* experiments (see section 2.4 below) to ensure images are reconstructed that are as specific as possible to blood vessels [167], [168]. The calibration data (homogenous medium) used for the swine brain experiments consisted in reflectance spectra from an Intralipid™ and blue dye phantom designed to match as closely as possible literature values for brain tissue optical properties ($\mu_a = 0.1 \text{ mm}^{-1}$ [168], [169], and $\mu'_s \sim 8 \text{ mm}^{-1}$ [169]). To discriminate blood vessels from non vascular tissue we used equation (2), with $I_{S/D}^{homogeneous}$ as the intensity collected for the

calibration phantom and $I_{S/D}^{heterogeneous}$ the intensity from the interrogated medium. The weighted differences $\delta\mu_a^{S,D}$ were then thresholded keeping only values at 50%, or higher, of the maximum value for the whole dataset. This threshold was a free parameter of the processing we used to maximize the correlation between the reconstructed images and the X-ray images used for *in vivo* validation of the technique. A more sophisticated model, based on Monte-Carlo simulations, was also developed to retrieve the optical absorption coefficient μ_a of the medium under the assumption of constant reduced scattering coefficient ($\mu'_s = 8 \text{ mm}^{-1}$ for brain tissue [126], [163], [164]) Briefly, diffuse reflectance spectra were generated based on Monte Carlo simulations for a range of optical properties consistent with brain tissue. Then, using a least-squares algorithm the resulting spectral look-up table was used to associate absorption coefficient values for each wavelength of all experimental reflectance spectra. Using a curve fitting with a linear regression, each resulting μ_a spectrum was projected onto a basis composed of the extinction coefficients of oxygenated and deoxygenated hemoglobin to retrieve their relative contributions. The resulting fitted hemoglobin absorption spectra were used for image reconstruction only when $\mu_a > 0.4 \text{ mm}^{-1}$ in the 575 nm band because this threshold was found to most consistently reconstruct vessels detected with the gold standard of X-ray imaging. However the images reconstructed with this spectral method led to the same blood vessels detection assessment when compared to Figure 4.6, and as a result they are not shown for conciseness.

4.3.4 *In vivo* data acquisition protocol

To demonstrate the technical feasibility of using the optical brain biopsy system in an operating room, as well as its capacity for intraoperative detection of blood vessels, an *in vivo* experiment was designed and conducted during which it was used in a living adult swine (male, approximately 30 kg). In this experiment the gold standard for blood vessels detection against which to evaluate the new technique was X-ray imaging. The animal ethics protocol was approved by the Comité institutionnel de protection des animaux (CIPA) at the Centre de recherche du Centre hospitalier de l'Université de Montréal (CRCHUM) in accordance with the Canadian Council on Animal Care (CCAC) guidelines. The animal was kept under general anesthesia during the entire experiment. The anesthesia was terminal.

Prior to the surgical procedure, the surgeon used two 3D imaging operating modes of the X-ray system (Artis Q, Siemens, Germany). The first was computed tomography (CT, 20 s acquisition per scan, 1 frame every 0.5° , 217° in total, $500\text{ }\mu\text{m}$ resolution). The second imaging mode was angiography ($250\text{ }\mu\text{m}$ resolution), obtained by subtracting two CT scans. For angiography, the second scan differed from the first because the contrast agent IodixanolTM was injected (270 mg/mL , 2 mL/s , 50 mL) to highlight blood vessels. The contrast agent was injected through a catheter into the femoral artery 5 s before image acquisition to ensure it had spread into the arteries. Based on the imaging results (3D image of the arteries), the surgeon planned a biopsy needle insertion trajectory minimizing the risks of damages to critical vessels. Although angiography had superior spatial resolution, CT scan images were shown to be more sensitive to vessels and thus used to provide a post-operative reference in order to preliminarily assess the ability of the optical biopsy system to detect the presence of blood vessels.

During insertion of the biopsy needle, the fluoroscopy modality of the X-ray imaging system was used as a guide. Two 2D fluoroshots were saved at several points along the trajectory and combined to retrieve the 3D location of the biopsy tool. At each imaging position, 30 reflectance spectra were acquired to reconstruct an image instead of the 81 used previously in the in vitro experiments. This constraint was imposed by the need to ensure that the full procedure was kept under 60 minutes as stipulated in the animal protocol. This resulted in an integration time of 55 seconds per image for each of the 9 different depth locations along the trajectory of the optical biopsy needle. The spatial insertion step between two locations along the trajectory of the needle was $\sim 3\text{ mm}$. After the 9th acquisition, the target was reached covering a total insertion length of 23 mm from the initial depth. The optical biopsy needle was then removed. Each spatial position where optical data was acquired was then retrieved from the 2D fluoroshots and merged with a CT scan. This resulted in a 3D image map of blood vessels in the brain over which the trajectory of the needle was superposed. Image merging was done using the Medical Imaging Interaction Toolkit (MITK) [170] to provide reference data for blood vessels localization. Uncertainty of the procedure associated with pre-op imaging and spatial registration errors associated with disrupton of the vessels. Quantitative estimation of the registration error is left for future work and remains here evaluated to approximately 1-2 mm.

4.4 Results

4.4.1 Tissue phantom experiment

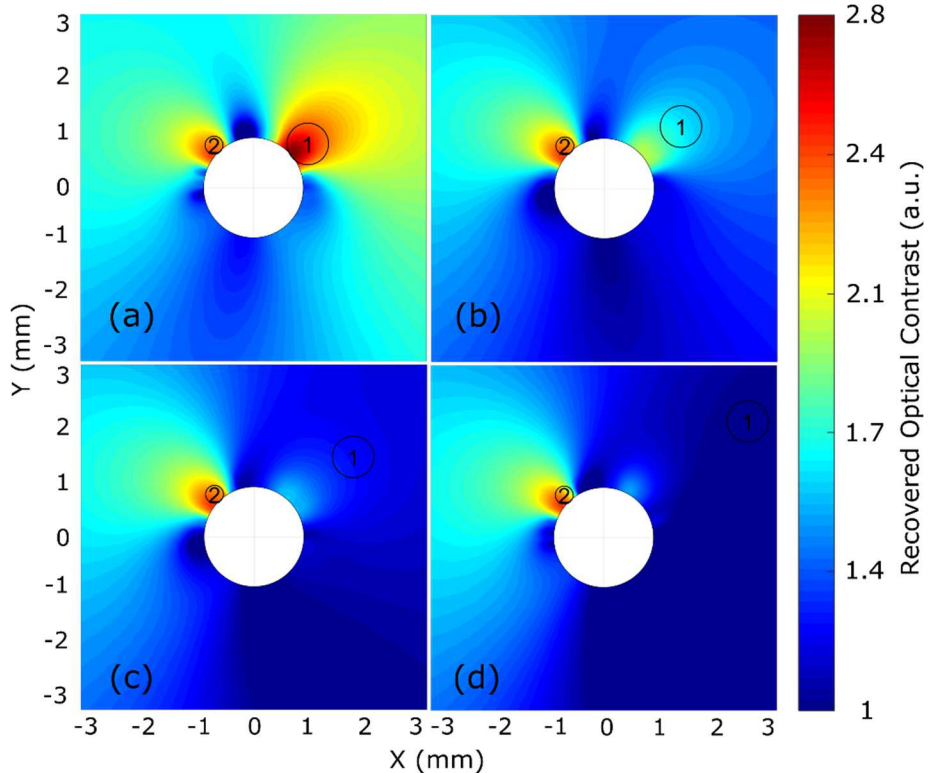


Figure 4.3 Reconstructed diffuse optics images of carbon rods immersed in a diffusive medium. The distances (edge-to-edge) between the optical biopsy needle and inclusion 1 is: a) 0 mm, b) 0.5 mm, c) 1 mm, and d) 2 mm. The other carbon rod (inclusion 2) remained at the same position in all experiments.

The aim of the phantom experiments was to reproduce a subset of results obtained in [45], [163] with a different probe design in order to demonstrate that the current system can also localize highly absorbing inclusions. For succinctness, images are presented only for a subset of the phantoms that were studied. Figure 4.3 shows reconstruction results of 4 out of the 28 phantoms that were imaged in this work. The figure shows images of carbon rods immersed in a diffusive medium with optical properties $\mu_a = 0.01 \text{ mm}^{-1}$ and $\mu_s' = 8 \text{ mm}^{-1}$, with edge-to-edge distances between the optical biopsy needle and inclusion 1: a) 0 mm, b) 0.5 mm, c) 1 mm, and d) 2 mm. The other carbon rod (inclusion

2) remained at the same position in all four phantoms. For each image, the location of the carbon rods is indicated with black circles while the color scale values (contrast) can be interpreted as being proportional to the probability that an absorber is present at the location of a given pixel. The cross-section of the biopsy needle is represented with the white circle in the center of each image. The results in Figure 4.3 demonstrate a match between the estimated angular location of the inclusion around the probe and its actual position for each of the four datasets. Furthermore, the decrease of the optical contrast when inclusion 1 is moved away from the edge of the probe shows the radial sensitivity of the system to be on the order of 2 mm from the edge of the probe. This is consistent with the radial sensitivity found in [45], [163], and this finding is also supported by the reconstructed images (not shown for conciseness) of the other 24 phantoms with different background optical properties. Here depth sensitivity to inclusion 1 was assessed based on whether or not contrast could be observed in the radial direction from the needle to the inclusion. For example, although small for larger distances between inclusion 1 and the needle, contrast could still be observed up to an edge-to-edge separation of 2 mm despite the presence of a large contrast absorber next to the needle (inclusion 2). Each measured spectrum satisfied the requirement that its SNR was superior to 5, using the formula $\text{SNR} = \sqrt{I}$, where I is the number of photons counts in the 450-950 nm spectral band. For this experiment the SNR value estimated for each reflectance spectra was between 7 and 83, with an average value of 22 and a standard deviation of 18.

4.4.2 *In vivo* experiment

To evaluate the potential of the system to detect blood vessels *in vivo*, the 3D CT image map was analyzed for use as the gold standard for vessels detection. Figure 4.4a shows a large field of view image of the CT volume while Figure 4.4b shows an enlarged view around the vicinity of the probe. In that enlarged view the needle is shown in white whereas the system holding it (made of a titanium tube and three screws) and the detected vessels are all shown in red. The large field of view image in the figure shows the swine skull along with the holding system and the needle. The reconstruction of the blood vessels network inside the brain provides the information necessary to estimate the location and the size of the vessels in the close vicinity of the needle. The precision for the vessels localization is limited by the error registration of the probe and the 3D CT image map roughly estimated to 1 mm.

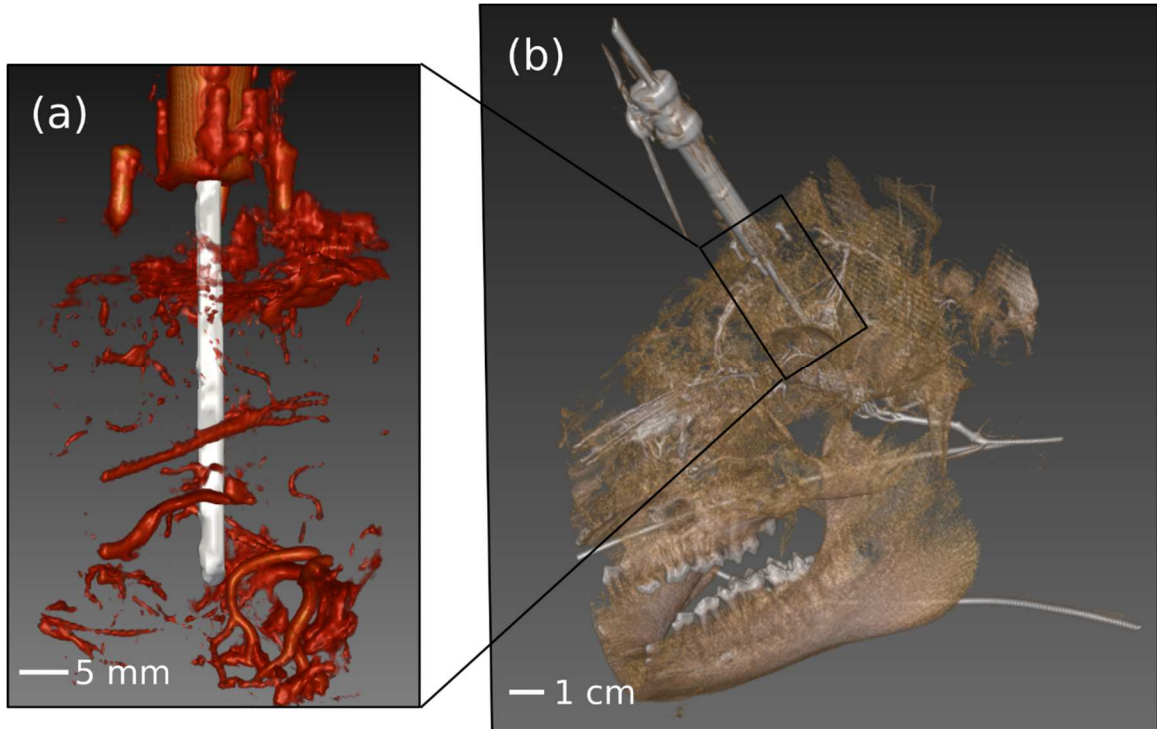


Figure 4.4 Computed tomography (CT) scan used to locate blood vessels in the vicinity of the biopsy needle: (a) representation of blood vessels (red) surrounding the optical biopsy needle (grey tubular object), (b) 3D reconstruction of the surgical field in semi-transparence showing the needle (in grey), the swine skull (in brown) and the blood vessels (in white).

Figure 4.5 shows two representative diffuse reflection spectra out of the 30 that were acquired per biopsy needle position, along with the calibration spectrum associated with a homogenous medium. Each spectrum in the figure shows characteristic features of the hemoglobin absorption signature including an increased absorption around 575 nm. The figure also shows the optical sinogram for one needle position, which graphically represents intensities associated with all 30 reflectance spectra with the detector number on the vertical axis and the source number on the horizontal axis. The intensity values in the sinogram are associated with the difference between the *in vivo* data and the calibration data (homogenous medium) at 575 nm. The sinogram data are used directly as input in Eq. (2) for image reconstruction. For this experiment, each measured spectrum used for image reconstruction satisfied the requirement that its SNR was superior to 5 in the spectral range 570-580 nm. The SNR value estimated for each reflectance spectra was then between 5 and 107, with an average value of 38 and a standard deviation of 22.

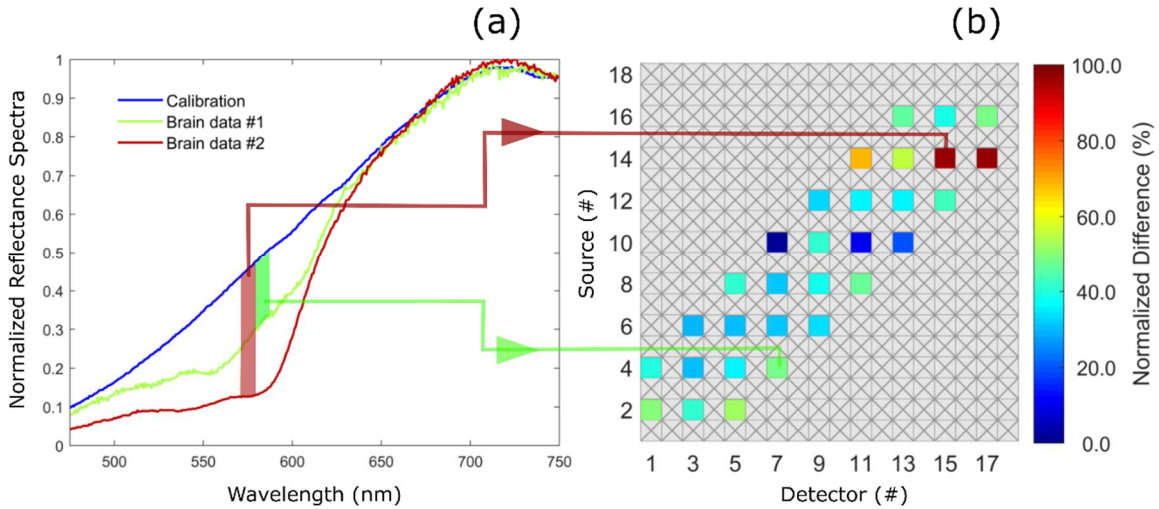


Figure 4.5 (a) Representative *in vivo* diffuse reflectance spectra and (b) optical sinogram associated with an interstitial measurement in swine brain.

Figure 4.6 shows a 3D representation of the blood vessels distribution detected in swine brain using CT and diffuse optics. For comparison purposes, each of the nine diffuse optics 2D images (Figure 4.6a) were juxtaposed with their corresponding 2D CT slice from the full 3D volume to assess the potential of the optical needle system to detect vessels. Importantly, all diffuse reflectance spectra were inspected and showed characteristic features of hemoglobin, confirming that the optical contrast was not provided by the X-ray contrast agent itself, which had cleared the vessels network at the moment when the diffuse reflectance images were acquired. The hemoglobin features themselves are the high optical absorption in the near 570-580 nm region and the low absorption elsewhere in the spectral range of the imaging system. An experienced radiologist (GS) analyzed the CT images to discriminate vessels from image noise and was able to confirm that the contrast observed in Figure 4.6b is associated with blood vessels. For the slices at depth 3, 6, 15, 18, 21 and 23 mm, both the diffuse optics and the CT slice are consistent with an absence of blood vessels. There is also a match for depths 0 and 12 mm where contrast is observed in both the diffuse optics and the CT images. However, the slice at depth 9 mm can be considered as a false negative for diffuse optics since the CT scan image shows blood vessel contrast not detected with the optical imaging system.

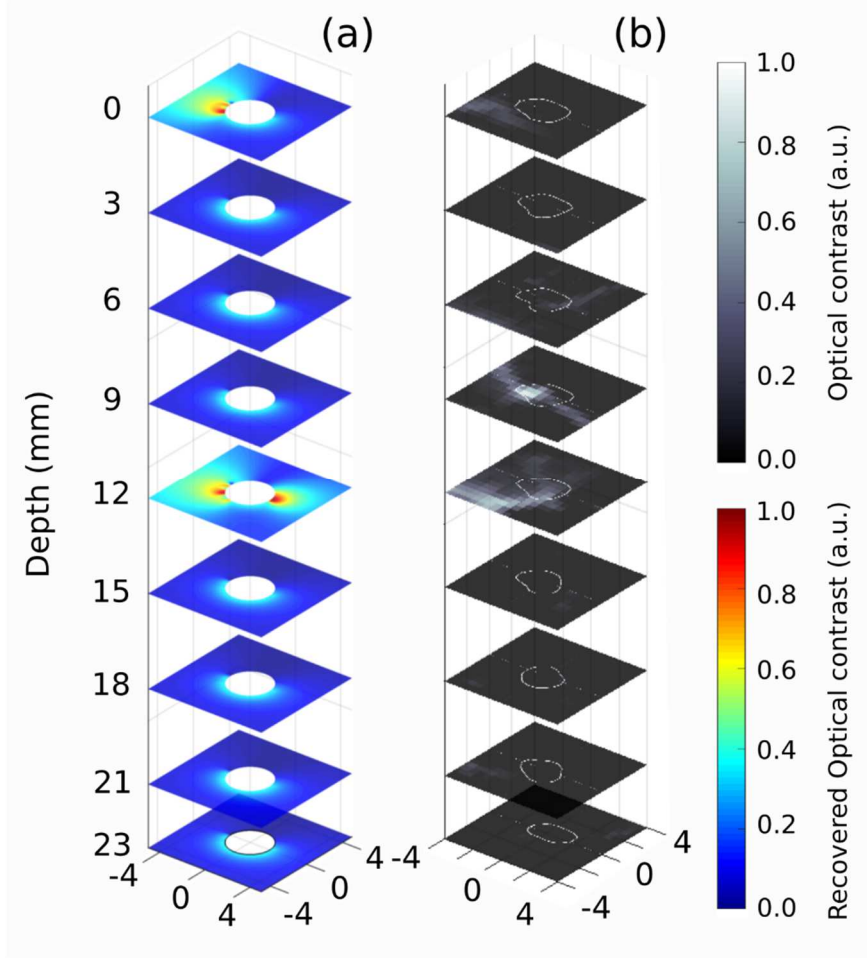


Figure 4.6 Comparison of spatially coincident images: (a) diffuse optical reconstructions, (b) CT scan (x- and y-axis units are in mm).

4.5 Discussion

The preliminarily *in vivo* results presented in this work suggest that a diffuse optics technique could detect blood vessels using hemoglobin absorption as a surrogate for blood vessels, as demonstrated by comparison with contrast CT used here as the gold standard for vessels detection. In its current form we believe the system presents features making in-human clinical translation eventually possible. For example, the technique could be used intraoperatively since the number of steps needed to manipulate the needle inside the brain is limited and does not require the use of any contrast agent.

Although the current optical reconstruction algorithm was able to detect high-absorbing inclusions in a diffusive medium up to ~2 mm from the needle core, it remains limited in terms of depth specificity, making it almost impossible to differentiate a large inclusion away from the edge of the needle and a smaller one in a closest range. As proposed in [40], this limitation could be overcome by using a more sophisticated reconstruction algorithm akin to diffuse optical tomography albeit adapted to an outside-viewing interstitial imaging geometry. Furthermore the method used to merge CT and diffuse optics images is inherently limited and prone to errors. This is because the CT image used as the gold standard was acquired prior to inserting the biopsy needle into the brain. As a result, needle insertion may have incurred shifts in vessels positions introducing a spatial mismatch between the high contrast locations predicted by both methods. For example, the false negative vessels detection for diffuse optics in Figure 4.6b might simply be a consequence of the vessels seen in the CT slice having moved in front of the dead angle of the optical detection system. To solve this problem, we considered acquiring the CT scan only once the optical biopsy needle was inserted instead of prior to. However this was made impossible due to artefacts caused by the metal in the needle and the limited imaging time allowed by the ethics protocol.

Several aspects are in need of improvement prior to first in-human testing. Most importantly, the diffuse optics imaging time per needle position needs to be reduced to <1s in order to minimize disruption of the surgical workflow; here the total *in vivo* imaging time was 55 s. However, this was achieved by using only a limited number of source-detector fiber pairs, namely only those for which the angular separation did not exceed 23°. While this reduced the integration time significantly (from ~7 minutes to 55 s), using a limited number of fibers also reduced the sensitivity of the system, potentially explaining the false negative diffuse optics image in Figure 4.4 for the slice at depth 9 mm. Ensuring that all fibers are used for a total integration <1 s can be achieved through a system redesign where instead of using a white-light lamp and a spectrometer, a simple laser diode centered at 575 nm is used in conjunction with an array of single-point detectors (e.g., photomultiplier tube or avalanche photodiode), each dedicated to one detection fiber. Light delivery to tissue in the current prototype was also highly inefficient because of sub-optimal fiber optics couplings leading to light doses delivered to tissue at least two orders of magnitude smaller than the maximum permissible exposure (MPE) limits for skin. As a result, integration time could

be reduced dramatically by simply improving the optical design and using a higher power light source.

Future work will also involve the conduct of a clinical study and the development of a validation protocol of the new technique based on pre-operative contrast-enhanced magnetic resonance imaging (MRI) rather than contrast CT because the latter is not a neuro-imaging standard in oncology. Specifically, the protocol will involve tracking the needle position in real time using a neuronavigation system allowing pre-op MR images to be spatially registered with each position where an optical measurement and a biopsy sample are collected. The presence of tissue damage associated with tissue harvesting will be assessed based on histopathology analyses and the presence of micro-vessels determined using immunohistochemistry using appropriate markers. While the current approach can potentially improve the safety of brain biopsy procedures, an instrument synergistically integrating a bio-molecular detection modality (e.g., Raman spectroscopy [57], [98], [171], [172]) with the diffuse optics approach could increase the diagnostic yield of the procedure to reduce instances of repeat procedures and limit the number of biopsy samples per procedure.

4.6 Conclusion

We have designed, fabricated, and validated a diffuse optical imaging system directly integrated on a commercial biopsy needle with the objective to detect blood vessels interstitially in the brain. The capabilities of the instrument were first demonstrated through an *in vitro* experiment using tissue phantoms to show that it can detect high absorbing inclusions within a diffusive medium. *In vivo* results in one animal were also presented to demonstrate feasibility and practicality of the technique in a clinical environment as well as the application of a protocol using CT imaging to validate the blood vessel detection capabilities of the optical system.

4.7 Disclosures

We do not declare any conflict of interest concerning this study.

4.8 Acknowledgments

This work is supported by the Discovery Grant program from Natural Sciences and Engineering Research Council of Canada (NSERC), the Collaborative Health Research Program (CIHR and NSERC), and the company Medtronic, which provided support with the commercial brain biopsy needles. We would also like to thank Optech for its help with fiber alignment and connections. Finally, we thank the personnel of the Animal Core Facility of the CRCHUM for providing the animal care and anesthesia and the CRCHUM Imagery Core Facility for help and expertise in imagery procedures.

CHAPITRE 5 ARTICLE 2: DATA CONSISTENCY AND CLASSIFICATION

MODEL TRANSFERABILITY ACROSS BIOMEDICAL RAMAN

SPECTROSCOPY SYSTEMS

**Fabien Picot, François Daoust, Guillaume Sheehy, Frédéric Dallaire, Layal Chaikho,
Théophile Bégin, Samuel Kadoury & Frédéric Leblond**

**Publié dans
TRANSLATIONAL BIOPHOTONICS
20 septembre 2020**

5.1 Abstract

Surgical guidance applications using Raman spectroscopy are being developed at a rapid pace in oncology to ensure safe and complete tumour resection during surgery. Clinical translation of these approaches relies on the acquisition of large spectral and histopathology datasets to train classification models. Data calibration must ensure compatibility across Raman systems and predictive model transferability to allow multi-centric studies to be conducted. This paper addresses issues relating with Raman measurement standardization by first comparing Raman spectral measurements made on an optical phantom and acquired with nine distinct point probe systems and one wide-field imaging instrument. Data standardization method led to normalized root-mean-square deviations between instruments of 2%. A classification model discriminating between white and gray matter was trained with one point probe system. When used to classify independent datasets acquired with the other systems, model predictions led to >95% accuracy, preliminarily demonstrating model transferability across different biomedical Raman spectroscopy instruments.

5.2 Introduction

Raman spectroscopy (RS) is an optical technique which can assess a sample's molecular content by probing its vibrational states. Over the last decades, it has been used in the medical field, in particular towards the development of imaging systems to detect pathologies [31], [97], [173]. The technique was used to guide tumor resection where the objective was to use the vibrational

spectroscopy information in combination with machine learning technology to maximize the volume of resected malignant tissue while preserving healthy tissue. Raman spectroscopy also showed promises in other clinical applications such as guided biopsy procedures in prostate surgery and neurosurgery [109], [174]. In 2011, Vargis et al. presented a Raman probe used in an *ex vivo* human study [106] to discriminate between normal, benign and malignant areas of the cervix, leading the way towards *in vivo* diagnosis. These results were followed in 2014 by another group, Shaikh et al., which was able to diagnose *in vivo* cervix cancer tissue with an accuracy superior to 95% [111]. Additional *in vivo* human diagnostic applications using RS can be found for multiple pathologies and especially multiple cancer types, such as gastro-intestinal cancers [112]–[114], [175]–[178] and malignant ulcers [179], lung cancers [115], [116], skin cancers [118]–[121], oral cancers [117], [180] and brain cancers [32], [67], [98], [99], [181], [182]. The number of patients in these studies varies greatly, ranging from 2 [116] to 848 [119], but in most cases does not exceed 100. A remarkable feat is that most RS studies consistently reported classification accuracies superior to 80%, while the lowest sensitivity and specificity reported were 75% [114] and 65% [115]. Most of these results were obtained by training a classification algorithm, usually combined with a leave-one-patient-out cross validation (LOPOCV). Principal component analysis combined with linear discriminant analysis (PCA-LDA) and partial least-square analysis combined with discriminant analysis (PLS-DA) stand as the most common algorithms used.

An emergent method to improve Raman imaging systems is to take advantage of a complementary signature to the fingerprint (FP) domain, i.e. the high wavenumber (HWN) range between 2500 and 3400 cm⁻¹. This was achieved in 2016 for oral [67][30] and colon [69][31] cancers and in a swine brain model in 2018 demonstrating its feasibility for human brain surgery [100]. Innovative clinical applications of RS, with *in vivo* human surgery potential, are still in development. It is partially done by conducting new animal experiments [183] and by designing new hardware systems, including Raman wide-field imaging systems [184], [185] as well as fused navigation platforms with Raman probe [174]. Overall, RS has demonstrated its great potential as an assisting diagnosis tool in the clinical environment. However, there are still relatively few large scale trials in the literature which not only limit the performance of the statistical models built but also mitigate their transferability to new trials.

To ensure high accuracy surgical guidance for a real-time human *in situ* application, the clinical translation relies on the quality and quantity of spectral and histopathological datasets from

a large number of patients. Due to the rapid pace of the RS development in oncology, multi-centric studies stand out as the best way to build these large-scale datasets. As a result, data calibration must ensure compatibility across Raman imaging systems. To answer this problem, we present in this paper a quantitative evaluation of the Raman data reproducibility when measurements are acquired and processed using multiple systems with different optical designs. This study's scope is limited to the compatibility of Raman biomedical spectroscopy systems regardless of the particularities of their clinical application. Hence the assessment is focusing on the inter-system deviation when comparing Raman spectra on a reference nylon phantom and on the diagnosis error of a classification model trained with one system and then exported and tested on multiple other systems.

5.3 Methods

5.3.1 Imaging systems and acquisition protocol

5.3.1.1 Point probe systems

Single-point interrogation in this study was performed using the fiber optics probe system developed by our group for neurosurgical applications [32]. Briefly, the hand-held probe (Emvision, LLC) was connected to a 785 nm laser source (Innovative Photonics Solution, USA) and a spectrometer (Emvision, LLC) with a resolution of $\approx 2 \text{ cm}^{-1}$. The probe had an outer diameter of 2.1 mm and was designed for tissue interrogation in reflectance. It integrated a central 272 μm (diameter) core excitation fiber surrounded by seven 300 μm core detection fibers. To minimize the Raman signature of the silica in the fibers, a short-pass filter and a notch filter were disposed in front of the illumination fiber and the detection fibers, respectively. Furthermore, a two-component lens was placed at the probe tip to ensure overlap between the excitation and detection areas, and a 3-meter long fiber bundle connected the probe to the laser and the spectrometer. Three probes, three spectrometers and one laser source were combined to assemble a total of nine distinct systems, labeled #1 to #9 (Fig. 5.1). The optical design and fabrication process were the same for all probe systems but the spectrometers differed in their slit width: 100 μm for systems #1 to #6 and 75 μm for systems #7 to #9.

All systems were controlled by a computer and the acquisition parameters were pre-set using a custom Matlab (Mathworks, USA) software. The laser power, P, and the number of repeat measurements at each point, n, were set at 50 mW and 20, respectively. The exposure time per spectrum, T, was computed and adjusted automatically to ensure a raw detected light intensity (photon count) >85% of the charged-coupled device (CCD) camera dynamic range, while avoiding saturation. The following measurements were made for normalization purposes: a dark count measurement with the laser off, an acetaminophen (DiN 00789801, Trianon inc, Canada) measurement for x-axis calibration, and a measurement on a relative intensity RS standard for excitation at 785 nm (NIST2241, NIST, USA).

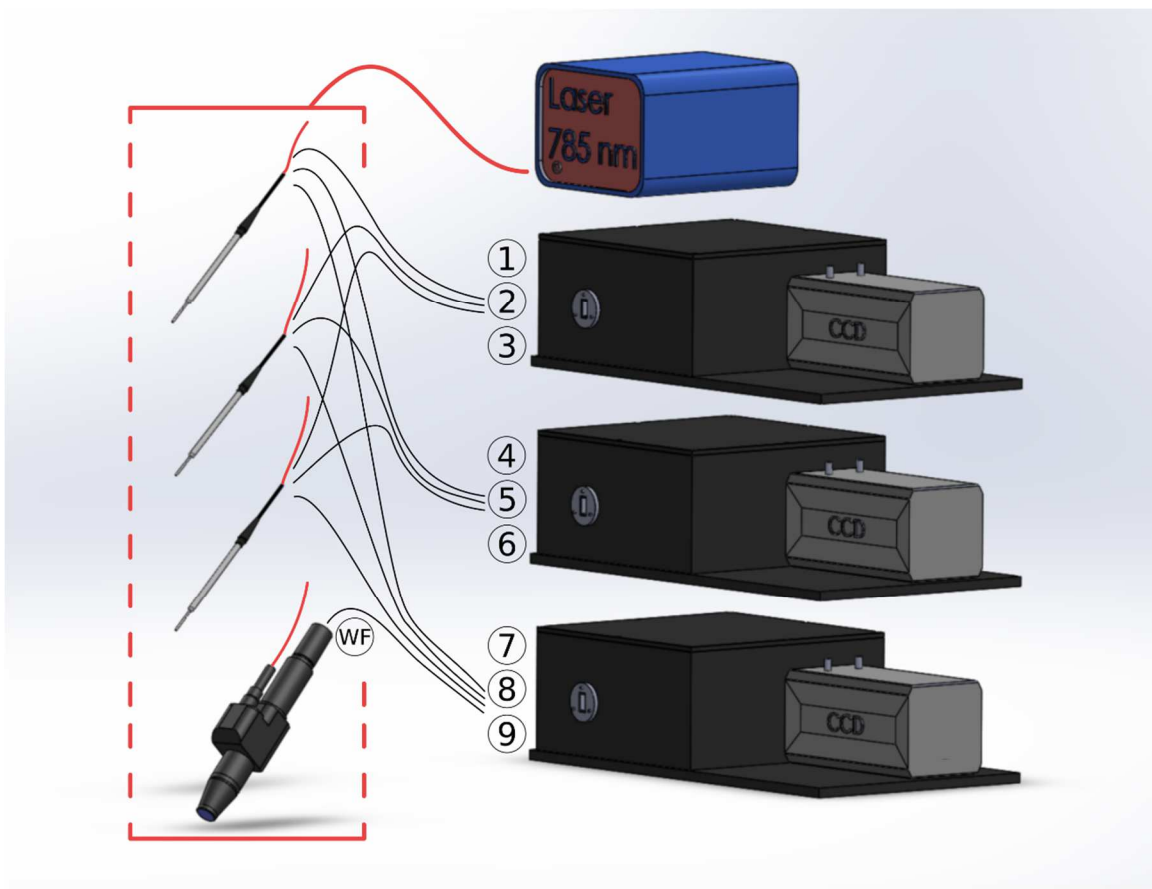


Figure 5.1 Three hand-held probes, one portable wide-field imaging instrument (labeled WF), three spectrometers and one 785 nm laser source were combined to build a total of 10 different Raman spectroscopy systems.

5.3.1.2 Wide-field Raman imaging system

The wide-field RS system used in this study was a modified version of a custom line-scanning instrument developed by our group [185]. The improvements made in the new system included the addition of a bright field reflectance channel and a series of optical components in the light path to the spectrometer. The new optics effectively decreased image size at the spectrometer slit and increased the signal-to-noise ratio (SNR). Briefly, the system consisted of a portable imaging instrument with a working distance of 40 mm, a FOV of $4 \times 4 \text{ mm}^2$ and a dichroic beam-splitter (LP02-785RE-25, Semrock, USA) combining the excitation and collection optical paths. Raman excitation was achieved using a 785 nm laser (Innovative Photonics Solution, USA) with an average laser intensity of 6.0 W/cm^2 at the sample along a single line scanned over the sample. Light detection was done through a series of collection optics, including a notch filter to eliminate elastic scattering from the excitation source, and a 91 cm long coherent imaging bundle with a $4 \times 4 \text{ mm}^2$ light sensitive area (IG-154, Schott, USA). The imaging bundle conveyed images through a flexible conduit of fiber optics to the collection branch of the system. The collection branch employed a series of optics and a scanning dichroic mirror to separate Raman scattering (810 to 922 nm) from the bright field signal (400 to 700 nm). Spectroscopic images were acquired through line scanning across the $75 \mu\text{m}$ slit of the spectrometer (HT model, EmVision LLC, USA) and the spectral content of each line was collected using a -60°C cooled CCD camera (Newton 920, Oxford Instruments, USA). A bright field reflectance image was collected with a high-sensitivity CMOS camera (DCC1240C, Thorlabs, USA) upon sample excitation with an exterior white light source (LED lamp).

Each component of the system was controlled via a custom software developed using LabVIEW (LabVIEW 2017, National Instruments, USA). Control and synchronization of the main system components (laser, galvanometer, cameras) was achieved using a digital acquisition device (150099A-04L, Texas Instruments, USA). Exposure time was kept at 4 s per line and laser intensity was set at its maximum value for each measurement. A total of 3 hyperspectral images were acquired and averaged for measurements on tissue phantoms while a total of 5 images were acquired and averaged for measurements on *ex vivo* tissue samples. Raman images were reconstructed by scanning 20 lines across a 16 mm^2 FOV. Pixels of the CCD camera were binned over 6 pixels along the spatial direction and 3 pixels along the spectral axis using the camera software (Solis S, Oxford Instruments, USA). This led to an instrument spatial resolution of 250

μm and a spectral resolution of 6 cm^{-1} . Room lights and the system's white light source were turned off during all spectroscopic measurements. White light images were acquired before every Raman image acquisition and the spectral data was processed in the same manner as the point probe systems. Table 5.1 summarizes the main imaging specifications distinguishing the imaging system from the point probe systems. The sampling depth for the Raman systems is estimated for both types of system to $\sim 500 \mu\text{m}$ based on [186].

5.3.2 Tissue phantom experiment

Nylon is associated with a distinctive Raman signature in the $400 - 1800 \text{ cm}^{-1}$ region [187]. A pure nylon disk (diameter = 5 cm, thickness = 1 cm) was cut and used as an optical phantom to evaluate signal variability between all 10 Raman systems. For the point probe systems, three measurements were made at three different locations on the phantom with the instrument placed in contact with the surface. The wide-field system was used to acquire a Raman image of the phantom and a nylon spectrum computed by averaging over three randomly selected pixels. The intra-system and inter-system deviations were computed as outlined in Section 2.5.

5.3.3 *Ex vivo* experiment

Six cynomolgus monkey (*Macaca fascicularis*) brains were used for *ex vivo* tissue experiments. The brains were cut into 52 slices (thickness = 1 mm), with each slice presenting visually distinguishable white matter and gray matter structural features. Sample preparation and storage were done at the CERVO Brain Research Centre. Immediately after animal death, the brains were collected and fixed by immersion, at 4°C , in 4% paraformaldehyde for 24 h. The organs were then sliced using a vibratome and preserved in phosphate buffered saline (PBS). This procedure was approved by the animal protection committee of Université Laval, in accordance to the Canadian Council on Animal Care's Guide and Use of Experimental Animals. All animals included in this study served in other experiments prior to our study.

The brain samples were used in an experiment evaluating classifier transferability between different RS systems based on a binary classification model (white matter vs. gray matter). To

minimize background contributions from non tissue specific Raman signals, slices were imaged on low Raman activity aluminum slides. System #1 was used to build the classification model using a 400 point-measurement dataset. Measurements were distributed equally between white matter and gray matter across the 52 slices. Point probe systems #2 to #9 and the wide-field imaging system were then used to acquire a testing dataset to evaluate the classification performance of the model. In total, 100 point measurements were acquired with the remaining point probe systems (#2 to #9), for a total of 800 points ensuring equal distribution between white matter and gray matter. All point measurements were acquired using a 1D linear stage to hold the probe and manually modify its position. Every point measurement required ~30s (~1.5s per spectrum for a total of 20 spectra per point measurement). Overall, the duration of the experiment was approximately 20 hours.

Tableau 5.1 Parameter differences between Raman wide-field system and point probe systems.

Parameters	Point probe systems	Imaging system
Sampling area	Ø500 µm	104x250 µm ² per pixel
Laser power	25.5 W/cm ²	6.0 W/cm ²
Spectral resolution	2 cm ⁻¹	6 cm ⁻¹
Integration time T per spectrum	~1 s per point	4s per line

Finally, one brain slice was randomly selected (amongst the 52 that were available) and imaged using the wide-field system. The resulting Raman spectroscopy image was spatially registered with a white light reflectance image to ensure each pixel could be assigned a tissue class (white matter or gray matter) in preparation for classification model testing.

5.3.4 Spectral data processing and statistical analysis

The raw spectroscopic data was first averaged over the number of spectra (n) acquired for each point. A cosmic ray removal algorithm was applied and the dark count signal subtracted [188]. The

signal was subsequently normalized with the NIST standard measurement and an x-axis calibration performed using the acetaminophen measurement. The background was finally removed using a rolling ball algorithm [189]. In addition, a quality factor $QF(n)$, was computed which consists in summing the Raman signal-to-noise ratio SNR_R over N spectral bands:

$$SNR_R \approx \sqrt{n T P} \sum_{j=1}^N \frac{r_j}{\sqrt{r_j + a_j}} \quad (1)$$

where r_j and a_j are the Raman signal and the background signal (mostly instrument response and fluorescence from the sample) within spectral band j , respectively [188]. Due to its ubiquitous presence in biological tissues [32], [68], [105], [122], the Raman peak at 1441 cm^{-1} was used as the unique band for the quality factor measurement. The final Raman spectrum R was then obtained by applying the standard normal variate (SNV) method. The Raman spectrum for each measurement point was then reduced to a list of K interpretable molecular features $\{\bar{R}\}_{l=1..K}$, around known tissue Raman peaks. Each feature was computed by integrating over a number of bands extending over 10 cm^{-1} around each peak.

Tableau 5.2 Raman band with molecular assignment, based on the literature, found in the current study on the monkey brain classification model [123], [190]–[192].

Raman band (cm^{-1})	Associated bond	Assigned molecules	Molecular family	[Ref]
700	Vibrational mode of sterol ring	Cholesterol	Lipids	[189]
1001	Symmetric ring breathing C-C stretching	Phenylalanine collagen heme carotenoid	Proteins	[122]
1064	C-O stretch C-O-C symmetric stretch C-C stretch	Proline phospholipid side chains cholesterol	Proteins lipids	[122]
1086	C-C stretch PO ₂ -symmetric stretch C=O vibration	Phospholipids nucleic acids	Lipids DNA	[122]
1129	C-C stretching	Skeletal of acyl backbone in lipid	Lipids	[190]
1262	CH ₂ in plane deformation	Glycerophospholipid	Lipids	[190] [191]
1298	CH ₂ twist and wag amide III	Phospholipids palmitic acid cholesterol collagen	Lipids proteins	[46]
1441	CH ₂ /CH ₃ deformation	Lipid side chains amino acids cholesterol collagen	Lipids proteins	[122]
1580	C=C bending mode of phenylalanine	Phenylalanine	Proteins	[190]
1659	Amide I C=C stretching	Nucleic acids collagen unsaturated fatty acids	DNA proteins lipids	[122]

The features used to produce the classification model were limited to $K = 4$ bands and were associated with common tissue molecular bonds: 1298, 1441, 1580 and 1659 cm^{-1} (Table 5.2). The bands around 1298, 1441 and 1659 cm^{-1} are associated with both lipids and proteins, but the 1659 cm^{-1} band can also be associated with nucleic acid content. The band around 1580 cm^{-1} is typically associated only with protein content, typically phenylalanine.

The next step consisted in producing classification models based on supervised training and testing on independent data. In this study, a two-class model was produced to discriminate between white matter and gray matter using the monkey brain samples by applying the following machine learning workflow. The classification algorithm was based on a support vector machine (SVM) [193] from $K = 4$ features resulting in a three-dimensional decision boundary; a similar modeling technique was used in [96]. Classification between white matter and gray matter was achieved through an optimization process using the geometrical distance of all measurement points from the decision boundary. Specifically, training was performed by minimizing a loss function which depends on SVM hyperparameters, namely: a regularization parameter, the kernel function, and the kernel coefficient. The dataset acquired with system #1 was divided into a training set (75% of all data points) and a testing set (25% of all data points). A 10-fold cross-validation procedure was then conducted using the training set to find the optimal hyperparameters based on a grid search method. The resulting hyperparameters obtained were 0.22 for the regularization parameter, 0.25 for the kernel coefficient and the kernel function was set to ‘linear’. The resulting model was then applied on an independent testing set composed of data from probes #2 to #9 and the wide-field system. The model performance was reported in terms of classification accuracy, sensitivity and specificity based on a receiver-operating-characteristic (ROC) curve analysis. All data processing was performed using the Matlab (Mathworks, USA) machine learning library.

5.3.5 Quantification of the intra-system and inter-system variability

Inter-system variability was evaluated by comparing measurements made on a nylon optical phantom with the point probe systems and the imaging system. Three co-located measurements were averaged for the point probe systems, while for the wide-field three randomly selected pixels across the image were averaged. These average values were used to compare system #1 to all the others point probe systems, and to compare system #1 to the wide-field system. The Raman

spectrum for each measurement was reduced to a list of $L = 14$ features $\{\bar{R}\}_{l=1..L}$, associated with characteristic nylon Raman bands (491.2, 616.7, 708.0, 788.7, 861.3, 953.8, 1062, 1131, 1234, 1298, 1384, 1443, 1477, 1634) cm^{-1}).

To compare system #1 to all the others point probe systems we calculated the residuals between the features $\{\bar{R}\}_{l=1..L}$ of system #1 and of systems #2 to #9. We then calculated the RMSD by taking the square-root of the residuals averaged over the systems. Finally, the RMSD was normalized by the statistical extent, $(\max_l \{\bar{R}\}_{l=1..L} - \min_l \{\bar{R}\}_{l=1..L})$ of system #1, as shown in the following equation:

$$NRMSD = \frac{RMSD}{\max_l \{\bar{R}\}_{l=1..L} - \min_l \{\bar{R}\}_{l=1..L}} \quad (2)$$

where $\max_l \{\bar{R}\}_{l=1..L}$ and $\min_l \{\bar{R}\}_{l=1..L}$ are the maximum and minimum of $\{\bar{R}\}_{l=1..L}$ over $\{l\}_{l=1..L}$ respectively. Similarly, we used the three point-measurements taken on the nylon phantom to evaluate the intra-system variability with every system. We used the same equation to calculate the NRMSD but the residuals calculated were between the three co-located measurements and their average. This complementary evaluation gives a reference for the inter-system variability to be compared with.

This procedure was repeated identically to compare system #1 to the wide-field system.

5.3.6 Quantitative evaluation of model transferability in monkey brain experiment

The classification model was first applied on the testing set from system #1 and the resulting sensitivity and specificity reported. These values were used as a comparison basis for the classifier's performance when applied on data acquired with the testing probe systems (#2 to #9). For each testing system, the entirety of the acquired data was considered as the testing data and the resulting sensitivity and specificity were averaged over 100 iterations of the machine learning workflow described in Section 2.4. These values were then directly compared with the base reference classifier's performance. Similarly, the classification model was applied to all pixels within the Raman image acquired with the wide-field system. The performance of the model was

estimated based on class labels (white matter or gray matter) assigned from inspection of the white light reflectance image.

5.4 Results

5.4.1 Quantitative comparison between systems

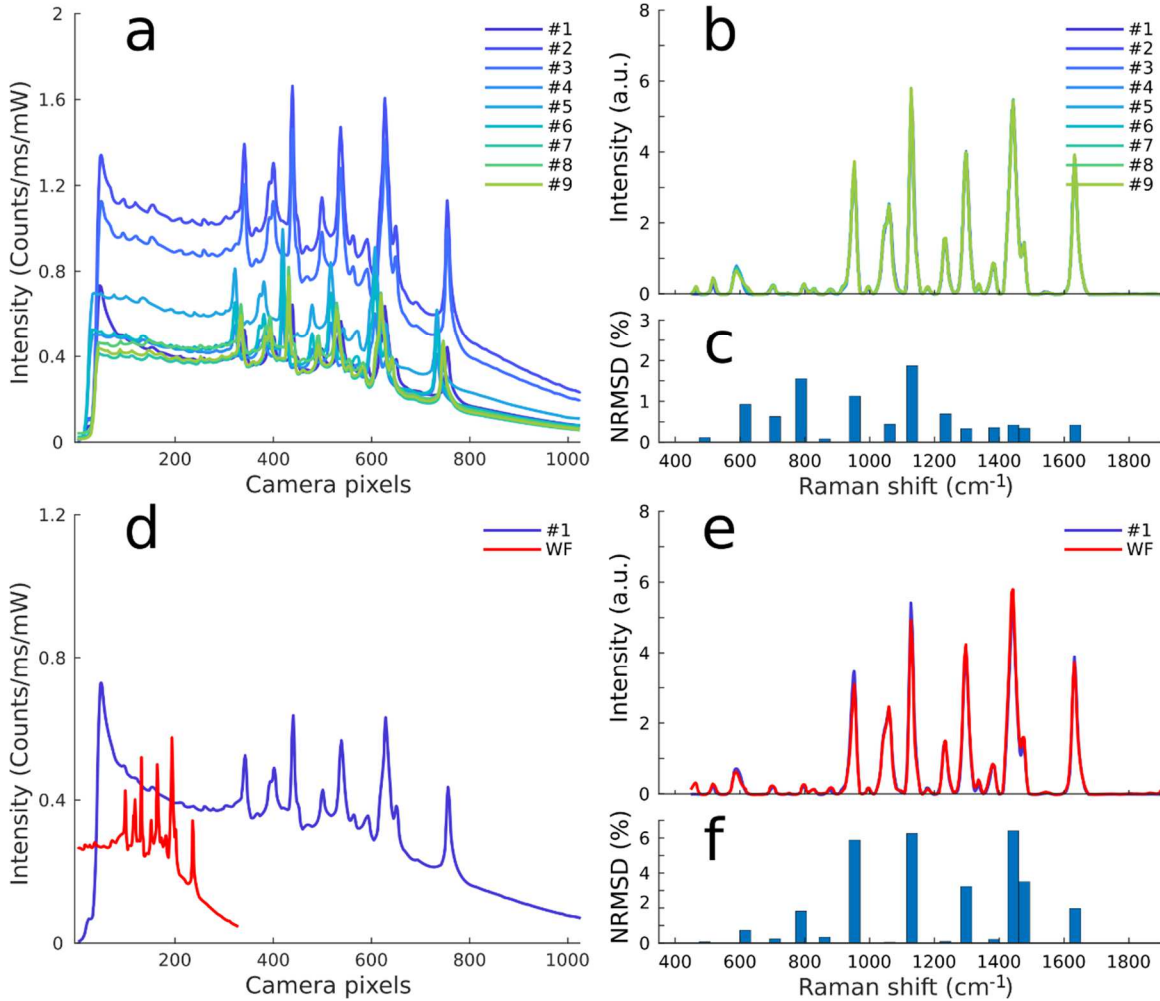


Figure 5.2 Quantitative comparison between point probe and wide field systems. Spectra comparison for point probe systems #1 to #9: A, raw spectra, B, processed Raman spectra, C, inter-system normalized root-mean-square deviation (NRMSD) for nylon features. Spectra comparison between point-probe system #1 and the wide-field system: D, raw spectra, E, processed Raman spectra, F, inter-system NRMSD for extracted features.

The inter-system variability was evaluated for all prominent Raman nylon peaks [37]: {491.2, 616.7, 708.0, 788.7, 861.3, 953.8, 1062, 1131, 1234, 1298, 1384, 1443, 1477, 1634} cm^{-1} . Fig. 5.2 illustrates the superposition of the nylon Raman measurements. Fig. 5.2a, 5.2b and 5.2c show this superposition when the 9 point probe systems are compared with one another, while Fig. 5.2d, 5.2e and 5.2f show the comparison between the point probe system #1 and the imaging system. The NMRSD between the 9 point probe Raman spectra is consistently inferior to 2% (Fig. 5.2c). Similarly, Fig. 5.2e shows how the Raman spectrum acquired using a point probe system compares to one acquired with the imaging system. The NMRSD between the two systems is overall inferior to 6% with only the peaks at 953.8, 1131 and 1443 cm^{-1} being over 4%. This deviation is to be compared with the point probes intra-system deviation, reaching a maximum of 5%.

5.4.2 Quantitative evaluation of model transferability in *ex vivo* experiment

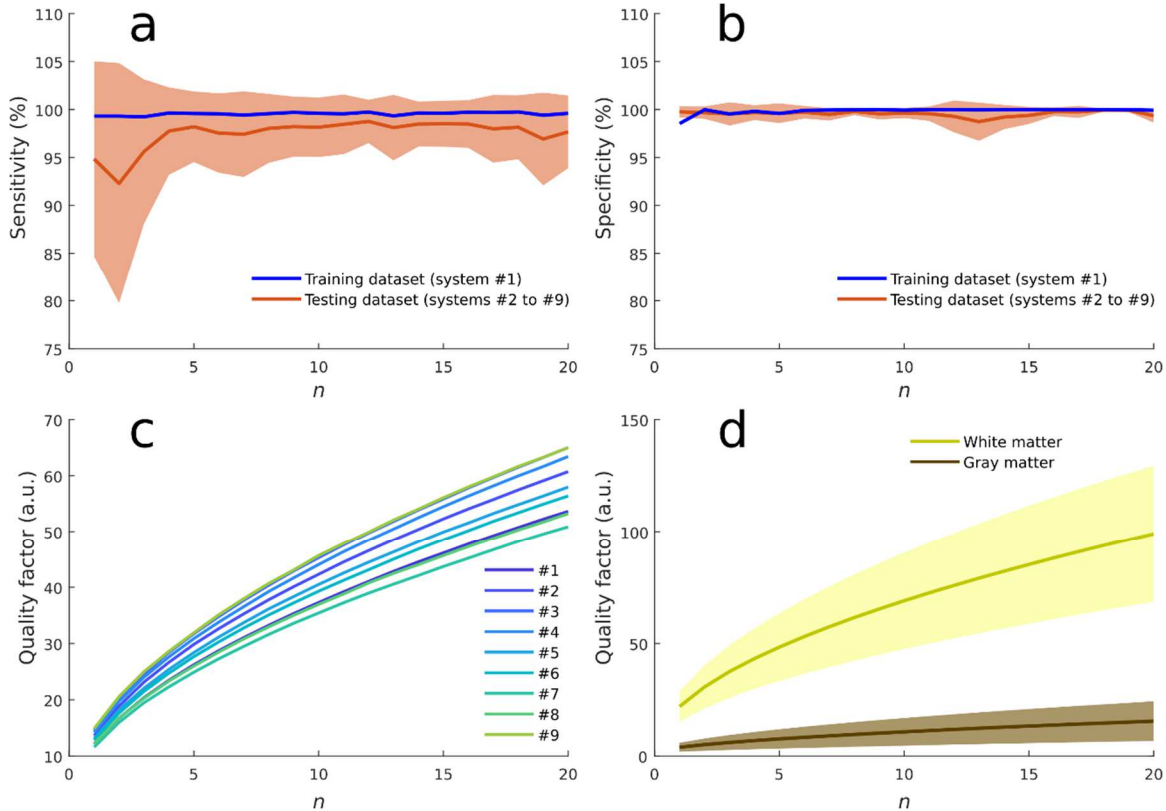


Figure 5.3 Classification model compatibility between the point probe systems and the wide-field imaging system. Average sensitivity, A, and specificity, B, of the classification model built with system #1 and tested on data acquired systems #2 to #9. The average and SD were calculated over 100 iterations of the machine learning workflow. C, Quality factor QF(n) depending on number of spectra per acquisition for systems #1 to #9. D, Quality factor QF(n) depending on number of spectra per acquisition for the two classes white/Gray matter. The average and SD were calculated over data measurements acquired per system, C, and per class, D.

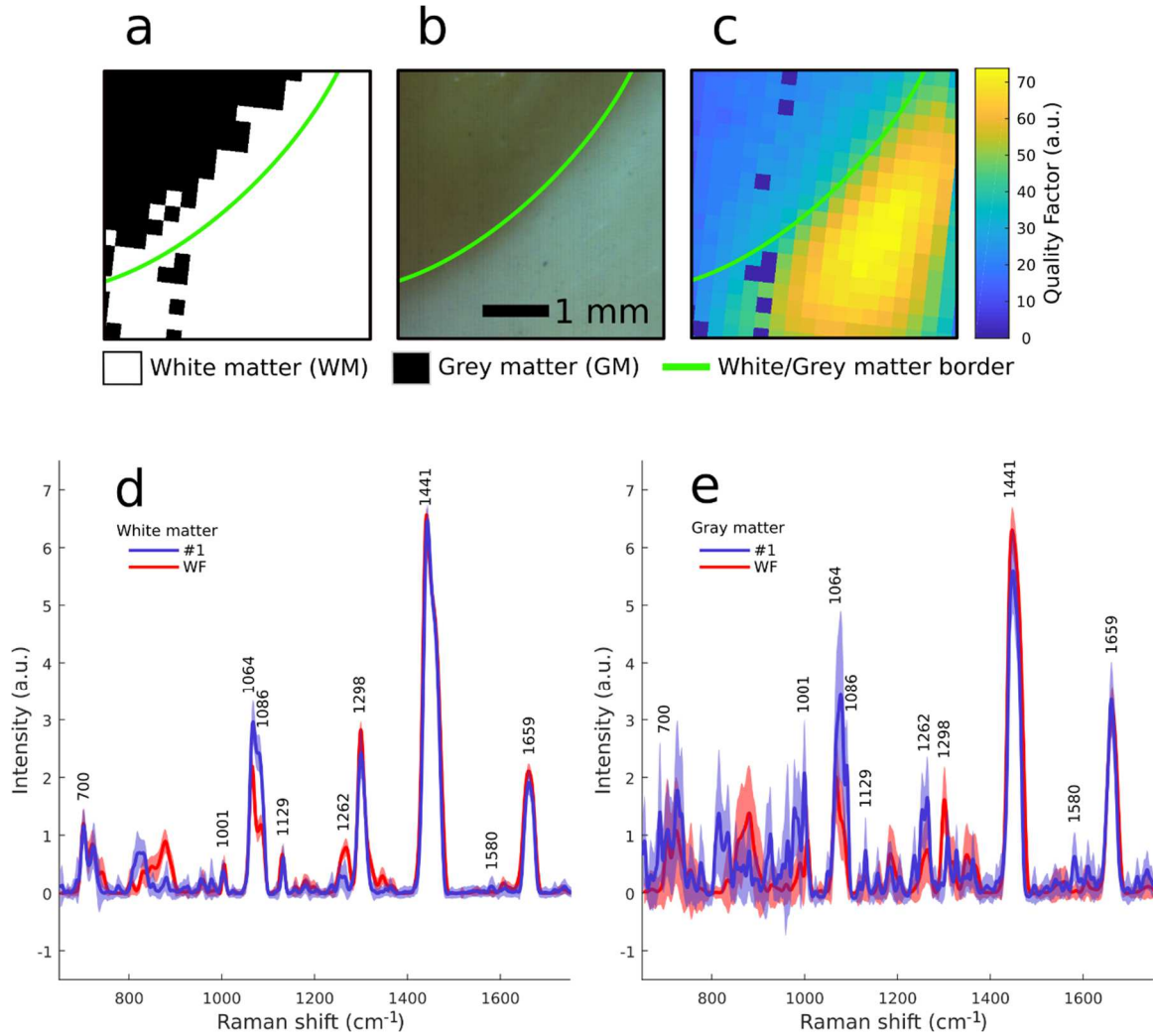


Figure 5.4 *Ex vivo* classification experimental results. A, Raman map of white matter (white pixels) and gray matter (black pixels) acquired with the wide-field system (#WF) and classified with the model built using the training system #1. B, White light reflectance image of the monkey brain acquired with the wide-field system (#WF). C, Quality factor map. D, Average and SD white matter spectra for system #1 and the wide-field system. E, Average and deviation gray matter spectra for system #1 and the wide-field system. The average and SD were calculated over data measurements acquired for the white matter, D, and for gray matter, E.

The *ex vivo* experiment illustrate classification model performances on multiple systems is presented in Fig. 5.3. Fig. 5.3a and 5.3b show the sensitivity and specificity of the classifier when applied on the testing sets acquired with both point probe system #1 (training system) and point

probe systems #2 to #9 (testing systems). Fig. 5.3c shows that the average quality factor, which is a function of n , varies from approximately 5 to a maximum comprised between 45 and 65 for all systems #1 to #9. As a result, which system is used only has a weak impact on the data quality factor. In contrast, the quality factor is highly dependent on the interrogated tissue type. As shown in Fig. 5.3d, the quality factor averaged on all gray matter sample reaches only a maximum of 15 compared to 100 for white matter. When tested on the testing set acquired with the training system, the classification model has a sensitivity of 99%, regardless of n . Its average sensitivity on data from the testing systems increases from 95% to 98% when n increases from 1 to 5 and is constant otherwise (Fig. 5.3a), meaning the optimum number of measurement per point for the brain classifier is $n = 5$ even though the quality factor increases for greater n values. Furthermore, the specificity for the training data is constant at 100% and is on average superior to 99% for the testing data with a deviation smaller than 5% (Fig. 5.3b). As a result, when exported from the training system to the testing systems, the model accuracy drops by less than 5% and remains >95%.

The classification model trained using system #1 successfully classified white matter vs. gray matter in the Raman image acquired using system #10, as shown in Fig. 5.4a. Fig. 5.4b displays the white light reflectance image used as a gold standard to identify the tissue classes and Fig. 5.4c shows the quality factor for every pixel, with an average of 20 and 60 for gray and white matter pixels, respectively. Nine pixels presented a factor of 0 because of a hardware fault during the acquisition. These pixels were systematically classified as gray matter pixels in the Raman map displayed in Fig. 5.4a, leading to 6 of them, located in the white matter area, to be misclassified. Aside from these misclassified pixels due to a hardware fault, a 500 μm band of gray matter is misclassified as white matter consistently along the border between tissue type. Otherwise, the rest of the image is classified accurately, demonstrating the transferability of the classification model, built with the training system, toward the wide-field system.

Finally, Fig. 5.4d and Fig. 5.4e show the average spectra measured on white and gray matter using the point probe and the wide-field imaging systems. The main difference in molecular composition of white and gray matter is a higher myelin content in white matter [194], resulting in a higher lipid concentration. This explains why white matter overall shares the same Raman peaks as gray matter (Table 5.2). However, the higher signal-to-noise ratio in white matter is partly associated to the strong Raman cross-section of lipids, as evidenced by the higher white matter quality factor in Fig. 5.3.

5.5 Discussion

Using the nylon phantom experiment, we can compare the intra- and inter-system deviations to assess the various systems measurement reproducibility. The intra-system deviation was typically below 3% for systems #1 to #9 and below 5% for the wide-field system, while these values were similar at 2% and 6% for the inter-system deviations of the multiple point probe systems and point probe vs wide-field systems, respectively. These deviations give, as a result, strong evidence for phantom measurement reproducibility regardless of the system used.

The *ex vivo* experiment on monkey brain demonstrates that a classification model can be exported from a training to a testing system with a low accuracy loss in the process, while the performance loss is higher in terms of sensitivity than specificity in the *ex vivo* point probe experiment. In this context, where sensitivity quantify the model ability to detect white matter, we expected that the highest quality factor associated with white matter measurements would be associated with a lower performance loss in sensitivity when transferring the model to other systems compared to the performance loss in specificity. However, due to the tissue identification error being overall negligible, quantitative correlation between the quality factor and the performance metrics may not be relevant for this association.

The Raman map shown in Fig. 5.4a returns a non-symmetrical margin error for diagnosis between white and gray matter, which is similar to results from another study where this system was used [185]. A plausible explanation to this phenomenon is the spatially offset Raman spectroscopy (SORS) effect caused by the wide-field illumination simultaneously to the line-scanning detection. To extract a depth-resolved Raman signature, this Raman imaging technique takes advantage of the spatial distance between the light collection occurring at the tissue surface and the point source Raman scattering event. In 2011, an in vitro study demonstrated Raman photons could be reliably detected over a distance of ≈ 2 mm through tissue [101]. This effect explains why the more prominent white matter signature, with higher lipids content, is detected over gray matter in a 500 μm margin band along the border between white and gray matter. As a result, the Raman map margin error displayed in Fig. 5.4a is probably not due to the classification model or to the data calibration and processing, but instead to the wide-field system detection design. A solution to this limitation was recently proposed and consists in including optical measurements, from the border between tissues, in the training set so that the resulting

classification model discriminates the biomolecular features from this region more accurately [195].

The Raman SNR and the corresponding quality factor extracted from the measurements appear to be critical for the development of high accuracy and generalizability of classification models. Optimizing these metrics mitigates Raman spectra deviations due to photonic noise and thus promotes increased ability of the Raman signature to separate between tissue classes. This is exemplified in our study by the difference of quality factor between white and gray matter. A significant improvement of the acquisition method for these systems would be an automated acquisition parameter control to ensure a minimum quality factor value set by the user, regardless of the interrogated tissue. This would allow for consistent quality Raman signal across the entire dataset.

This study presented preliminary evidence that standardized data calibration and processing enable the training of low complexity classification models, based on few spectral bands and their high transferability towards new data collected with different imaging systems. However, future work should focus on demonstrating the same results for more complex models, including more spectral bands. It should also investigate the classifier's transferability problematic in more challenging clinical problems such as *in vivo* human brain cancer detection for which spectral signature differences between tissues are more subtle [32], [98], [109].

5.6 Conclusion

Ten Raman spectroscopy systems, including nine based on hand-held probes and one portable imaging instrument, were used to measure Raman signals on a nylon phantom and on monkey brain samples to evaluate the inter-system signal deviation and its effect on classification problems. Low inter-system deviations were observed and, using our standardized data calibration method, we also demonstrated that a two-class classification model can be trained using a training point probe-based system and transferred to an imaging-based system without significant increase of tissue identification error. These results demonstrate the feasibility of combining measurements from multiple Raman imaging systems in a centralized databank, opening the possibility of future training of statistical models based on a new scale of human clinical dataset.

5.7 Acknowledgments

This work is supported by the Discovery Grant program from the Natural Sciences and Engineering Research Council of Canada (NSERC), the Collaborative Health Research Program (CIHR and NSERC), and the TransMedTech Institute. We would also like to thank Damon de Paoli, Daniel Côté and Martin Parent (CERVO brain research center, Université Laval) for providing the animal brains.

5.8 Conflict of interest

We do not declare any conflict of interest concerning this study.

5.9 Data availability statement

The data that support the findings of this study are available from the corresponding author upon reasonable request.

**CHAPITRE 6 ARTICLE 3: IMAGE-GUIDED RAMAN SPECTROSCOPY
NAVIGATION SYSTEM TO IMPROVE TRANSPERINEAL PROSTATE
CANCER DETECTION. PART 1: RAMAN SPECTROSCOPY FIBER-
OPTICS SYSTEM AND *IN SITU* TISSUE CHARACTERIZATION**

Fabien Picot, Rozbeh Shams, Frédéric Dallaire, Guillaume Sheehy, Trang Tran, David Grajales,
Mirela Birle, Dominique Trudel, Cynthia Ménard, Samuel Kadoury, Frédéric Leblond

Publié dans
JOURNAL OF BIOMEDICAL OPTICS
27 septembre 2022

6.1 Abstract

Significance: The diagnosis of prostate cancer (PCa) and focal treatment by brachytherapy are limited by the lack of precise intraoperative information to target tumors during biopsy collection and radiation seed placement. Novel image-guidance techniques could improve the safety and diagnostic yield of biopsy collection as well as increase the efficacy of radiotherapy.

Aim: To estimate the accuracy of PCa detection using *in situ* Raman spectroscopy (RS) in a pilot in-human clinical study and assess biochemical differences between *in vivo* and *ex vivo* measurements.

Approach: A new miniature RS fiber-optics system equipped with an electromagnetic (EM) tracker was guided by TRUS imaging, fused with pre-operative magnetic resonance imaging (MRI) to acquire 49 spectra *in situ* (*in vivo*) from 18 PCa patients. In addition, 179 spectra were acquired *ex vivo* in fresh prostate samples from 14 patients who underwent radical prostatectomy. Two machine-learning models were trained to discriminate cancer from normal prostate tissue from both *in situ* and *ex vivo* datasets.

Results: A support vector machine (SVM) model was trained on the *in situ* dataset and its performance was evaluated using leave-one-patient-out cross validation (LOPOCV) from 28 normal prostate measurements and 21 in-tumor measurements. The model performed at 86% sensitivity and 72% specificity. Similarly, an SVM model was trained with the *ex vivo* dataset from 152 normal prostate measurements and 27 tumor measurements showing reduced cancer detection

performance mostly attributable to spatial registration inaccuracies between probe measurements and histology assessment. A qualitative comparison between *in situ* and *ex vivo* measurements demonstrated a one-to-one correspondence and similar ratios between the main Raman bands (e.g., amide I-II bands, phenylalanine).

Conclusions: PCa detection can be achieved using RS and machine learning models for image-guidance applications by using *in situ* measurements during prostate biopsy procedures.

6.2 Introduction

In 2020, 1.4 million cases of prostate cancer (PCa) were diagnosed worldwide with an estimated 375,000 deaths [196]. In the United States, PCa is the most common and second deadliest cancer for men, accounting for 11% of total cancer deaths [7]. Trans-rectal ultrasound-guided (TRUS) biopsy procedure is the standard of care for diagnosis of PCa due to its real-time capabilities and convenience [197]–[199]. However, the genotypic and phenotypic heterogeneity of prostate tumors presents challenges in validating their position, type, extent and grade to establish the diagnosis and prognosis [200], [201]. As a result, a significant rate of false negatives is reported for prostate biopsy procedures, reaching up to 30% [17], [18].

To address this clinical problem, electromagnetic (EM) tracking has helped to enhance the guidance of brachytherapy procedures [19]–[21] and may have potential to guide prostate biopsy surgery. Furthermore, magnetic resonance imaging (MRI) navigation systems demonstrated superior sensitivity and equivalent or superior specificity to TRUS-guided biopsy [22], [23], including an 85% sensitivity for prostate tumors larger than 10 mm [24]. The limited access and higher costs of MRI for intraoperative and real-time surgical use [25], [26] has incentivized the use of MRI-TRUS fusion technology, which combines the high sensitivity of MRI and the high specificity of TRUS while removing the intraoperative use of MRI. By relying on pre-operative MRI images, MRI-TRUS fusion technology can further increase the accuracy of the biopsy procedure. However, due to the dynamic tissue deformation caused by the surgical instrument, the image registration between these modalities remains a challenge [27]–[29].

Raman spectroscopy (RS) is a technique that can assess the biomolecular content of a sample through its optical properties. RS collects information about the vibrational states, which

are specific to the molecules involved in the Raman scattering events. The molecular information infers differences in tissues, providing a real-time confirmation of tumor location during therapy. In the last decades, RS has been used for the *in vivo* diagnosis of several cancer types. Multiple research groups have successfully targeted skin cancers in open surgeries [118]–[120]. McGregor et al. used Raman probes for a minimally invasive diagnosis of peripheral and early lung cancers [115], [116]. The state of the art technology has also combined fingerprint (FP) and high wavenumber (HWN) spectral domains to further increase the sensitivity and specificity of Raman systems, notably on oral, colon and brain cancers [67], [69], [172]. Aubertin et al. conducted two *ex vivo* studies on human prostate, resulting in classification models that discriminated cancer from normal tissue with >85% sensitivity and specificity [68], [105]. Since 2019, similar performances have been reported in an *ex vivo* Raman microscopy study [96], while a Raman probe integrated to a robotic-assisted surgical system allowed the *in vivo* collection of extra-prostatic and prostatic preliminary spectra without classification [122]. To the best of our knowledge, there is no in-human study reporting the use of a Raman system for the purpose of PCa diagnosis.

We conducted a pilot clinical study to evaluate the feasibility and performance of a multimodal system, combining RS and MRI-TRUS guidance using EM tracking, for PCa diagnosis during surgery. For clarity and conciseness we divided this study in two parts. This manuscript is Part 1 and presents our combined *ex vivo* and first in-human *in situ* RS study on prostate tissues from a total of 32 patients. A RS system in which an EM tracker was integrated was used to perform MRI-TRUS procedures on 18 patients. The 49 *in situ* spectra acquired from these patients were used as a training dataset to build a support vector machine (SVM) classification model discriminating cancer from normal prostate tissue. Additionally, 179 *ex vivo* Raman measurements acquired from fresh prostate specimens of 14 patients who underwent radical prostatectomy (RP) were also used to further analyze the biomolecular content of prostate tissue and perform a qualitative comparison with the *in vivo* measurements. Part 2 of the study [202] focuses on machine learning applications demonstrating that combining biomolecular characteristics from RS with imaging features from preoperative multiparametric MRI improves PCa detection accuracy.

6.3 Methods

6.3.1 Raman system and calibration processing

Optical measurements were obtained using an RS fiber-optics probe (EmVision LLC, FL, USA) equipped with an EM tracker that was developed by our group for prostate biopsy applications (Figure 6.1) [174]. The probe integrates eleven optical fibers and the EM tracker can sense six degrees of freedom (6-DOF) (NDI Inc., Canada). The rigid part of the probe has a length of 20 cm and an outer diameter of 1.22 mm. The wire of the tracker is located 3.25 mm from the distal end of the probe next to the ten fiber-optics collection fibers (100 μm diameter core). Of these fibers, nine were intended to be used for Raman signal detection and one for fluorescence signal, and sensors encircled the length of the one Raman excitation fiber. However, no fluorescence measurements were made as part of this study. As shown in the magnified view of the probe tip in Figure 6.1, two different filters are positioned to cover both collection and excitation Raman fibers. A band-pass filter, centered at 709 nm with full-width-at-half maximum (FWHM) of 172 nm (Semrock, NY, USA), is placed at the end of the Raman excitation fiber to allow illumination at 671 nm and 785 nm for HWN and FP detection, respectively. A notch filter, centered at 785 nm with FWHM of 39 nm (Semrock, NY, USA), is placed at the end of Raman collection fibers to prevent silicon signature from interfering with the signal of interest when using an excitation of 785 nm. Finally, one collection fiber is left without any filter to allow fluorescence signal acquisition although it is not used in the clinical protocol and was included in the design only for a future fluorescence system integration. A nylon heat shrink tubing seals and protects the probe's tip. The probe itself is then connected to a dual-wavelength laser 671/785 nm (Innovative Photonics Solution, NJ, USA) and a high sensitivity spectrometer at wavelengths from 800 to 900 nm, with an average resolution of 1.8 cm^{-1} (EmVision LLC, FL, USA). Two slightly different versions of this probe were used for our study; both were identical except for one probe that had a two-component lens at the probe's tip to enhance signal collection and used of a 200 μm (instead of 100 μm) diameter core for the excitation fiber. The overall system was controlled by a Matlab (Mathworks, USA) customized software to set acquisitions parameters: laser power P, exposure time per spectrum T, and number of repeated measurements n at each point. Complementary calibration data was acquired prior to experiments for normalization purpose. This included a dark count acquisition with illumination off, acetaminophen measurements (DiN 00789801, Trianon

inc, Canada) for x-axis calibration, and measurements of a Raman standard (NIST2241, NIST, USA) for relative intensity calibration.

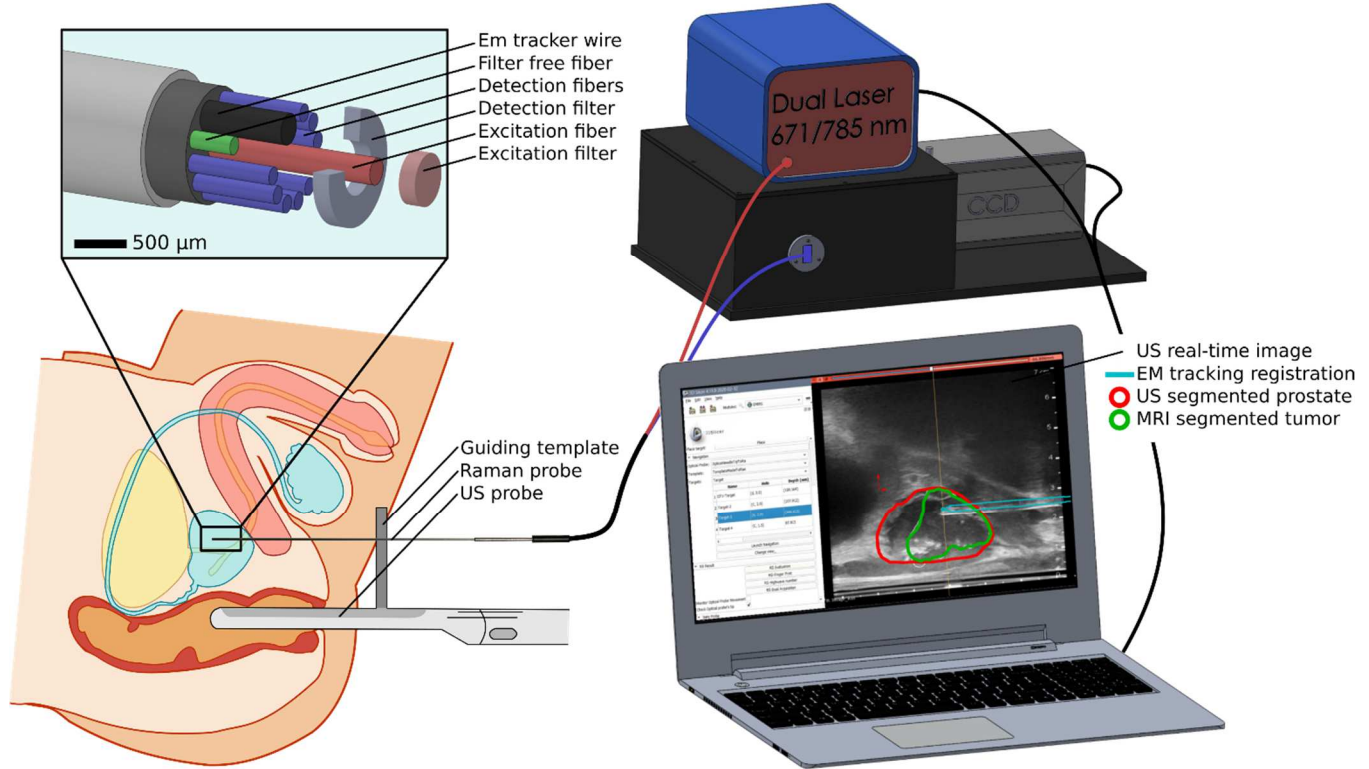


Figure 6.1 Schematic representation of the Raman probe obtaining measurements of the prostate through the guiding template, with a magnified view of the probe's tip. The probe is connected to the laser source and the spectrometer, which are controlled by a computer, and the optical system is combined with a TRUS system to perform the prostate biopsy procedure through the surgical guiding template. The computer displays the fused TRUS-MRI guiding image and the raw optical spectra after spectral acquisition for each site.

6.3.2 Navigation system

The navigation system used MRI-TRUS fusion guidance and is fully described in our previous study [174] as well as in the companion study of this paper [202]. Targets for the biopsy procedure were determined on pre-operative MRI identification of regions of interest: based on multiparametric MRI, performed without contrast agent, the physician segmented the tumor and

selected at least one biopsy site in the tumor and at least one biopsy site more than 10 mm away from the tumor. We used prototype interventional system (Invivo/UroNav, Philips Disease Management Solutions, Gainesville, USA) to perform the fusion between MRI images and 3D TRUS acquired with a BK3000 ultrasound and a BK Endocavity Biplane 8848 transducer (BK Medical, Denmark). The multiple subsystems, EM tracking, MRI-segmented images and US were connected and coordinated using a customized 3D Slicer [203] module allowing visualization of the registration. The navigation system was used during the prostate biopsy procedure to provide the surgeon with real-time anatomical guidance for instrument insertion, including the Raman probe, biopsy gun and guiding cannulas. Only TRUS-MRI fused structures, without the RS, were used for navigation to the targets. They were only used for tissue classification purposes in Part 2 of the study.

6.3.3 Patient selection

Informed consent was obtained from the 32 patients included in this study. Fourteen patients underwent prostate biopsy procedures revealing more than two PCa positive biopsy cores with a cancer involvement >10% for each core. Patients agreed to participate in the institutional PCa repository of the Centre hospitalier de l'Université de Montréal (CHUM Ethics Committees approval number 15.102) and underwent RP, leading to the exclusion of prostate specimens <35g. Samples from these 14 patients were used to build the *ex vivo* dataset combining RS and histopathological data. Similarly, 18 patients were recruited in the study to acquire *in situ* data to build the *in vivo* dataset. Informed consents were obtained as well as agreement to participate in the institutional PCa repository before the patient underwent prostate biopsy procedure (CHUM Ethics Committees approval number 18.295). Clinical data were added to include age and pre-operative prostate-specific antigen (PSA) of patients for both datasets. We also added the grade group (GG) from the whole prostate pathology result after RP and from the core needle biopsy procedure to the *ex vivo* and *in vivo* datasets, respectively. Finally, pathological stage (pT) was determined after RP procedures by a pathologist at the CHUM according to the TNM staging system, seventh edition [204]. The details of these histopathological analyses are shown in Table 6.1.

Tableau 6.1 Clinical and pathological characteristics of the patients at radical prostatectomy and at biopsy procedure.

Characteristics	<i>ex vivo</i>	<i>in vivo</i>
# patients (# measurements)	14 (179)	18 (49)
Median age	64 (62-67)	67 (65-70)
Median PSA ($\mu\text{g}/\mu\text{L}$)	5.56 (4.11-8.06)	5.84 (4.59-11.44)
# measurements (cancer/normal)	27/152	21/28
Prostate cancer grade # patients		
0	0	3
1	1	1
2	6	6
3	5	5
4	0	3
5	2	0
Pathological tumor stage # patients		
pT2 (organ-confined)	8 (20)	—
pT3a (extra-prostatic extension)	4 (5)	—
pT3b (seminal vesicle extension)	2 (2)	—

The recruitment of the 32 patients led to two independent datasets: *ex vivo* and *in vivo*. Each dataset was used to build a classification model to assess the potential of RS to discriminate cancer from normal tissue and allowed a qualitative assessment of the main spectral differences between *in vivo* and *ex vivo* measurements.

6.3.4 Specimen handling and *ex vivo* measurements

Immediately after RP, the entire organ was weighed, measured and marked with ink, following institutional standards [205]. The prostate was cut in transverse plane perpendicular to the urethra, in approximately ten slices with a thickness of 3-5 mm each. The slice with the highest probability of containing a large cancer area, according to the biopsy pathology report, was removed and held between two pieces of waxed cardboard and then placed in the guiding template, as shown in Figure 6.2a. Raman measurements were taken sequentially through the guiding holes. The laser power P was optimized and set at a maximum of 20-50 mW to prevent tissue or instrument damage. Number of repeat measurements per point n was fixed at 50 and the exposure time per spectra T ($0.1 < T < 2\text{s}$) was automatically adjusted and optimized to ensure a raw signal intensity between 85% and 100%

of the camera dynamic range. After the measurements were done, the slice was put in 10% formalin and underwent standard histopathological analysis based on microscopic hematoxylin, phloxine and saffron staining (HPS). In the time between its removal from the patient and its histopathological analysis, the prostate slice was prepared and measurements were acquired within a 2-hour limit to ensure preservation of the sample. This time constraint put a limit of an hour for the total optical acquisition time, allowing 5-20 point measurements per sample.

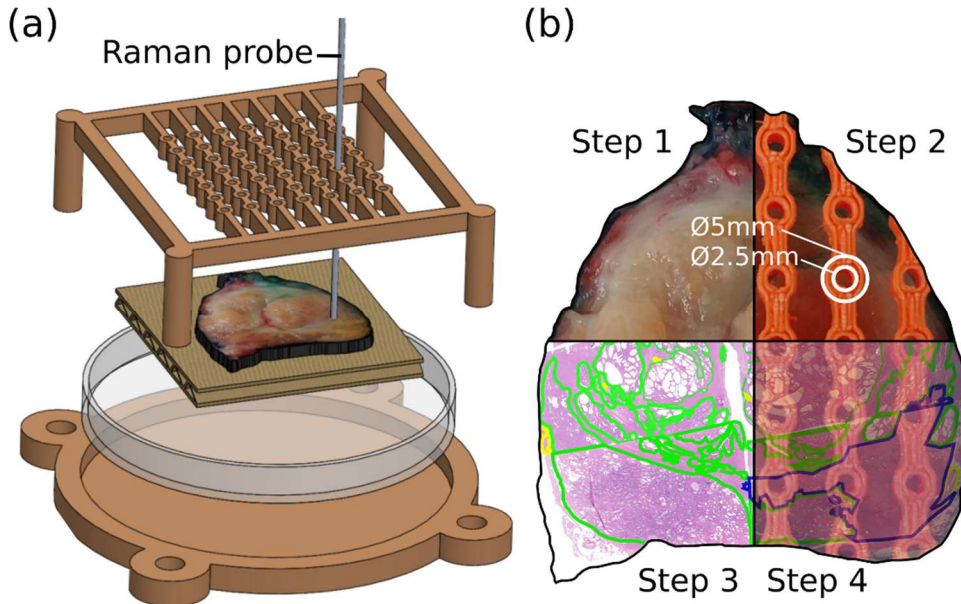


Figure 6.2 (a) Magnified view of the fresh prostate slice inside the guiding template for incremental Raman point measurements. (b) Four-step methodology for spatial registration of Raman measurements with labelled HPS tissue image reconstruction. Step 1 is a photograph of fresh prostate specimen; Step 2 is a photograph of the fresh prostate specimen through guiding template; Step 3 is HPS-labelled prostate image (cancer and normal tissue are labelled in blue and green, respectively); and Step 4 is the superimposed images of Step 2 and Step 3.

6.3.5 Prostate slice reconstruction and registration with optical measurements

The process of registration between Raman measurement locations and HPS prostate images that assessed tissue as cancer or normal involved four steps. The first and second steps consisted of macroscopic photographs of the prostate slice in actual image and through the guiding template,

respectively, as shown on Figure 6.2b. A contour was extracted from the image of stage 1 and served as a guiding boundary to reconstruct the HPS prostate image. Due to standard histopathological processing, the fresh prostate slice was segmented into 4-10 equal sections before staining. These sections were then imaged with an Aperio Digital Pathology Slide Scanner (Leica Biosystems, Nussloch, Germany) and were labelled by a pathologist to discriminate cancer area from normal tissue area. Stage 3 juxtaposed the labelled sections to build the complete HPS prostate image. For every section, multiple anatomical landmarks were used to ensure continuity between each other for accurate reconstruction. This included boundaries of cancerous nodules, ejaculatory ducts, prostatic urethra and benign prostate hypertrophic nodules. Finally, stage 4 superimposed the results of the macroscopic fresh prostate photograph through the template from stage 2 and the HPS reconstructed prostate image from stage 3. Figure 6.2b shows for stage 4, every possible location of the probe through guiding template registered with a normal/cancer diagnosis.

Reconstruction of prostate slices and registrations with optical measurements were done using Inkscape software (Inkscape's Contributors). Several factors could potentially limit the accuracy of the results, such as anisotropic tissue warping and uneven tissue level between adjacent sections. To mitigate the amount of classification error by our histopathological gold standard, we applied a spatial margin error. A measurement was labelled as normal if no cancer tissue was found in a 2.5 mm radius of the point localization. Similarly, a measurement was labelled as cancer and as cancer border if no normal tissue was found in a 2.5 mm and 1.25 mm radius, respectively, of the point localization. The choice to ensure a higher level of certainty for normal points than for cancer points was made because of the imbalance between these classes in the dataset, with only <15% of points labelled as cancer or cancer border.

6.3.6 Surgical workflow and *in vivo* measurements

Once patients are under anesthesia, the lead surgeon sets up the US system to acquire a full 3D image of the prostate and its surrounding tissue and then operates the imaging system in real-time 2D mode. The prostate is manually fully segmented in the 3D TRUS image and serves as a reference to register the imported 3D pre-operative MRI data including the tumor segmentations. Although this step can be managed through the 3D slicer module, it is done by the Invivo/Uronav system fusion methods for workflow efficiency. The EM generator field is positioned by

mechanical arm above the patient's abdomen for the entire procedure. Two to four targets are defined on the MRI-TRUS navigation system and visualized on the augmented 2D real-time TRUS image. They are used by the surgeon to guide the insertion of cannulas to each biopsy target. The optical probe is inserted through the guiding cannulas and, with the probe's tip making contact with the tissue, the Raman measurement is acquired ($P=50\text{mW}$, $n=50$ or 100 and T optimized as exactly described in section 2.4). The probe is then immediately removed and replaced by the prostate biopsy gun to ensure an exact spatial registration between the optical measurement and the sample's location. A horizontal cross-sectional sample is extracted and the process is repeated for every target defined by the navigation system. The samples undergo a post-operative histopathological analysis (HPS staining) to provide a normal vs. cancer label to build the *in vivo* dataset. The overall procedure lasts roughly 150 minutes, including 20-30 minutes to operate the multimodal guiding system and allowed 1 to 5 distinct measurements localization.

6.3.7 Data processing and machine learning workflow

The data processing steps preceding the production of machine learning models involve extracting the Raman signature of the sample from the background signal, mostly associated with intrinsic tissue fluorescence. Raw data was averaged over the number of spectra (n), and cosmic ray artefacts were removed using a median filter. The calibration data acquired prior to the experiment was then used to subtract the dark count signal, normalize with the NIST standard measurement, and provide every spectrum with the x-axis Raman shift in cm^{-1} . Finally, the background from autofluorescence signal was removed using a rolling ball algorithm, and the resulting Raman measurements were combined with labels (normal vs. cancer) to be used as a training set input for the statistical analysis.

Due to the small size of the datasets, in comparison with the 1024 available intensity bins for each spectrum, the first step of the machine learning workflow consisted of dimensional reduction to <10 features. This dimensional reduction was achieved using a leave-one-patient-out cross validation (LOPOCV) random forest (RF) algorithm [206], [207]. Each feature was assigned a statistical weight quantifying its ability to capture inter-class variations or “class purity”, allowing less important features to be dismissed. The remaining features were sorted according to their weight and a limited number of features associated with known prostatic molecular content was

retained for model training. This feature selection process was applied independently twice: once on the raw 1024 feature set, and once again on the (<20) fitted Raman peaks extracted from the processed measurements. This method ensured a selection of <10 features notably linked to prostatic molecular content while still maintaining high statistical relevance for class separation.

The classification model training was a support vector machine (SVM) with a linear kernel and a regularization parameter C. This hyperparameter, varying between 10⁻³ and 1, controlled the penalty for errors in the training process and prevented the model from overfitting since the number of observations used as support vectors remained <50% of the total observations. The SVM algorithm also considered the class imbalance (cancer vs. normal) for all datasets by setting a higher cost γ to misclassified cancer spectra from normal spectra. A fixed weight value of 1 was set for the normal class, while γ varied between 0.2 and 5 for the cancer class. A grid search method was used to optimize both hyperparameters C and γ , and a LOPOCV procedure was performed to assess the classification model performance. The resulting model demonstrated optimal performance to discriminate cancer from normal tissue and returned for each measurement a posterior probability $0 \leq p \leq 1$ to be classified as cancer. A receiver-operating-characteristic (ROC) curve was computed by comparing this posterior probability p with a parameter λ ($0 \leq \lambda \leq 1$). All observations associated by the classifier were assigned the label “cancer” when $p \geq \lambda$ or assigned the label “normal” if otherwise. Different values of the parameter λ corresponded to different points of the ROC curve. For all observations tested through cross validation, every point combines the comparison between the labels returned by the classifier and those returned by the histopathological gold standard to provide sensitivity and specificity values.

Results were reported for the optimized hyperparameters only, yielding the highest area-under-curve (AUC) value. The final optimized model, with reported accuracy, sensitivity and specificity, corresponds to the ROC curve point with the smallest distance to the upper left corner of the curve.

6.4 Results

6.4.1 Spectroscopic measurements

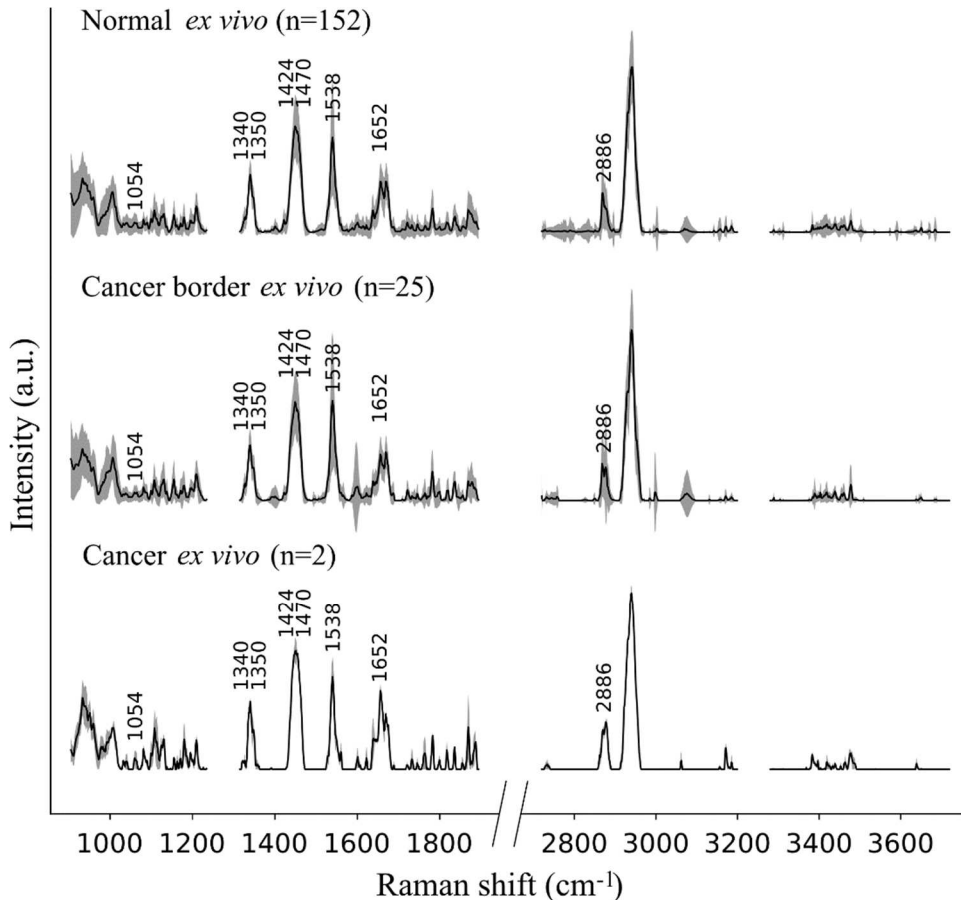


Figure 6.3 *Ex vivo* dataset: average and standard deviation of processed spectra for each category (normal, cancer border, cancer) with all peaks used by the classification models labeled with their Raman shift in cm⁻¹.

The processed histopathological images of the 14 *ex vivo* prostate samples resulted in 179 spectroscopic measurements with co-located histopathology analyses, including 152 measurements labeled as normal prostate, 2 labeled as pure cancer and 25 labelled as cancer border (mixture of normal prostate and cancer). A total of 20 additional measurements were located in normal tissue with cancer tissue within a <2.5mm radius and were removed from the *ex vivo*

dataset. Figure 6.3 shows the average and standard deviation for the Raman measurements of normal ($n=152$), cancer border ($n=25$) and cancer ($n=2$) for both FP (500-2000 cm^{-1}) and HWN (2500-3800 cm^{-1}) spectral domains. All three classes displayed similar high intensities for the phenylalanine peak at 1000 cm^{-1} , the collagen peaks at 1340 and 1440 cm^{-1} , the amides peaks at 1535 and 1650 cm^{-1} , and the lipids and protein peaks at 2880 and 2930 cm^{-1} , respectively. Qualitative assessment of the spectral bands did not allow direct discrimination between classes.

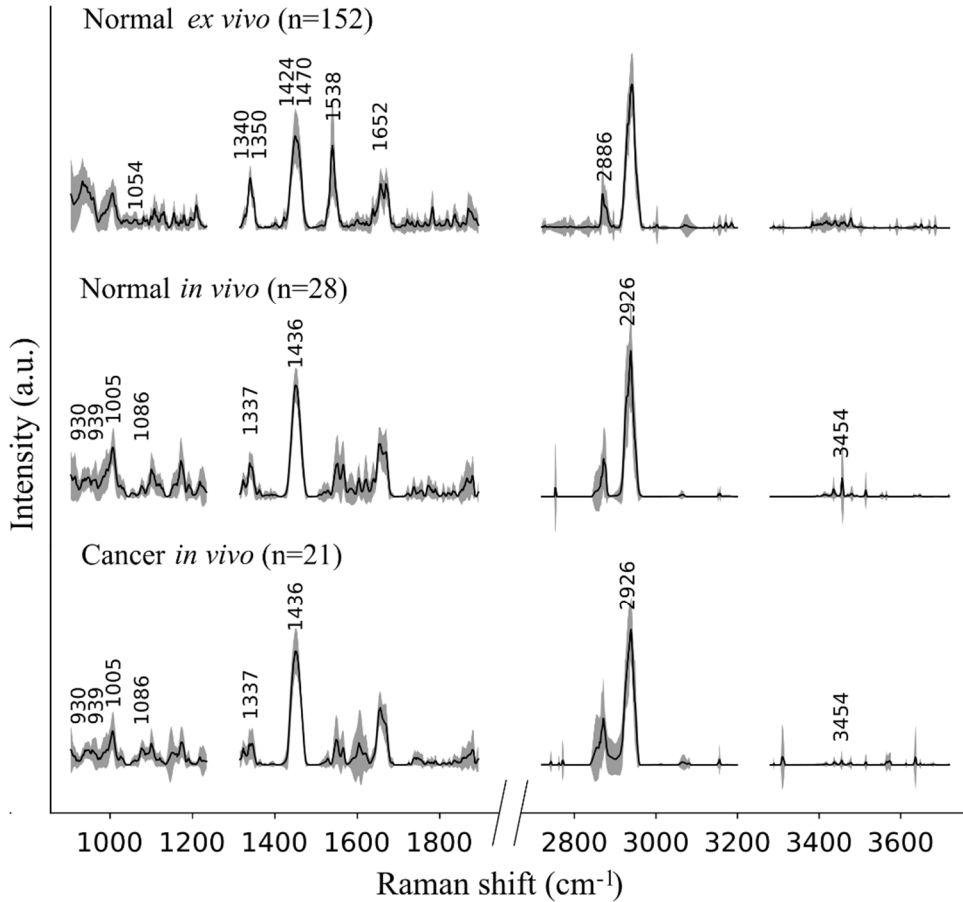


Figure 6.4 Average and standard deviation of processed spectra for normal and cancer *in vivo* spectra with all peaks used by the classification models labeled with their Raman shift in cm^{-1} .

The *ex vivo* spectra from normal prostate are shown for comparison.

However, subtle differences in peak intensities remained noticeable between classes by qualitative visual inspection. For instance, the intensities of the HWN lipids peak doublet at 2880/2886 cm^{-1}

shifts from right to left when comparing normal to cancer, with cancer border showing even intensity of the two peaks. Similarly, the amide peak at 1650 cm^{-1} was stronger for the cancer class but was identical between the cancer border and normal classes.

The *in vivo* acquisition from 18 patients led to 49 RS measurements, including 28 labeled as normal and 21 labeled as cancer. Figure 6.4 shows the average and standard deviation of these Raman measurements for FP ($500\text{-}2000\text{ cm}^{-1}$) and HWN ($2500\text{-}3800\text{ cm}^{-1}$) spectral domains. Also shown are the average and standard deviation of the 152 *ex vivo* Raman measurements labelled as normal prostate tissue to allow a spectra-to-spectra comparison of the biomolecular content of *ex vivo* normal tissue and *in vivo* spectra. Similarly to the *ex vivo* measurements, the *in vivo* spectra displayed the phenylalanine peak at 1000 cm^{-1} , collagen peaks at $1335/1440\text{ cm}^{-1}$, and amides peaks at $1535/1650\text{ cm}^{-1}$ in the FP region, as well as the lipids and protein peaks at $2880/2930\text{ cm}^{-1}$ in the HWN region. Although these spectral bands did not allow for strict discrimination between *in vivo* cancer and *in vivo* normal classes, slight differences remained visible. The phenylalanine and collagen peaks, at 1000 and 1335 cm^{-1} respectively, displayed higher intensity in normal measurements than in cancer, and an additional peak at 3454 cm^{-1} (O-H molecular bond) also displayed higher intensity in normal than in cancer.

Lastly, we identified one major difference between *ex vivo* normal spectra and *in vivo* spectra for the amide peak at 1535 cm^{-1} only. Figure 6.4 shows an intensity that is >3 times greater for *ex vivo* normal than it is for both *in vivo* spectra (normal and cancer).

6.4.2 Machine learning detection models

The classification model trained on the 179 *ex vivo* Raman measurements yielded an accuracy of 67%, a sensitivity of 63% and a specificity of 68%. This optimized statistical model was obtained with a ROC curve with an AUC of 0.72 and used eight spectral features. The classification model trained on the 49 *in vivo* Raman measurements yielded an accuracy of 79%, a sensitivity of 86% and a specificity of 72%. This optimized statistical model was obtained with a ROC curve with an AUC of 0.77 and used eight features.

These classification results between cancer and normal tissue are presented as ROC curves for the *ex vivo* and *in vivo* datasets in Figure 6.5a and 6.5b, respectively. Additionally, Figure 6.5c

and 6.5d list the Raman features used for both models and their molecular assignment based on the literature [68], [96], [105], [191]. Moreover, the *ex vivo* and *in vivo* models used DNA, RNA, proteins and lipids features. Amides, adenine and guanine at 1350/1470/1538/1652 cm⁻¹ served the *ex vivo* model only, while the phenylalanine at ~1000 cm⁻¹ was used only for the *in vivo* model. Finally, the collagen peak at 1335 cm⁻¹ was a feature in both models.

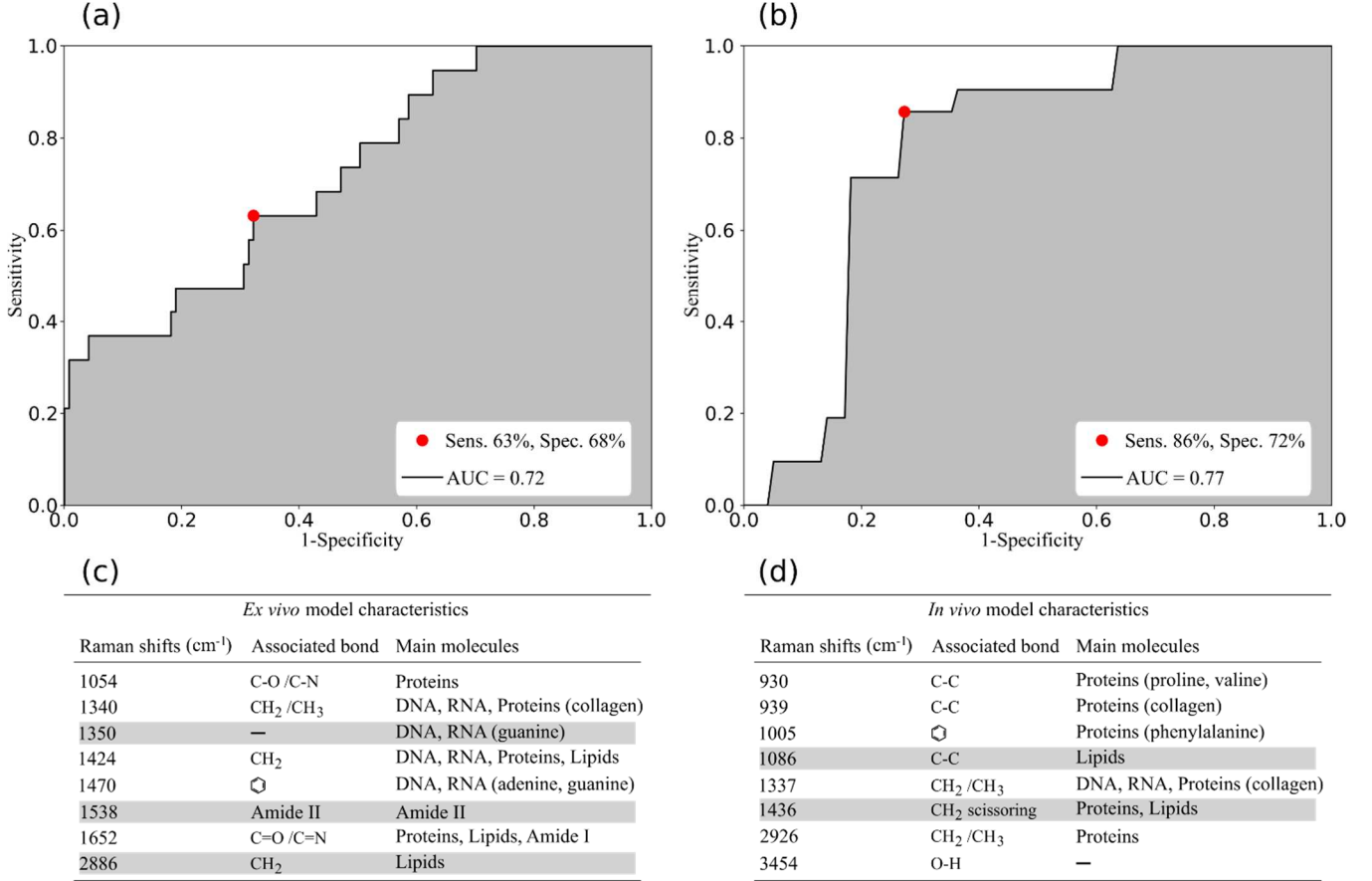


Figure 6.5 Receiver-operating characteristic (ROC) curve for discriminating normal from cancer prostatic tissue using Raman spectroscopy: (a) *ex vivo* model (b) *in vivo* model. List of Raman features associated with prostatic Raman-predicted molecular content that are used as inputs for the classification models: (c) *ex vivo*, (d) *in vivo*. Features with Raman band intensities higher in the cancer class are highlighted in gray. The molecular assignment of Raman peaks was based on literature findings [68], [96], [105], [191].

6.5 Discussion

Although limited in their accuracy, the classification models built from the *ex vivo* and *in vivo* datasets demonstrate that RS could discriminate PCa from normal tissue in a laboratory environment or *in situ* during surgery. On *in vivo* specimens, the spectra of normal and PCa showed differences in peaks at 1086 and 1436 cm⁻¹ (Figure 6.5c) while the *ex vivo* spectra showed differences at 2886 cm⁻¹ (Figure 6.5d). These differences are indicating the presence of greater amounts of lipids in cancer locations. The presence of lipids peaks has also been demonstrated in a study of prostate cancer by Medipally et al. (2020) [208] in which they found an alteration of lipid metabolism. Moreover, in this study the bands corresponding to lipids were more abundant in the plasma of prostate cancer patients compared to healthy individuals. Indeed, due to their high proliferation rate, cancer cells depend upon a large amount of metabolic energy to synthesize cellular membranes [209]. Lipids in cancer cells are therefore the main fuel source for membrane synthesis and become one of the major actors in tumor cells growth.

Furthermore, in the *ex vivo* specimens, the peak at 1350 cm⁻¹ assigned to DNA, RNA (guanine) is higher in intensity in cancerous prostate tissues than healthy tissues (Figure 6.5d). This is consistent with many studies that have demonstrated genetic dysregulation in PCa [210]–[213]. In a study by Gao et al. (2018) [214], they found that aggressive prostate cancer has the guanine allele- and thus, this allele was linked to higher expression of genes that are tied to the growth of cells and progression of tumors in prostate cancer.

The peak at 1538 cm⁻¹ assigned to the amide group is also higher in PCa patients, which implies an increase of protein concentration, and is consistent with the literature that found higher amide peak in breast cancer [215], lung cancer [216] and colorectal cancer tissues [217]. One of the proposed explanations for this difference is that it appears to inform on biological changes of malignancy such as increased alterations in protein structures and protein unfolding.

A limitation of the study is the small size of the datasets from which the classifiers were built. However, to minimize the likelihood of overfitting, we constrained the training process to using <10 features while the dataset size was at least five times larger. We also ensured -through qualitative inspection of the spectra- biomolecular interpretability of the features since the risk of overfitting rises with the use of features that are purely associated with statistical variance between observations. Another limitation relates to the limited reliability associated with the gold standard

of histology used to assign labels to each *ex vivo* measurement. The HPS staining used for histopathological analysis resulted in registration errors between Raman measurements of localization and the reconstructed prostates slices used to assign tissue labels (cancer vs. normal prostate). This limitation was mitigated for the measurements labeled as normal tissue in which a high margin of error criterium (2.5 mm radius confidence area) kept 152 normal measurements in the dataset but led to the removal of 20 measurements. However, when the same criterium, plus one that was more lenient (1.25 mm radius confidence area), was applied to measurements labeled as cancer, only 2 cancer and 25 cancer border measurements were retained. As a result, the cancer class, summing up to 27 measurements for the *ex vivo* dataset, showed not only a low number of measurements but was also at risk of containing mixed cancer and normal labels. These two major limitations of the *ex vivo* dataset present a plausible explanation of the underperformance of the resulting model in comparison with the classifiers trained with the *in vivo* dataset, which was limited only by its small sample size. Due to the small biopsy sample size for the *in vivo* dataset and the highly accurate co-location with the RS measurements, the gold standard (histology) accuracy was not limited by the spatial registration error between optical measurements and the sample's location.

To overcome the pitfalls of small datasets, a possible solution was to merge *ex vivo* and *in vivo* measurements. The spectra-to-spectra comparison highlighted their compatibility in terms of identified prostatic molecular contents (e.g., amides I, collagen, phenylalanine). The only notable exception was the 1535 cm^{-1} peak related to amide II, which was identified in all measurements but displayed an average intensity that was three times greater in the *ex vivo* measurements. However, merging of the two datasets solution was not used for this study due to the low reliability of the histology for the *ex vivo* dataset. Furthermore, this approach would require accounting for signal changes associated with temperature-induced optical properties variations. For example, Ghita et al. demonstrated that differences in temperature $>20^\circ\text{C}$ can affect the intensity of the collected signal and lead to Raman spectra changes [218].

Future efforts should focus on increasing the amount of data by increasing the number of recruited patients. The number of measurements obtained per patient was consistently less than four, but the acquisition time did not require more than 20% of the total experiment duration. Combining the robustness of our *in vivo* dataset acquisition method with a larger patient cohort would be the next step in evaluating PCa detection using our multimodal method based on the RS

system. Future work should also expand to other clinical applications with the same issue of tumor localization such as brachytherapy procedures. Indeed, the treatment procedure efficiency relies on the accurate radiation delivery dose on the tumor while minimizing healthy tissue exposition, and an assisting real-time Raman system would significantly improve the tumor outline detection. However, to avoid any registration problems caused by extra-cannulas insertion for the Raman probe, the tumor detection would need to be performed directly through the brachytherapy plastic guiding cannulas. This detection through a plastic layer has precedents and literature indicates that spatial offset Raman spectroscopy (SORS) could achieve it by providing depth resolution to the collected measurements [219].

6.6 Acknowledgments

This work is supported by the Discovery Grant program from the Natural Sciences and Engineering Research Council of Canada (NSERC), the Collaborative Health Research Program (CIHR and NSERC) and the TransMedTech Institute. We would also like to thank all the medical team at the radio-oncology department of CHUM.

6.7 Conflict of interest

We do not declare any conflict of interest concerning this study.

6.8 Code, Data and Materials Availability

The data and materials information that support the findings of this study are available from the corresponding author upon reasonable request.

CHAPITRE 7 DISCUSSION GÉNÉRALE

7.1 Buts de l'étude

La question du guidage des interventions chirurgicales couvre un large spectre de problèmes cliniques. Le problème du ciblage des tissus cancéreux lors de procédures de biopsies révèle en particulier un besoin critique pour de nouveaux systèmes et technologies. L'enjeu est de garantir le prélèvement d'un échantillon représentatif de la tumeur, menant au diagnostic le plus précis possible et assurant ainsi l'établissement d'une stratégie de traitement optimal. La contrainte principale demeure à chaque fois identique, il s'agit d'intégrer ces nouvelles technologies en ajoutant leur usage au traitement standard tout en ne modifiant pas ce dernier de sorte que l'effort d'adaptation de l'environnement clinique soit minimal voire nul. Dans ce contexte, la spectroscopie Raman apparaît comme une solution de choix pour la détection du cancer et ce pour plusieurs raisons. Tout d'abord, son contraste est basé sur les modes vibrationnels des molécules du milieu sondé, i.e. son utilisation repose sur un contraste intrinsèque des tissus et ne requiert aucun agent de contraste externe. De plus en n'étant pas limitée par la détection de certains fluorophores précis, comme c'est le cas de la spectroscopie de fluorescence, elle procure un moyen détection et de diagnostic avec un plus grand potentiel de sensibilité et spécificité. Ces atouts de la spectroscopie Raman sont cependant à mettre en perspective avec ses limites et les difficultés de son intégration en salle opératoire. La faiblesse du signal d'intérêt, la force du signal de background qui lui fait compétition et les contraintes de dimensionnement d'un prototype de sonde compatible avec le matériel chirurgical son autant de barrières faisant obstacle à cette intégration.

Mon projet de recherche portait spécifiquement sur le guidage des procédures de la prostate à l'aide de la spectroscopie Raman. L'objectif était de valider, à l'aide d'une étude sur patients humains, que cette technique optique permet de détecter les tissus cancéreux et que cette détection améliore la précision de guidage de la procédure. Cette thèse a menée au développement d'un système Raman combinant les plages spectrales *fingerprint* et *high wavenumber* ainsi qu'un capteur EM permettant son intégration dans la plateforme de navigation TRUS-IRM utilisée comme méthode de guidage standard.

7.2 Validation de la spectroscopie Raman *in situ* pour le guidage des biopsies de la prostate

L'objectif principal du projet était de valider *in situ* la détection de tissus cancéreux sur des patients humains à l'aide de la spectroscopie Raman. Afin d'y parvenir plusieurs objectifs intermédiaires ont été définis et réalisés. Le premier d'entre eux était l'établissement d'une preuve de concept, présentée dans le premier article, de l'intégration de méthodes optiques pour le guidage de procédures chirurgicales. Les objectifs 2 et 3 se concentraient sur le développement et la validation d'un nouveau prototype de sonde et du système optique dans son ensemble.

Afin d'optimiser et de valider préliminairement ce nouveau système, une expérience fut menée sur les échantillons de prostate *ex vivo* d'une cohorte de 14 patients recrutés au CHUM. Cette étude a révélé que le principal défi serait non seulement la faiblesse du signal brut provenant des tissus prostatiques mais surtout la très large prédominance du signal d'autofluorescence sur le signal Raman d'intérêt. Plusieurs solutions furent expérimentées pour y répondre. La première fut simplement dans l'amélioration du design du nouveau prototype de sonde. Il fut en effet manufacturé en deux versions, la seconde bénéficiant de l'ajout d'une lentille de focalisation ainsi que d'une fibre optique deux fois plus large pour l'illumination laser des tissus sondés. Ces ajouts/modifications ont permis, à durée d'acquisition constante, un gain de signal brut d'environ un ordre de grandeur de la seconde version (utilisée pour l'intégralité de l'étude *in vivo*) par rapport au premier modèle. La seconde solution proposée fut dans le choix du compromis lié aux paramètres d'acquisition : la puissance laser P, le temps d'intégration T et nombre d'accumulations par mesure n. Tandis que P et T furent maximisés tel qu'expliqué dans les chapitres 5 et 6, le nombre d'accumulations n fut semi-arbitrairement fixé à 50, voire 100 pour l'expérience *in vivo*. Ce choix fut pris dans l'idée de surdimensionner la valeur de ce paramètre et assurer le meilleur SNR possible pour la signature Raman extraite. L'étude *ex vivo* a ainsi mené à un premier modèle de classification discriminant entre les tissus cancéreux et sains avec une précision, une sensibilité et une spécificité de 67%, 63% et 68% respectivement.

Le deuxième défi majeur fut la faible quantité de points de données pour l'entraînement des modèles de classification entre les groupes "Cancer" et "Normal". Ce problème fut récurrent pour les études *ex vivo* et *in vivo*, bien que se matérialisant différemment. Dans le cas de l'étude *ex vivo*, il agit en conjonction avec le manque de fiabilité de l'étoile standard et la faible proportion de

points de données appartenant au groupe “Cancer”. Cette faiblesse de l’étalon standard est liée au manque de précision des techniques de recalage d’image entre les images des échantillons frais et les images histopathologiques. Cette limite, liée aux déformations non élastiques des tissus lors de leur coloration avec l’hematoxylin phloxine, est un problème dont il demeure difficile de s’affranchir. Elle conduit à un compromis entre la quantité de points rejetés, sur critère de confiance du diagnostic, et l’exactitude du diagnostic pour l’ensemble de donnée d’apprentissage. Dans le cas de l’étude *in vivo*, ce défi est directement lié au nombre réduit d’échantillons collectables par patients et indispensables au diagnostic de référence. Cette limite pourrait cependant être surmontée en reproduisant l’étude sur de plus longues périodes et en multipliant le nombre de patients recrutés. Malgré cette limite, les résultats présentés dans le troisième article rapportent la validation *in situ* du système Raman avec une précision de 79% ainsi qu’une sensibilité et une spécificité de 86% et 72% respectivement.

7.3 Développement d’un système multimodal

Un des éléments clefs de la méthodologie suivie pour ce projet de recherche fut l’aspect multimodal du système pour répondre au problème clinique. Le système Raman développé suite à l’objectif 2 se compose de deux sous-systèmes permettant de collecter la signature des régions *fingerprint* et *high wavenumber*. De plus l’utilisation du capteur EM dans le design du nouveau prototype de sonde a permis l’intégration du système optique dans la plateforme de navigation TRUS-IRM et a ainsi facilité sa validation au cours de l’étude *in vivo*. Ces différents sous-systèmes ont dû être précautionneusement développés en synchronisation afin que le système au complet soit prêt pour réaliser l’objectif 3, i.e. sa validation clinique. À cet égard, le choix de sacrifier le développement des systèmes de fluorescence et de réflectance diffuse s’explique par leur potentiel, pour le diagnostic des tissus, estimé plus faible que celui de la spectroscopie Raman. Le développement de ces deux sous-systèmes aurait nécessité une optimisation et une calibration délicate des sources de lumières et caméra additionnelles, ainsi que le développement d’un logiciel pour contrôler l’acquisition automatique des données. Ces différentes étapes nécessitent en général des validations itératives sur des mires anthropomorphiques aux propriétés optiques adaptées à ce type de système. Dans le cas d’un système combinant la spectroscopie de fluorescence et la réflectance diffuse, il

faut à la fois contrôler les coefficients d'absorption et de diffusion des mires mais aussi les concentrations des différents fluorophores ajoutés pour reproduire la fluorescence des tissus.

Comme présenté dans le chapitre 3, le choix a donc été fait de concentrer le projet sur l'approche Raman et de limiter le développement des autres sous-systèmes optiques. En conséquence bien que le nouveau prototype de sonde inclut une fibre optique sans filtres, permettant de collecter des signaux à larges spectres tels que ceux de fluorescence et de réflectance diffuse, le système optique final lui-même est limité à la spectroscopie Raman. Toutefois l'étude de la spectroscopie de fluorescences corrigée par les propriétés optiques n'a pas été abandonnée dans le LRO. Un système d'imagerie macroscopique, combinant la spectroscopie de fluorescence et l'imagerie par domaines de fréquences spatiales (SFDI) a été conçu par Émile Beaulieu (M. Sc. A du LRO). Ce système fonctionnant sur le principe du signal de fluorescence corrigé par les propriétés optiques a été testé sur des mires anthropomorphiques ainsi que sur des échantillons de prostate *ex vivo* [124]. Cette étude, menée parallèlement à ma thèse, fournit une preuve de concept de la faisabilité du diagnostic des tissus prostatiques grâce à la spectroscopie de fluorescence. Et elle constitue donc une forte incitation à la poursuite du développement des sous-systèmes optiques laissés inexploités dans mon projet de recherche.

CHAPITRE 8 CONCLUSION ET RECOMMANDATIONS

Le travail de recherche effectué au cours de ma thèse portait sur l'utilisation de la spectroscopie Raman pour détecter les tissus cancéreux lors des procédures de biopsie de la prostate. Plusieurs défis majeurs ont été rencontrés et ont mené à plusieurs contributions originales. Tel que montré dans le chapitre 5, la robustesse des méthodes de traitement de données permet de corriger les différences de manufacture et/ou de design entre systèmes. En conséquence il devient possible de construire des ensembles de données, compatibles les uns avec les autres, indépendamment des systèmes utilisés. Des études multicentriques permettraient notamment de construire de plus grands ensembles de données avec un coût en temps moindre. Mais il s'agit aussi d'une ouverture vers des changements dans la méthode d'entraînement des systèmes Raman pour le diagnostic des tissus.

En effet, comme discuté dans le chapitre 6, la question du recalage d'images entre échantillons frais et histopathologiques n'a pas de solution satisfaisante et limite la capacité de l'étalon standard à fournir un diagnostic de référence. C'est particulièrement le cas au voisinage des marges entre tissus sains et tissus cancéreux. Le problème de la colocalisation de l'échantillon histopathologique et de la mesure optique est cependant significativement réduit dans le cas de petits échantillons (de biopsie par exemple) comme le montrent les différences de résultat entre l'expérience *ex vivo* et *in situ*. De la même façon que l'expérience *ex vivo* a buté sur ce problème, on peut anticiper que la phase d'entraînement d'un système d'imagerie Raman macroscopique buterait sur le même problème, limitant sa précision. Ce que montrent les résultats du chapitre 5, c'est que cette difficulté pourrait être contournée en utilisant un système de sonde pour accumuler des données et entraîner un modèle de classification. Puis ce modèle pourrait être simplement exporté sur un système d'imagerie grand champs pour être utilisé avec le même niveau de précision. L'utilisation du système de sonde, plus simple et rapide, permettrait des acquisitions sur de petits échantillons pour éviter les erreurs de colocalisation. Le système grand champs pourrait être utilisé pour faire du diagnostic, cumulant les avantages d'une image macroscopique et la précision d'un modèle de classification robuste.

Le travail de recherche principal de ma thèse demeure la mise en évidence expérimentale de la capacité de la spectroscopie Raman à détecter les tissus cancéreux au cours d'une procédure

de biopsie de la prostate. L'expérience *in situ* sur 18 patients au CHUM constitue le cœur de cette contribution et est à ce jour la seule étude de ce genre appliquée à ce problème clinique. Comme discuté dans le chapitre 7, plusieurs limites existent encore et peuvent servir de base pour orienter des travaux futurs. L'aspect multimodal s'est montré déterminant dans la réussite du projet, il apparaît donc naturel de poursuivre dans cette voie pour améliorer la précision de diagnostic du système. Ainsi dans son état actuel, celui-ci combine la spectroscopie Raman et le guidage EM mais ces deux sous-systèmes ont été utilisés indépendamment. Pour renforcer l'aspect multimodal du système, les travaux futurs ne devraient pas se limiter à l'ajout de nouvelles modalités, telles que la spectroscopie de fluorescence et la spectroscopie de réflectance diffuse. Au contraire, la méthodologie à adopter devrait se concentrer sur la construction de nouveaux modèles de classification combinant les différentes sources d'information. Cette approche est celle qui a été retenue pour la suite du projet et a donné lieu à une publication de David Grajales (laboratoire MediCAL, Polytechnique Montréal) intitulée “Image-guided Raman spectroscopy navigation system to improve transperineal prostate cancer detection. Part 2: In-vivo tumor-targeting using a classification model combining spectral and MRI-radiomics features.” (Journal of Biomedical Optics, facteur d'impact = 3.73). Cet article, dont je suis deuxième auteur, est la partie 2 de l'article présenté au chapitre 6. Tout comme la partie 1, Il se concentre sur le développement d'un modèle de classification entre tissus sains et tissus cancéreux. Il se distingue cependant par son modèle de classification construit à partir des données Raman ainsi que de données IRM multiparamétriques, colocalisée avec les mesures optiques grâce au guidage EM. L'objectif de cette étude était la mise en évidence de l'augmentation significative de la précision du modèle de classification au fur et à mesure de l'inclusion des informations issues de l'IRM. Cet objectif est atteint car la précision augmente d'environ 10% (de 79% à 89%) entre le modèle basé seulement sur les données Raman et celui combinant les données Raman et IRM multiparamétriques. Cependant la partie 2 souffre de la même limite que la partie 1. La quantité de points de donnée, environ une cinquantaine, est la même pour les deux modèles de classification. Et bien que le nombre de paramètres utilisés soit bridé à moins de 10 pour éviter tout phénomène de sur-apprentissage, la confiance dans la généralisation des résultats ne peut être définitivement acquise qu'en poursuivant l'accumulation des données pour augmenter la taille des ensembles disponibles.

Plusieurs éléments viennent supporter l'originalité de mon projet de recherche. Tout d'abord jamais une sonde Raman n'avait été intégrée avec un capteur EM afin de l'insérer dans

une plateforme de navigation TRUS-IRM. Ensuite la classification des tissus prostatiques, sains ou cancéreux, n'avaient jamais été réalisées *in situ* chez l'Homme en utilisant un système de sonde basé sur la spectroscopie Raman. La poursuite du développement de ce système optique multimodal a le potentiel de donner aux chirurgiens des informations de contraste biomoléculaire en plus des informations anatomiques habituelles. En conséquence une caractérisation plus subtile et plus précise des tissus devient possible pour guider l'insertion des instruments lors des procédures chirurgicales. Ce changement de paradigme constitue un impact clinique considérable car il a le potentiel de générer un saut de performance dans la précision des dites procédures. Dans le cas de la biopsie de la prostate, cette amélioration causée par la technologie Raman, réduirait grandement le risque de collecter des échantillons non représentatifs. Le besoin induit de renouveler les procédures de biopsie serait donc réduit, avec tous les avantages que cela implique sur les risques chirurgicaux moindres pour le patient ainsi que l'amélioration de son confort et de sa qualité de vie. Cette thèse a démontré la faisabilité d'intégration de la spectroscopie Raman, couplée au guidage EM, dans le flux chirurgical standard de la procédure de biopsie de la prostate guidée par TRUS-IRM. Malgré les nouveaux défis découverts au cours de ce travail de recherche, les résultats obtenus ouvrent la voie à une intégration clinique toujours plus poussée ainsi qu'à la translation des technologies développées vers d'autres procédures, telle que la brachythérapie.

RÉFÉRENCES

- [1] W. M. Butler, G. S. Merrick, A. T. Dorsey, J. H. Lief, and R. W. Galbreath, “Modern prostate brachytherapy,” *Med. Dosim.*, vol. 25, no. 3, pp. 149–153, 2000, doi: 10.1016/S0958-3947(00)00041-8.
- [2] M. A. Penna, K. A. Dines, R. Seip, R. F. Carlson, and N. T. Sanghvi, “Modeling prostate anatomy from multiple view TRUS images for image-guided HIFU therapy,” *IEEE Trans. Ultrason. Ferroelectr. Freq. Control*, vol. 54, no. 1, pp. 52–68, 2007, doi: 10.1109/TUFFC.2007.211.
- [3] N. Hata *et al.*, “MR imaging-guided prostate biopsy with surgical navigation software: Device validation and feasibility,” *Radiology*, vol. 220, no. 1, pp. 263–268, 2001, doi: 10.1148/radiology.220.1.r01jl44263.
- [4] Y. Hu, “Registration of Magnetic Resonance and Ultrasound Images for Guiding Prostate Cancer Interventions,” 2013.
- [5] P. A. Pinto *et al.*, “Magnetic resonance imaging/ultrasound fusion guided prostate biopsy improves cancer detection following transrectal ultrasound biopsy and correlates with multiparametric magnetic resonance imaging,” *J. Urol.*, vol. 186, no. 4, pp. 1281–1285, 2011, doi: 10.1016/j.juro.2011.05.078.
- [6] Canadian Cancer Society, “Canadian Cancer Statistics Special topic : Predictions of the future burden of cancer in Canada,” *Public Heal. Agency Canada*, pp. 1–151, 2015, doi: Canadian Cancer Society.
- [7] R. L. Siegel, K. D. Miller, H. E. Fuchs, and A. Jemal, “Cancer Statistics, 2021,” *CA. Cancer J. Clin.*, vol. 71, no. 1, pp. 7–33, 2021, doi: 10.3322/caac.21654.
- [8] W. Causes and P. Cancer, “What is Prostate Cancer ? Symptoms,” pp. 1–9, 2018.
- [9] P. Chung and K. Noonan, “Grades du cancer de la prostate.” <https://cancer.ca/fr/cancer-information/cancer-types/prostate/grading>.
- [10] P. McKenzie, B. Delahunt, K. DeVoss, B. Ross, H. Tran, and K. Sikaris, “Prostate specific antigen testing for the diagnosis of prostate cancer,” *Pathology*, vol. 43, no. 5, p. 403, 2011,

doi: 10.1097/PAT.0b013e32834915fc.

- [11] J. H. Hayes and M. J. Barry, "Screening for prostate cancer with the prostate-specific antigen test: A review of current evidence," *JAMA - J. Am. Med. Assoc.*, vol. 311, no. 11, pp. 1143–1149, 2014, doi: 10.1001/jama.2014.2085.
- [12] X. Filella and L. Foj, "Novel biomarkers for prostate cancer detection and prognosis," *Adv. Exp. Med. Biol.*, vol. 1095, pp. 15–39, 2018, doi: 10.1007/978-3-319-95693-0_2.
- [13] H. Schatten, "Brief overview of prostate cancer statistics, grading, diagnosis and treatment strategies," *Adv. Exp. Med. Biol.*, vol. 1095, pp. 1–14, 2018, doi: 10.1007/978-3-319-95693-0_1.
- [14] J. Crook *et al.*, "Ultrasound-planned high-dose-rate prostate brachytherapy: Dose painting to the dominant intraprostatic lesion," *Brachytherapy*, vol. 13, no. 5, pp. 433–441, 2014, doi: 10.1016/j.brachy.2014.05.006.
- [15] P. A. Pinto *et al.*, "J Urol," vol. 186, no. 4, pp. 1281–1285, 2011, doi: 10.1016/j.juro.2011.05.078.Magnetic.
- [16] A. R. Rastinehad *et al.*, "D'Amico risk stratification correlates with degree of suspicion of prostate cancer on multiparametric magnetic resonance imaging," *J. Urol.*, vol. 185, no. 3, pp. 815–820, 2011, doi: 10.1016/j.juro.2010.10.076.
- [17] F. Rabbani, N. Stroumbakis, B. R. Kava, M. S. Cookson, and W. R. Fair, "Incidence and clinical significance of false-negative sextant prostate biopsies," *J. Urol.*, vol. 159, no. 4, pp. 1247–1250, 1998, doi: 10.1016/S0022-5347(01)63574-2.
- [18] M. A. Bjurlin, J. S. Wysock, and S. S. Taneja, "Optimization of prostate biopsy: Review of technique and complications," *Urol. Clin. North Am.*, vol. 41, no. 2, pp. 299–313, 2014, doi: 10.1016/j.ucl.2014.01.011.
- [19] J. Zhou, E. Sebastian, V. Mangona, and D. Yan, "Real-time catheter tracking for high-dose-rate prostate brachytherapy using an electromagnetic 3D-guidance device: A preliminary performance study," *Med. Phys.*, vol. 40, no. 2, pp. 1–8, 2013, doi: 10.1118/1.4788641.
- [20] S. Bharat *et al.*, "Electromagnetic tracking for catheter reconstruction in ultrasound-guided high-dose-rate brachytherapy of the prostate," *Brachytherapy*, vol. 13, no. 6, pp. 640–650,

2014, doi: 10.1016/j.brachy.2014.05.012.

- [21] E. Poulin, E. Racine, D. Binnekamp, and L. Beaulieu, “Fast, automatic, and accurate catheter reconstruction in HDR brachytherapy using an electromagnetic 3D tracking system,” *Med. Phys.*, vol. 42, no. 3, pp. 1227–1232, 2015, doi: 10.1118/1.4908011.
- [22] K. M. Pondman *et al.*, “MR-Guided Biopsy of the Prostate: An Overview of Techniques and a Systematic Review,” *Eur. Urol.*, vol. 54, no. 3, pp. 517–527, 2008, doi: 10.1016/j.eururo.2008.06.001.
- [23] B. Turkbey, P. A. Pinto, and P. L. Choyke, “Imaging techniques for prostate cancer: Implications for focal therapy,” *Nat. Rev. Urol.*, vol. 6, no. 4, pp. 191–203, 2009, doi: 10.1038/nrurol.2009.27.
- [24] J. Nakashima *et al.*, “Endorectal MRI for prediction of tumor site, tumor size, and local extension of prostate cancer,” *Urology*, vol. 64, no. 1, pp. 101–105, 2004, doi: 10.1016/j.urology.2004.02.036.
- [25] M. Roethke *et al.*, “MRI-guided prostate biopsy detects clinically significant cancer: Analysis of a cohort of 100 patients after previous negative TRUS biopsy,” *World J. Urol.*, vol. 30, no. 2, pp. 213–218, 2012, doi: 10.1007/s00345-011-0675-2.
- [26] S. Il Hwang *et al.*, “Value of MR-US fusion in guidance of repeated prostate biopsy in men with PSA < 10 ng/mL,” *Clin. Imaging*, vol. 53, no. April 2018, pp. 1–5, 2019, doi: 10.1016/j.clinimag.2018.09.012.
- [27] S. Natarajan *et al.*, “Clinical application of a 3D ultrasound-guided prostate biopsy system,” *Urol. Oncol. Semin. Orig. Investig.*, vol. 29, no. 3, pp. 334–342, 2011, doi: 10.1016/j.urolonc.2011.02.014.
- [28] A. Sedghi *et al.*, “Deep neural maps for unsupervised visualization of high-grade cancer in prostate biopsies,” *Int. J. Comput. Assist. Radiol. Surg.*, vol. 14, no. 6, pp. 1009–1016, 2019, doi: 10.1007/s11548-019-01950-0.
- [29] S. Kadoury *et al.*, “Realtime TRUS/MRI fusion targeted-biopsy for prostate cancer: A clinical demonstration of increased positive biopsy rates,” *Lect. Notes Comput. Sci. (including Subser. Lect. Notes Artif. Intell. Lect. Notes Bioinformatics)*, vol. 6367 LNCS, pp. 52–62, 2010, doi: 10.1007/978-3-642-15989-3_7.

- [30] C. Kallaway *et al.*, “Advances in the clinical application of Raman spectroscopy for cancer diagnostics,” *Photodiagnosis Photodyn. Ther.*, vol. 10, no. 3, pp. 207–219, 2013, doi: 10.1016/j.pdpt.2013.01.008.
- [31] M. Jermyn *et al.*, “A review of Raman spectroscopy advances with an emphasis on clinical translation challenges in oncology,” *Phys. Med. Biol.*, vol. 61, no. 23, pp. R370–R400, 2016, doi: 10.1088/0031-9155/61/23/R370.
- [32] M. Jermyn *et al.*, “Highly accurate detection of cancer *in situ* with intraoperative, label-free, multimodal optical spectroscopy,” *Cancer Res.*, vol. 77, no. 14, pp. 3942–3950, 2017, doi: 10.1158/0008-5472.CAN-17-0668.
- [33] S. R. Arridge, “Optical tomography in medical imaging,” *Inverse Probl.*, vol. 15, no. 2, 1999, doi: 10.1088/0266-5611/15/2/022.
- [34] C. Boudoux, “*Light transport in tissue*” in “*Fundamentals of Biomedical Optics, From light interactions with cells to complex imaging system*” 1st edition, United States of America: Pollux Editions, 2017, pp 237-260. .
- [35] B. Davison, *Neutron Transport Theory*. Oxford: Oxford University Press, 1957.
- [36] D. S. Anikonov, “*Tomography through the transport equation*” in “*Computational Radiology and Imaging: Therapy and Diagnosis*” (IMA Volumes in Mathematics and its Applications 110) Berlin (Springer) : ed C Borgers and F Natterer, 1998. .
- [37] A. P. Gibson, J. C. Hebden, and S. R. Arridge, “Recent advances in diffuse optical imaging,” *Phys. Med. Biol.*, vol. 50, no. 4, 2005, doi: 10.1088/0031-9155/50/4/R01.
- [38] S. L. Jacques and B. W. Pogue, “Tutorial on diffuse light transport,” *J. Biomed. Opt.*, vol. 13, no. 4, p. 041302, 2008, doi: 10.1117/1.2967535.
- [39] B. C. Wilson, “[1] Wilson_B_1983 monte carlo light absorption tissues.pdf.” 1983.
- [40] L. Wang, S. L. Jaques, and L. Zheng, “MCML-Monte Carlo modeling of light transport in multi-layered Tissues,” *Computer Methods and Programs in Biomedicine*, vol. 47, no. 2. pp. 131–146, 1995, [Online]. Available: oilab.seas.wustl.edu/epub/1995LWCMPBMcml.pdf%0Awww.ncbi.nlm.nih.gov/pubmed/7587160.

- [41] S. A. Prahl, “A Monte Carlo model of light propagation in tissue,” *Dosim. Laser Radiat. Med. Biol.*, vol. 10305, no. 1989, p. 1030509, 1989, doi: 10.1117/12.2283590.
- [42] H. Shen and G. Wang, “A tetrahedron-based inhomogeneous Monte Carlo optical simulator,” *Phys. Med. Biol.*, vol. 55, no. 4, pp. 947–962, 2010, doi: 10.1088/0031-9155/55/4/003.
- [43] Q. Fang, “Mesh-based Monte Carlo method using fast ray-tracing in Plücker coordinates,” *Biomed. Opt. Express*, vol. 1, no. 1, p. 165, 2010, doi: 10.1364/boe.1.000165.
- [44] Q. Fang and D. R. Kaeli, “Accelerating mesh-based Monte Carlo method on modern CPU architectures,” *Biomed. Opt. Express*, vol. 3, no. 12, p. 3223, 2012, doi: 10.1364/boe.3.003223.
- [45] A. Goyette *et al.*, “Sub-diffuse interstitial optical tomography to improve the safety of brain needle biopsies: a proof-of-concept study,” *Opt. Lett.*, vol. 40, no. 2, p. 170, 2015, doi: 10.1364/ol.40.000170.
- [46] G. Hong, A. L. Antaris, and H. Dai, “Near-infrared fluorophores for biomedical imaging,” *Nat. Biomed. Eng.*, vol. 1, no. 1, 2017, doi: 10.1038/s41551-016-0010.
- [47] K. D. Paulsen and H. Jiang, “Spatially varying optical property reconstruction using a finite element diffusion equation approximation,” *Med. Phys.*, vol. 22, no. 6, pp. 691–701, 1995, doi: 10.1118/1.597488.
- [48] M. Schweiger, S. R. Arridge, and D. T. Delpy, “Application of the finite-element method for the forward and inverse models in optical tomography,” *J. Math. Imaging Vis.*, vol. 3, no. 3, pp. 263–283, 1993, doi: 10.1007/BF01248356.
- [49] J. P. VanHouten, D. A. Benaron, S. Spilman, and Stevenson D. K., “maging brain injury using time-resolved near infrared light scanning,” *Pediatr Res*, vol. 39, no. 3, pp. 470–476, 1996.
- [50] A. T. Eggenbrecht *et al.*, “Mapping distributed brain function and networks with diffuse optical tomography,” *Nat. Photonics*, vol. 8, no. 6, pp. 448–454, 2014, doi: 10.1038/nphoton.2014.107.
- [51] A. A. Sari, M. Mobinizadeh, and M. Azadbakht, “A systematic review of the effects of

- diffuse optical imaging in breast diseases,” *Iran. J. Cancer Prev.*, vol. 6, no. 1, pp. 44–51, 2013.
- [52] W. Zhi *et al.*, “Solid breast lesions: Clinical experience with US-guided diffuse optical tomography combined with conventional US,” *Radiology*, vol. 265, no. 2, pp. 371–378, 2012, doi: 10.1148/radiol.12120086.
- [53] R. Shaikh *et al.*, “A comparative evaluation of diffuse reflectance and Raman spectroscopy in the detection of cervical cancer,” *J. Biophotonics*, vol. 10, no. 2, pp. 242–252, 2017, doi: 10.1002/jbio.201500248.
- [54] A. Garcia-Uribe, J. Zou, M. Duvic, J. H. Cho-Vega, V. G. Prieto, and L. V. Wang, “In vivo diagnosis of melanoma and nonmelanoma skin cancer using oblique incidence diffuse reflectance spectrometry,” *Cancer Res.*, vol. 72, no. 11, pp. 2738–2745, 2012, doi: 10.1158/0008-5472.CAN-11-4027.
- [55] W. Stummer *et al.*, “Intraoperative detection of malignant gliomas by 5-aminolevulinic acid-induced porphyrin fluorescence,” *Neurosurgery*, vol. 42, no. 3, pp. 518–526, 1998, doi: 10.1097/00006123-199803000-00017.
- [56] W. Stummer, U. Pichlmeier, T. Meinel, O. D. Wiestler, F. Zanella, and H. J. Reulen, “Fluorescence-guided surgery with 5-aminolevulinic acid for resection of malignant glioma: a randomised controlled multicentre phase III trial,” *Lancet Oncol.*, vol. 7, no. 5, pp. 392–401, 2006, doi: 10.1016/S1470-2045(06)70665-9.
- [57] M. Jermyn *et al.*, “Highly accurate detection of cancer in situ with intraoperative, label-free, multimodal optical spectroscopy,” *Cancer Res.*, vol. 77, no. 14, pp. 3942–3950, 2017, doi: 10.1158/0008-5472.CAN-17-0668.
- [58] J. J. Bravo, J. D. Olson, S. C. Davis, D. W. Roberts, K. D. Paulsen, and S. C. Kanick, “Hyperspectral data processing improves PpIX contrast during fluorescence guided surgery of human brain tumors,” *Sci. Rep.*, vol. 7, no. 1, pp. 1–13, 2017, doi: 10.1038/s41598-017-09727-8.
- [59] A. Kim, M. Roy, F. Dadani, and B. C. Wilson, “A fiberoptic reflectance probe with multiple source-collector separations to increase the dynamic range of derived tissue optical absorption and scattering coefficients,” *Opt. Express*, vol. 18, no. 6, p. 5580, 2010, doi:

10.1364/oe.18.0005580.

- [60] A. Kim, M. Khurana, Y. Moriyama, and B. C. Wilson, “Quantification of in vivo fluorescence decoupled from the effects of tissue optical properties using fiber-optic spectroscopy measurements,” *J. Biomed. Opt.*, vol. 15, no. 6, p. 067006, 2010, doi: 10.1117/1.3523616.
- [61] C. Zhu, G. M. Palmer, T. M. Breslin, J. Harter, and N. Ramanujam, “Diagnosis of breast cancer using fluorescence and diffuse reflectance spectroscopy: a Monte-Carlo-model-based approach,” *J. Biomed. Opt.*, vol. 13, no. 3, p. 034015, 2008, doi: 10.1117/1.2931078.
- [62] X. Zheng, H. Xiong, Y. Li, B. Han, and J. Sun, “Application of Quantitative Autofluorescence Bronchoscopy Image Analysis Method in Identifying Bronchopulmonary Cancer,” *Technol. Cancer Res. Treat.*, vol. 16, no. 4, pp. 482–487, 2017, doi: 10.1177/1533034616656466.
- [63] K. Fostiroopoulos, C. Arens, C. Betz, and M. Kraft, “Nichtinvasive Bildgebung mittels Autofluoreszenzendoskopie: Stellenwert bei der Früherfassung des Kehlkopfkarzinoms,” *HNO*, vol. 64, no. 1, pp. 13–18, 2016, doi: 10.1007/s00106-015-0095-5.
- [64] Z. Volynskaya *et al.*, “Diagnosing breast cancer using diffuse reflectance spectroscopy and intrinsic fluorescence spectroscopy,” *J. Biomed. Opt.*, vol. 13, no. 2, p. 024012, 2008, doi: 10.1117/1.2909672.
- [65] E. Tanis *et al.*, “In vivo tumor identification of colorectal liver metastases with diffuse reflectance and fluorescence spectroscopy,” *Lasers Surg. Med.*, vol. 48, no. 9, pp. 820–827, 2016, doi: 10.1002/lsm.22581.
- [66] E. Smith and G. Dent, *Modern Raman spectroscopy—a practical approach*. Ewen Smith and Geoffrey Dent. John Wiley and Sons Ltd, Chichester, 2005. Pp. 210. ISBN 0 471 49668 5 (cloth, hb); 0 471 49794 0 (pbk), vol. 36, no. 8. 2005.
- [67] K. Lin, W. Zheng, J. Wang, C. M. Lim, and Z. Huang, “Simultaneous fingerprint and high-wavenumber fiber-optic Raman endoscopy for in vivo diagnosis of laryngeal cancer,” *Photonic Ther. Diagnostics XII*, vol. 9689, p. 96892B, 2016, doi: 10.1117/12.2213964.
- [68] K. Aubertin *et al.*, “Combining high wavenumber and fingerprint Raman spectroscopy for the detection of prostate cancer during radical prostatectomy,” *Biomed. Opt. Express*, vol.

- 9, no. 9, p. 4294, 2018, doi: 10.1364/boe.9.004294.
- [69] M. S. Bergholt *et al.*, “Simultaneous fingerprint and high-wavenumber fiber-optic Raman spectroscopy enhances real-time *in vivo* diagnosis of adenomatous polyps during colonoscopy,” *J. Biophotonics*, vol. 9, no. 4, pp. 333–342, 2016, doi: 10.1002/jbio.201400141.
- [70] C. Boudoux, “Scattering” in “*Fundamentals of Biomedical Optics, From light interactions with cells to complex imaging system*” 1st edition, United States of America: Pollux Editions, 2017, pp 230-237. .
- [71] S. Dochow *et al.*, “Etaloning, fluorescence and ambient light suppression by modulated wavelength Raman spectroscopy,” *Biomed. Spectrosc. Imaging*, vol. 1, no. 4, pp. 383–389, 2012, doi: 10.3233/bsi-120031.
- [72] J. Zhao, H. Lui, D. I. Mclean, and H. Zeng, “Automated autofluorescence background subtraction algorithm for biomedical raman spectroscopy,” *Appl. Spectrosc.*, vol. 61, no. 11, pp. 1225–1232, 2007, doi: 10.1366/000370207782597003.
- [73] J. F. Kelly, T. A. Blake, B. E. Bernacki, and T. J. Johnson, “Design Considerations for a Portable Raman Probe Spectrometer for Field Forensics,” *Int. J. Spectrosc.*, vol. 2012, pp. 1–15, 2012, doi: 10.1155/2012/938407.
- [74] K. Kong, C. Kendall, N. Stone, and I. Notingher, “Raman spectroscopy for medical diagnostics - From *in-vitro* biofluid assays to *in-vivo* cancer detection,” *Adv. Drug Deliv. Rev.*, vol. 89, pp. 121–134, 2015, doi: 10.1016/j.addr.2015.03.009.
- [75] Y. Shen, J. Yue, W. Xu, and S. Xu, “Recent progress of surface-enhanced Raman spectroscopy for subcellular compartment analysis,” *Theranostics*, vol. 11, no. 10, pp. 4872–4893, 2021, doi: 10.7150/thno.56409.
- [76] J. Yue, Y. Shen, C. Liang, W. Shi, W. Xu, and S. Xu, “Investigating Lysosomal Autophagy via Surface-Enhanced Raman Scattering Spectroscopy,” *Anal. Chem.*, vol. 93, no. 38, pp. 13038–13044, 2021, doi: 10.1021/acs.analchem.1c02939.
- [77] S. Feng *et al.*, “A noninvasive cancer detection strategy based on gold nanoparticle surface-enhanced raman spectroscopy of urinary modified nucleosides isolated by affinity chromatography,” *Biosens. Bioelectron.*, vol. 91, pp. 616–622, 2017, doi:

- 10.1016/j.bios.2017.01.006.
- [78] Y. Xing *et al.*, “Raman observation of a molecular signaling pathway of apoptotic cells induced by photothermal therapy,” *Chem. Sci.*, vol. 10, no. 47, pp. 10900–10910, 2019, doi: 10.1039/c9sc04389f.
 - [79] M. R. K. Ali *et al.*, “Simultaneous Time-Dependent Surface-Enhanced Raman Spectroscopy, Metabolomics, and Proteomics Reveal Cancer Cell Death Mechanisms Associated with Gold Nanorod Photothermal Therapy,” *J. Am. Chem. Soc.*, vol. 138, no. 47, pp. 15434–15442, 2016, doi: 10.1021/jacs.6b08787.
 - [80] J. Ando, K. Fujita, N. I. Smith, and S. Kawata, “Dynamic SERS imaging of cellular transport pathways with endocytosed gold nanoparticles,” *Nano Lett.*, vol. 11, no. 12, pp. 5344–5348, 2011, doi: 10.1021/nl202877r.
 - [81] S. Yerolatsitis *et al.*, “Ultra-low background Raman sensing using a negative-curvature fibre and no distal optics,” *J. Biophotonics*, vol. 12, no. 3, pp. 1–6, 2019, doi: 10.1002/jbio.201800239.
 - [82] Q. Tu and C. Chang, “Diagnostic applications of Raman spectroscopy,” *Nanomedicine Nanotechnology, Biol. Med.*, vol. 8, no. 5, pp. 545–558, 2012, doi: 10.1016/j.nano.2011.09.013.
 - [83] C. L. Evans, E. O. Potma, M. Puoris’haag, D. Côté, C. P. Lin, and X. S. Xie, “Chemical imaging of tissue in vivo with video-rate coherent anti-Stokes Raman scattering microscopy,” *Proc. Natl. Acad. Sci. U. S. A.*, vol. 102, no. 46, pp. 16807–16812, 2005, doi: 10.1073/pnas.0508282102.
 - [84] F. Légaré, C. L. Evans, F. Ganikhanov, and X. S. Xie, “Abstract :,” vol. 14, no. 10, pp. 4427–4432, 2006.
 - [85] B. G. Saar, R. S. Johnston, C. W. Freudiger, X. S. Xie, and E. J. Seibel, “Coherent Raman scanning fiber endoscopy,” *Opt. Lett.*, vol. 36, no. 13, p. 2396, 2011, doi: 10.1364/ol.36.002396.
 - [86] M. Balu, G. Liu, Z. Chen, B. J. Tromberg, and E. O. Potma, “Fiber delivered probe for efficient CARS imaging of tissues,” *Opt. Express*, vol. 18, no. 3, p. 2380, 2010, doi: 10.1364/oe.18.002380.

- [87] J. Zheng *et al.*, “Vibrational phase imaging in wide-field CARS for nonresonant background suppression,” *Opt. Express*, vol. 23, no. 8, p. 10756, 2015, doi: 10.1364/oe.23.010756.
- [88] A. Alfonso-García, R. Mittal, E. S. Lee, and E. O. Potma, “Biological imaging with coherent Raman scattering microscopy: a tutorial,” *J. Biomed. Opt.*, vol. 19, no. 7, p. 071407, 2014, doi: 10.1117/1.jbo.19.7.071407.
- [89] B. G. Saar, C. W. Freudiger, J. Reichman, C. M. Stanley, G. R. Holtom, and X. S. Xie, “Video-rate molecular imaging *in vivo* with stimulated Raman scattering,” *Science (80-.).*, vol. 330, no. 6009, pp. 1368–1370, 2010, doi: 10.1126/science.1197236.
- [90] C. W. Freudiger, W. Yang, G. R. Holtom, N. Peyghambarian, X. S. Xie, and K. Q. Kieu, “Stimulated Raman scattering microscopy with a robust fibre laser source,” *Nat. Photonics*, vol. 8, no. 2, pp. 153–159, 2014, doi: 10.1038/nphoton.2013.360.
- [91] D. Fu *et al.*, “Quantitative chemical imaging with multiplex stimulated Raman scattering microscopy,” *J. Am. Chem. Soc.*, vol. 134, no. 8, pp. 3623–3626, 2012, doi: 10.1021/ja210081h.
- [92] C. S. Liao *et al.*, “Optical Microscopy: Spectrometer-free vibrational imaging by retrieving stimulated Raman signal from highly scattered photons,” *Sci. Adv.*, vol. 1, no. 9, pp. 1–9, 2015, doi: 10.1126/sciadv.1500738.
- [93] P. Berto, E. R. Andresen, and H. Rigneault, “Background-free stimulated raman spectroscopy and microscopy,” *Phys. Rev. Lett.*, vol. 112, no. 5, pp. 1–5, 2014, doi: 10.1103/PhysRevLett.112.053905.
- [94] I. Latka, S. Dochow, C. Krafft, B. Dietzek, and J. Popp, “Fiber optic probes for linear and nonlinear Raman applications - Current trends and future development,” *Laser Photonics Rev.*, vol. 7, no. 5, pp. 698–731, 2013, doi: 10.1002/lpor.201200049.
- [95] H. Salehi *et al.*, “Confocal Raman spectroscopy to monitor intracellular penetration of TiO₂ nanoparticles,” *J. Raman Spectrosc.*, vol. 45, no. 9, pp. 807–813, 2014, doi: 10.1002/jrs.4561.
- [96] A. A. Grosset *et al.*, “Identification of intraductal carcinoma of the prostate on tissue specimens using Raman micro-spectroscopy: A diagnostic accuracy case–control study with multicohort validation,” *PLoS Med.*, vol. 17, no. 8 August, pp. 1–20, 2020, doi: 10.1371/journal.pmed.1009330.

- 10.1371/JOURNAL.PMED.1003281.
- [97] I. Pence and A. Mahadevan-Jansen, “Clinical instrumentation and applications of Raman spectroscopy,” *Chem. Soc. Rev.*, vol. 45, no. 7, pp. 1958–1979, 2016, doi: 10.1039/c5cs00581g.
 - [98] M. Jermyn *et al.*, “Intraoperative brain cancer detection with Raman spectroscopy in humans,” *Sci. Transl. Med.*, vol. 7, no. 274, pp. 1–10, 2015, doi: 10.1126/scitranslmed.aaa2384.
 - [99] J. Desroches *et al.*, “Characterization of a Raman spectroscopy probe system for intraoperative brain tissue classification,” *Biomed. Opt. Express*, vol. 6, no. 7, p. 2380, 2015, doi: 10.1364/boe.6.002380.
 - [100] J. Desroches *et al.*, “A new method using Raman spectroscopy for in vivo targeted brain cancer tissue biopsy,” *Sci. Rep.*, vol. 8, no. 1, pp. 1–10, 2018, doi: 10.1038/s41598-018-20233-3.
 - [101] M. D. Keller *et al.*, “Development of a spatially offset Raman spectroscopy probe for breast tumor surgical margin evaluation,” *J. Biomed. Opt.*, vol. 16, no. 7, p. 077006, 2011, doi: 10.1117/1.3600708.
 - [102] S. Mosca *et al.*, “Spatially Offset Raman Spectroscopy—How Deep?,” *Anal. Chem.*, vol. 93, no. 17, pp. 6755–6762, 2021, doi: 10.1021/acs.analchem.1c00490.
 - [103] M. V. P. Chowdary, K. K. Kumar, J. Kurien, S. Mathew, and C. M. Krishna1, “Discrimination of Normal, Benign, and Malignant Breast Tissues by Raman Spectroscopy,” *Biopolymers*, vol. 85, no. 4, pp. 392–406, 2007, doi: 10.1002/bip.
 - [104] P. Matousek and N. Stone, “Prospects for the diagnosis of breast cancer by noninvasive probing of calcifications using transmission Raman spectroscopy,” *J. Biomed. Opt.*, vol. 12, no. 2, p. 024008, 2007, doi: 10.1117/1.2718934.
 - [105] K. Aubertin *et al.*, “Mesoscopic characterization of prostate cancer using Raman spectroscopy: potential for diagnostics and therapeutics,” *BJU Int.*, vol. 122, no. 2, pp. 326–336, 2018, doi: 10.1111/bju.14199.
 - [106] E. Vargis *et al.*, “Effect of normal variations on disease classification of Raman spectra from

- cervical tissue,” *Analyst*, vol. 136, no. 14, pp. 2981–2987, 2011, doi: 10.1039/c0an01020k.
- [107] E. Widjaja, W. Zheng, and Z. Huang, “Classification of colonic tissues using near-infrared Raman spectroscopy and support vector machines,” *Int. J. Oncol.*, vol. 32, no. 3, pp. 653–662, 2008, doi: 10.3892/ijo.32.3.653.
- [108] A. Beljebar *et al.*, “Identification of Raman spectroscopic markers for the characterization of normal and adenocarcinomatous colonic tissues,” *Crit. Rev. Oncol. Hematol.*, vol. 72, no. 3, pp. 255–264, 2009, doi: 10.1016/j.critrevonc.2009.09.004.
- [109] J. Desroches *et al.*, “Development and first in-human use of a Raman spectroscopy guidance system integrated with a brain biopsy needle,” *J. Biophotonics*, vol. 12, no. 3, pp. 1–7, 2019, doi: 10.1002/jbio.201800396.
- [110] S. Rubina, P. Sathe, T. K. Dora, S. Chopra, A. Maheshwari, and C. M. Krishna, “In vivo Raman spectroscopy of cervix cancers ,” *Opt. Biopsy XII*, vol. 8940, no. Vili, p. 89400E, 2014, doi: 10.1117/12.2033937.
- [111] R. Shaikh *et al.*, “In vivo Raman spectroscopy of human uterine cervix: exploring the utility of vagina as an internal control ,” *J. Biomed. Opt.*, vol. 19, no. 8, p. 087001, 2014, doi: 10.1117/1.jbo.19.8.087001.
- [112] J. Wang *et al.*, “Comparative study of the endoscope-based bevelled and volume fiber-optic Raman probes for optical diagnosis of gastric dysplasia in vivo at endoscopy,” *Anal. Bioanal. Chem.*, vol. 407, no. 27, 2015, doi: 10.1007/s00216-015-8727-x.
- [113] M. S. Bergholt *et al.*, “Real-time depth-resolved fiber optic Raman endoscopy for in vivo diagnosis of gastric precancer ,” *Biomed. Vib. Spectrosc. VI Adv. Res. Ind.*, vol. 8939, p. 89390M, 2014, doi: 10.1117/12.2039552.
- [114] M. S. Bergholt *et al.*, “Fiber-optic Raman spectroscopy probes gastric carcinogenesis in vivo at endoscopy,” *J. Biophotonics*, vol. 6, no. 1, pp. 49–59, 2013, doi: 10.1002/jbio.201200138.
- [115] H. C. McGregor *et al.*, “Real-time endoscopic Raman spectroscopy for in vivo early lung cancer detection,” *J. Biophotonics*, vol. 10, no. 1, pp. 98–110, 2017, doi: 10.1002/jbio.201500204.
- [116] H. C. McGregor, M. A. Short, S. Lam, T. Shaipanich, E. L. Beaudoin, and H. Zeng,

- “Development and in vivo test of a miniature Raman probe for early cancer detection in the peripheral lung,” *J. Biophotonics*, vol. 11, no. 11, pp. 1–4, 2018, doi: 10.1002/jbio.201800055.
- [117] H. Krishna, S. K. Majumder, P. Chaturvedi, M. Sidramesh, and P. K. Gupta, “In vivo Raman spectroscopy for detection of oral neoplasia: A pilot clinical study,” *J. Biophotonics*, vol. 7, no. 9, pp. 690–702, 2014, doi: 10.1002/jbio.201300030.
- [118] J. Schleusener *et al.*, “In vivo study for the discrimination of cancerous and normal skin using fibre probe-based Raman spectroscopy,” *Exp. Dermatol.*, vol. 24, no. 10, pp. 767–772, 2015, doi: 10.1111/exd.12768.
- [119] H. Lui, J. Zhao, D. McLean, and H. Zeng, “Real-time raman spectroscopy for in vivo skin cancer diagnosis,” *Cancer Res.*, vol. 72, no. 10, pp. 2491–2500, 2012, doi: 10.1158/0008-5472.CAN-11-4061.
- [120] L. Lim *et al.*, “Clinical study of noninvasive in vivo melanoma and nonmelanoma skin cancers using multimodal spectral diagnosis ,” *J. Biomed. Opt.*, vol. 19, no. 11, p. 117003, 2014, doi: 10.1111/1.jbo.19.11.117003.
- [121] V. P. Zakharov *et al.*, “Combined Raman spectroscopy and autofluorescence imaging method for in vivo skin tumor diagnosis ,” *Ultrafast Nonlinear Imaging Spectrosc. II*, vol. 9198, p. 919804, 2014, doi: 10.1117/12.2061667.
- [122] M. Pinto *et al.*, “Integration of a Raman spectroscopy system to a robotic-assisted surgical system for real-time tissue characterization during radical prostatectomy procedures,” *J. Biomed. Opt.*, vol. 24, no. 02, p. 1, 2019, doi: 10.1117/1.jbo.24.2.025001.
- [123] É. Lemoine *et al.*, “Feature engineering applied to intraoperative: In vivo Raman spectroscopy sheds light on molecular processes in brain cancer: A retrospective study of 65 patients,” *Analyst*, vol. 144, no. 22, pp. 6517–6532, 2019, doi: 10.1039/c9an01144g.
- [124] E. Beaulieu *et al.*, “Wide-field optical spectroscopy system integrating reflectance and spatial frequency domain imaging to measure attenuation-corrected intrinsic tissue fluorescence in radical prostatectomy specimens,” *Biomed. Opt. Express*, vol. 11, no. 4, p. 2052, 2020, doi: 10.1364/boe.388482.
- [125] P. Van Der Zee and M. Essenpreis, “Optical properties of brain tissue Pieter van der Zee,

Matthias Essenpreis, David, T. Delpy University of Hertfordshire, Dept. of Physics, Hatfield, Herts AL1O 9AB, UK University College London, Dept. of Medical Physics & Bioengineering, WC1E 6JA, UK,” *Library (Lond)*., vol. 1888, pp. 454–465, 1888.

- [126] A. N. Yaroslavsky, P. C. Schulze, I. V. Yaroslavsky, R. Schober, F. Ulrich, and H. J. Schwarzmaier, “Optical properties of selected native and coagulated human brain tissues in vitro in the visible and near infrared spectral range,” *Phys. Med. Biol.*, vol. 47, no. 12, pp. 2059–2073, 2002, doi: 10.1088/0031-9155/47/12/305.
- [127] A. Goyette, “Système d’imagerie d’optique diffuse hyperspectral intégré à une aiguille de biopsie neurochirurgicale afin d’en améliorer la sécurité,” École Polytechnique de Montréal, 2015.
- [128] C. Nimsky, A. Fujita, O. Ganslandt, B. Von Keller, and R. Fahlbusch, “Volumetric assessment of glioma removal by intraoperative high-field magnetic resonance imaging,” *Neurosurgery*, vol. 55, no. 2, pp. 358–370, 2004, doi: 10.1227/01.neu.0000129694.64671.91.
- [129] E. B. Claus *et al.*, “Survival rates in patients with low-grade glioma after intraoperative magnetic resonance image guidance,” *Cancer*, vol. 103, no. 6, pp. 1227–1233, 2005, doi: 10.1002/cncr.20867.
- [130] M. Lacroix *et al.*, “A multivariate analysis of 416 patients with glioblastoma multiforme: prognosis, extent of resection, and survival,” *J. Neurosurg.*, vol. 95, no. 2, pp. 190–198, Aug. 2001, doi: 10.3171/jns.2001.95.2.0190.
- [131] E. R. Laws, “Surgical management of intracranial gliomas—does radical resection improve outcome?,” 2003.
- [132] J. C. Buckner, “Factors Influencing Survival in High-Grade Gliomas,” *Semin. Oncol.*, vol. 30, no. 6 SUPPL. 19, pp. 10–14, 2003, doi: 10.1053/j.seminoncol.2003.11.031.
- [133] G. E. Keles, K. R. Lamborn, and M. S. Berger, “Low-grade hemispheric gliomas in adults: a critical review of extent of resection as a factor influencing outcome,” *J. Neurosurg.*, vol. 95, no. 5, pp. 735–745, Nov. 2001, doi: 10.3171/jns.2001.95.5.0735.
- [134] S. A. Yeh, J. T. Ho, C. C. Lui, Y. J. Huang, C. Y. Hsiung, and E. Y. Huang, “Treatment outcomes and prognostic factors in patients with supratentorial low-grade gliomas,” *Br. J.*

- Radiol.*, vol. 78, no. 927, pp. 230–235, 2005, doi: 10.1259/bjr/28534346.
- [135] J. P. Schneider *et al.*, “Gross-total surgery of supratentorial low-grade gliomas under intraoperative MR guidance,” *Am. J. Neuroradiol.*, vol. 22, no. 1, pp. 89–98, 2001.
- [136] R. Dammers, I. K. Haitsma, J. W. Schouten, J. M. Kros, C. J. J. Avezaat, and A. J. P. E. Vincent, “Safety and efficacy of frameless and frame-based intracranial biopsy techniques,” *Acta Neurochir. (Wien)*, vol. 150, no. 1, pp. 23–29, 2008, doi: 10.1007/s00701-007-1473-x.
- [137] M. D. Krieger, P. Chandrasoma, and M. L. J. Apuzzo, “Role of stereotactic biopsy in the diagnosis and management of brain tumors,” *Semin. Surg. Oncol.*, vol. 14, no. 1, pp. 13–25, 1998, doi: 10.1002/(sici)1098-2388(199801/02)14:1<13::aid-ssu3>3.0.co;2-5.
- [138] A. V. Kulkarni, A. Guha, A. Lozano, and M. Bernstein, “Incidence of silent hemorrhage and delayed deterioration after stereotactic brain biopsy,” *J. Neurosurg.*, vol. 89, no. 1, pp. 31–35, 1998, doi: 10.3171/jns.1998.89.1.0031.
- [139] M. Field, “Comprehensive assessment of hemorrhage risks and outcomes after stereotactic brain biopsy,” vol. 94, pp. 545–551, 2001.
- [140] R. Grossman, S. Sadetzki, R. Spiegelmann, and Z. Ram, “Haemorrhagic complications and the incidence of asymptomatic bleeding associated with stereotactic brain biopsies,” *Acta Neurochir. (Wien)*, vol. 147, no. 3, pp. 627–631, 2005, doi: 10.1007/s00701-005-0495-5.
- [141] D. Kondziolka, A. D. Firlik, and L. D. Lunsford, “Complications of stereotactic brain surgery,” *Neurol. Clin.*, vol. 16, no. 1, pp. 35–54, 1998, doi: 10.1016/S0733-8619(05)70366-2.
- [142] W. A. Hall, “The safety and efficacy of stereotactic biopsy for intracranial lesions,” *Cancer*, vol. 82, no. 9, pp. 1749–1755, 1998, doi: 10.1002/(SICI)1097-0142(19980501)82:9<1756::AID-CNCR23>3.0.CO;2-2.
- [143] L. D. Lunsford, A. Niranjan, A. A. Khan, and D. Kondziolka, “Establishing a benchmark for complications using frame-based stereotactic surgery,” *Stereotact. Funct. Neurosurg.*, vol. 86, no. 5, pp. 278–287, 2008, doi: 10.1159/000147636.
- [144] J. Tilgner, M. Herr, C. Ostertag, and B. Volk, “Validation of intraoperative diagnoses using

- smear preparations from stereotactic brain biopsies: Intraoperative versus final diagnosis - Influence of clinical factors," *Neurosurgery*, vol. 56, no. 2, pp. 257–263, 2005, doi: 10.1227/01.NEU.0000148899.39020.87.
- [145] D. B. P. D, A. J. M. M. D, N. O. Connorj, and T. H. Phd, "3-d reconstruction of blood vessels in the ocular fundus from confocal scanning laser ophthalmoscopeICG angiography," pp. 687–690, 1996.
- [146] L. Boni *et al.*, "Clinical applications of indocyanine green (ICG) enhanced fluorescence in laparoscopic surgery," *Surg. Endosc.*, vol. 29, no. 7, pp. 2046–2055, 2015, doi: 10.1007/s00464-014-3895-x.
- [147] A. Rühm, W. Göbel, R. Sroka, and H. Stepp, "ICG-assisted blood vessel detection during stereotactic neurosurgery: simulation study on excitation power limitations due to thermal effects in human brain tissue," *Photodiagnosis Photodyn. Ther.*, vol. 11, no. 3, pp. 307–318, 2014, doi: 10.1016/j.pdpdt.2014.03.007.
- [148] M. Hassan, A. Kerdok, A. Engel, K. Gersch, and J. M. Smith, "Near infrared fluorescence imaging with ICG in TECAB surgery using the da Vinci Si surgical system in a canine model," *J. Card. Surg.*, vol. 27, no. 2, pp. 158–162, 2012, doi: 10.1111/j.1540-8191.2011.01411.x.
- [149] Y. Rino *et al.*, "Visualization of blood supply route to the reconstructed stomach by indocyanine green fluorescence imaging during esophagectomy," *BMC Med. Imaging*, vol. 14, no. 1, 2014, doi: 10.1186/1471-2342-14-18.
- [150] J. de Moura, J. Novo, P. Charlón, N. Barreira, and M. Ortega, "Enhanced visualization of the retinal vasculature using depth information in OCT," *Med. Biol. Eng. Comput.*, vol. 55, no. 12, pp. 2209–2225, 2017, doi: 10.1007/s11517-017-1660-8.
- [151] S. Yang *et al.*, "OCT imaging detection of brain blood vessels in mouse, based on semiconducting polymer nanoparticles," *Analyst*, vol. 142, no. 23, pp. 4503–4510, 2017, doi: 10.1039/c7an01245d.
- [152] P. Gong *et al.*, "Optical coherence tomography for longitudinal monitoring of vasculature in scars treated with laser fractionation," *J. Biophotonics*, vol. 9, no. 6, pp. 626–636, 2016, doi: 10.1002/jbio.201500157.

- [153] D. Lorensen *et al.*, “Dual-modality needle probe for combined fluorescence imaging and three-dimensional optical coherence tomography,” *Opt. Lett.*, vol. 38, no. 3, p. 266, 2013, doi: 10.1364/ol.38.000266.
- [154] S. Onoda, “Preoperative identification of perforator vessels by combining MDCT, Doppler flowmetry, and ICG fluorescent angiography,” *Microsurgery*, pp. 504–506, 2009, doi: 10.1002/micr.
- [155] R. A. Leitgeb, L. Schmetterer, W. Drexler, A. F. Fercher, R. J. Zawadzki, and T. Bajraszewski, “Real-time assessment of retinal blood flow with ultrafast acquisition by color Doppler Fourier domain optical coherence tomography,” *Opt. Express*, vol. 11, no. 23, p. 3116, 2003, doi: 10.1364/oe.11.003116.
- [156] H. Ramakonar *et al.*, “Intraoperative detection of blood vessels with an imaging needle during neurosurgery in humans,” *Sci. Adv.*, vol. 4, no. 12, pp. 1–11, 2018, doi: 10.1126/sciadv.aav4992.
- [157] C.-P. Liang *et al.*, “Coherence-gated Doppler: a fiber sensor for precise localization of blood flow,” *Biomed. Opt. Express*, vol. 4, no. 5, p. 760, 2013, doi: 10.1364/boe.4.000760.
- [158] V. Rajan, B. Varghese, T. G. Van Leeuwen, and W. Steenbergen, “Review of methodological developments in laser Doppler flowmetry,” *Lasers Med. Sci.*, vol. 24, no. 2, pp. 269–283, 2009, doi: 10.1007/s10103-007-0524-0.
- [159] K. Wårdell, S. Hemm-Ode, P. Rejmstad, and P. Zsigmond, “High-Resolution Laser Doppler Measurements of Microcirculation in the Deep Brain Structures: A Method for Potential Vessel Tracking,” *Stereotact. Funct. Neurosurg.*, vol. 94, no. 1, pp. 1–9, 2016, doi: 10.1159/000442894.
- [160] V. Virdyawan, M. Oldfield, and F. Rodriguez Y Baena, “Laser Doppler sensing for blood vessel detection with a biologically inspired steerable needle,” *Bioinspiration and Biomimetics*, vol. 13, no. 2, 2018, doi: 10.1088/1748-3190/aaa6f4.
- [161] M. A. Davis, L. Gagnon, D. A. Boas, and A. K. Dunn, “Sensitivity of laser speckle contrast imaging to flow perturbations in the cortex,” *Biomed. Opt. Express*, vol. 7, no. 3, p. 759, 2016, doi: 10.1364/boe.7.000759.
- [162] K. Basak, M. Manjunatha, and P. K. Dutta, “Review of laser speckle-based analysis in

- medical imaging,” *Med. Biol. Eng. Comput.*, vol. 50, no. 6, pp. 547–558, 2012, doi: 10.1007/s11517-012-0902-z.
- [163] J. Pichette *et al.*, “Sensitivity analysis aimed at blood vessels detection using interstitial optical tomography during brain needle biopsy procedures,” *Biomed. Opt. Express*, vol. 6, no. 11, 2015, doi: 10.1364/BOE.6.004238.
- [164] P. Van Der Zee and M. Essenpreis, “Optical properties of brain tissue Pieter van der Zee, Matthias Essenpreis, David, T. Delphy University of Hertfordshire, Dept. of Physics, Hatfield, Herts AL1O 9AB, UK University College London, Dept. of Medical Physics & Bioengineering, WC1E 6JA, UK,” *Library (Lond.)*, vol. 1888, no. May 2012, pp. 454–465, 1888.
- [165] D. A. Boas, J. P. Culver, J. J. Stott, and A. K. Dunn, “Three dimensional Monte Carlo code for photon migration through complex heterogeneous media including the adult human head,” *Opt. Express*, vol. 10, no. 3, p. 159, 2002, doi: 10.1364/oe.10.000159.
- [166] Q. Fang and D. Boas, “Tetrahedral mesh generation from volumetric binary and gray-scale images,” شفافیت، شفافیت، vol. 2009, no. شفافیت، شفافیت، p. 2009, doi: 10.1038/132817a0.
- [167] S. Prahl, “Optical absorption of hemoglobin. Oregon Medical Laser Center.” <http://omlc.ogi.edu/spectra/hemoglobin/index.html>.
- [168] Michael Mastanduno, “Combined MRI and Near-Infrared spectroscopy for increased specificity of breast cancer imaging,” 2016.
- [169] T. Phantoms, P. Di Ninni, F. Martelli, and G. Zaccanti, “Intralipid: Towards a diffusive reference standard for optical,” *Phys. Med. Biol.*, vol. 56, no. 2, 2011, doi: 10.1088/0031-9155/56/2/N01.
- [170] I. Wolf *et al.*, “The medical imaging interaction toolkit,” *Med. Image Anal.*, vol. 9, no. 6, pp. 594–604, 2005, doi: 10.1016/j.media.2005.04.005.
- [171] J. Desroches *et al.*, “A new method using Raman spectroscopy for in vivo targeted brain cancer tissue biopsy,” *Sci. Rep.*, vol. 8, no. 1, 2018, doi: 10.1038/s41598-018-20233-3.
- [172] J. Desroches *et al.*, “Development and first in-human use of a Raman spectroscopy guidance system integrated with a brain biopsy needle,” *J. Biophotonics*, vol. 12, no. 3, 2019, doi:

10.1002/jbio.201800396.

- [173] I. P. Santos *et al.*, “Raman spectroscopy for cancer detection and cancer surgery guidance : translation to the clinics,” pp. 3025–3047, 2017, doi: 10.1039/c7an00957g.
- [174] R. Shams *et al.*, “Pre-clinical evaluation of an image-guided in-situ Raman spectroscopy navigation system for targeted prostate cancer interventions,” *Int. J. Comput. Assist. Radiol. Surg.*, vol. 15, no. 5, 2020, doi: 10.1007/s11548-020-02136-9.
- [175] M. S. Bergholt *et al.*, “Combining near-infrared-excited autofluorescence and Raman spectroscopy improves in vivo diagnosis of gastric cancer,” *Biosens. Bioelectron.*, vol. 26, no. 10, pp. 4104–4110, 2011, doi: 10.1016/j.bios.2011.04.005.
- [176] M. S. Bergholt *et al.*, “Characterizing variability in in vivo Raman spectra of different anatomical locations in the upper gastrointestinal tract toward cancer detection,” *J. Biomed. Opt.*, vol. 16, no. 3, p. 037003, 2011, doi: 10.1117/1.3556723.
- [177] M. S. Bergholt *et al.*, “In vivo diagnosis of gastric cancer using Raman endoscopy and ant colony optimization techniques,” *Int. J. Cancer*, vol. 128, no. 11, pp. 2673–2680, 2011, doi: 10.1002/ijc.25618.
- [178] Z. Huang *et al.*, “In vivo detection of epithelial neoplasia in the stomach using image-guided Raman endoscopy,” *Biosens. Bioelectron.*, vol. 26, no. 2, pp. 383–389, 2010, doi: 10.1016/j.bios.2010.07.125.
- [179] M. S. Bergholt *et al.*, “Raman endoscopy for in vivo differentiation between benign and malignant ulcers in the stomach,” *Analyst*, vol. 135, no. 12, pp. 3162–3168, 2010, doi: 10.1039/c0an00336k.
- [180] S. P. Singh, A. Sahu, A. Deshmukh, P. Chaturvedi, and C. M. Krishna, “In vivo raman spectroscopy of oral buccal mucosa: A study on malignancy associated changes (MAC)/cancer field effects (CFE),” *Analyst*, vol. 138, no. 14, pp. 4175–4182, 2013, doi: 10.1039/c3an36761d.
- [181] M. Jermyn *et al.*, “Neural networks improve brain cancer detection with Raman spectroscopy in the presence of operating room light artifacts,” *J. Biomed. Opt.*, vol. 21, no. 9, p. 094002, 2016, doi: 10.1117/1.jbo.21.9.094002.

- [182] M. Jermyn *et al.*, “Raman spectroscopy detects distant invasive brain cancer cells centimeters beyond MRI capability in humans,” *Biomed. Opt. Express*, vol. 7, no. 12, p. 5129, 2016, doi: 10.1364/boe.7.005129.
- [183] T. Bhattacharjee, L. C. Fontana, L. Raniero, and J. Ferreira, “In vivo Raman spectroscopy of breast tumors prephotodynamic and postphotodynamic therapy,” no. February, pp. 1–6, 2018, doi: 10.1002/jrs.5360.
- [184] K. St-Arnaud *et al.*, “Wide-field spontaneous Raman spectroscopy imaging system for biological tissue interrogation,” *Opt. Lett.*, vol. 41, no. 20, p. 4692, 2016, doi: 10.1364/ol.41.004692.
- [185] K. St-arnaud, Q. C. Hx, and K. Petrecca, “Development and characterization of a handheld hyperspectral Raman imaging probe system for molecular characterization of tissue on mesoscopic scales,” vol. 45, no. January, pp. 328–339, 2018, doi: 10.1002/mp.12657.
- [186] A. Akbarzadeh *et al.*, “Experimental validation of a spectroscopic Monte Carlo light transport simulation technique and Raman scattering depth sensing analysis in biological tissue,” *J. Biomed. Opt.*, vol. 25, no. 10, pp. 1–19, 2020, doi: 10.1117/1.jbo.25.10.105002.
- [187] A. Shoji, T. Ozaki, T. Fujito, K. Deguchi, S. Ando, and I. Ando, “Raman Spectroscopic Characterization and Molecular Force Field Development of a Synthetic Polyamide: Nylon 66,” pp. 2863–2867, 1989.
- [188] F. Dallaire *et al.*, “Quantitative spectral quality assessment technique validated using intraoperative in vivo Raman spectroscopy measurements,” *J. Biomed. Opt.*, vol. 25, no. 4, 2020, doi: 10.1117/1.JBO.25.4.040501.
- [189] R. Perez-pueyo, M. J. Soneira, and S. Ruiz-moreno, “Morphology-Based Automated Baseline Removal for Raman Spectra of Artistic Pigments,” vol. 64, no. 6, pp. 595–600, 2010.
- [190] P. LeCacheux and G. Menard, “Quantitative Analysis of Cholesterol and Cholesterol Ester Mixtures Using Near-Infrared Fourier Transform Raman Spectroscopy,” vol. 50, no. 10, pp. 1253–1257, 1996.
- [191] A. Chandra and S. Talari, “Raman Spectroscopy of Biological Tissues,” pp. 46–111, 2015, doi: 10.1080/05704928.2014.923902.

- [192] M. Jové, I. Pradas, M. Dominguez-Gonzalez, I. Ferrer, and R. Pamplona, “Lipids and lipoxidation in human brain aging. Mitochondrial ATP-synthase as a key lipoxidation target,” *Redox Biol.*, vol. 23, no. October 2018, p. 101082, 2019, doi: 10.1016/j.redox.2018.101082.
- [193] C. Cortes, “Support-Vector Networks,” vol. 297, pp. 273–297, 1995.
- [194] J. S. O. Brien and E. L. Sampson, “Lipid composition of the normal human brain ;,” vol. 6, no. 9, 1965.
- [195] F. Daoust *et al.*, “Handheld macroscopic Raman spectroscopy imaging instrument for machine-learning-based molecular tissue margins characterization,” *J. Biomed. Opt.*, vol. 26, no. 02, pp. 1–18, 2021, doi: 10.1117/1.jbo.26.2.022911.
- [196] H. Sung *et al.*, “Global Cancer Statistics 2020: GLOBOCAN Estimates of Incidence and Mortality Worldwide for 36 Cancers in 185 Countries,” *CA. Cancer J. Clin.*, vol. 71, no. 3, pp. 209–249, 2021, doi: 10.3322/caac.21660.
- [197] A. Heidenreich *et al.*, “EAU Guidelines on Prostate Cancer,” *Eur. Urol.*, vol. 53, no. 1, pp. 68–80, 2008, doi: 10.1016/j.eururo.2007.09.002.
- [198] J. C. Presti, “Prostate cancer: Assessment of risk using digital rectal examination, tumor grade, prostate-specific antigen, and systematic biopsy,” *Radiol. Clin. North Am.*, vol. 38, no. 1, pp. 49–58, 2000, doi: 10.1016/s0033-8389(05)70149-4.
- [199] G. Fichtinger, A. Krieger, R. C. Susil, A. Tanacs, L. L. Whitcomb, and E. Atalar, “Transrectal prostate biopsy inside closed mri scanner with remote actuation, under real-time image guidance,” *Lect. Notes Comput. Sci. (including Subser. Lect. Notes Artif. Intell. Lect. Notes Bioinformatics)*, vol. 2488, pp. 91–98, 2002, doi: 10.1007/3-540-45786-0_12.
- [200] L. Wei *et al.*, “Intratumoral and Intertumoral Genomic Heterogeneity of Multifocal Localized Prostate Cancer Impacts Molecular Classifications and Genomic Prognosticators,” *Eur. Urol.*, vol. 71, no. 2, pp. 183–192, 2017, doi: 10.1016/j.eururo.2016.07.008.
- [201] P. C. Boutros *et al.*, “Spatial genomic heterogeneity within localized, multifocal prostate cancer,” *Nat. Genet.*, vol. 47, no. 7, pp. 736–745, 2015, doi: 10.1038/ng.3315.

- [202] David Grajales *et al.*, “Image-guided Raman spectroscopy navigation system to improve transperineal prostate cancer detection. Part 2: In-vivo tumor-targeting using a classification model combining spectral and MRI-radiomics features.,” *J. Biomed. Opt.*, 2022.
- [203] A. Fedorov *et al.*, “3D Slicer as an image computing platform for the Quantitative Imaging Network,” *Magn. Reson. Imaging*, vol. 30, no. 9, pp. 1323–1341, 2012, doi: 10.1016/j.mri.2012.05.001.
- [204] C. C. Compton, *A Companion to the Seventh Editions of the AJCC Cancer Staging Manual and Handbook*. 2012.
- [205] H. Samaratunga *et al.*, “International society of urological pathology (ISUP) consensus conference on handling and staging of radical prostatectomy specimens. working group 1: Specimen handling,” *Mod. Pathol.*, vol. 24, no. 1, pp. 6–15, 2011, doi: 10.1038/modpathol.2010.178.
- [206] S. S. Kumar and T. Shaikh, “Empirical Evaluation of the Performance of Feature Selection Approaches on Random Forest,” *2017 Int. Conf. Comput. Appl. ICCA 2017*, pp. 227–231, 2017, doi: 10.1109/COMAPP.2017.8079769.
- [207] J. K. Jaiswal and R. Samikannu, “Application of Random Forest Algorithm on Feature Subset Selection and Classification and Regression,” *Proc. - 2nd World Congr. Comput. Commun. Technol. WCCCT 2017*, pp. 65–68, 2017, doi: 10.1109/WCCCT.2016.25.
- [208] D. K. R. Medipally *et al.*, “Vibrational spectroscopy of liquid biopsies for prostate cancer diagnosis,” *Ther. Adv. Med. Oncol.*, vol. 12, pp. 1–23, 2020, doi: 10.1177/1758835920918499.
- [209] D. W. Jeong, S. Lee, and Y. S. Chun, “How cancer cells remodel lipid metabolism: strategies targeting transcription factors,” *Lipids Health Dis.*, vol. 20, no. 1, pp. 1–19, 2021, doi: 10.1186/s12944-021-01593-8.
- [210] C. J. D. Wallis and R. K. Nam, “Prostate Cancer Genetics: A Review.,” *Ejifcc*, vol. 26, no. 2, pp. 79–91, 2015, [Online]. Available: <http://www.ncbi.nlm.nih.gov/pubmed/27683484%0Ahttp://www.ncbi.nlm.nih.gov/entrez/eutils/efetch.fcgi?artid=PMC4975354>.
- [211] S. Benafif and R. Eeles, “Genetic predisposition to prostate cancer,” *Br. Med. Bull.*, vol.

- 120, no. 1, pp. 75–89, 2016, doi: 10.1093/bmb/ldw039.
- [212] K. A. Cooney, “Inherited Predisposition to Prostate Cancer: From Gene Discovery to Clinical Impact,” *Trans. Am. Clin. Climatol. Assoc.*, vol. 128, pp. 14–23, 2017.
- [213] S. Benafif, Z. Kote-Jarai, and R. A. Eeles, “A review of prostate cancer Genome-Wide Association Studies (GWAS),” *Cancer Epidemiol. Biomarkers Prev.*, vol. 27, no. 8, pp. 845–857, 2018, doi: 10.1158/1055-9965.EPI-16-1046.
- [214] P. Gao *et al.*, “Biology and Clinical Implications of the 19q13 Aggressive Prostate Cancer Susceptibility Locus,” *Cell*, vol. 174, no. 3, pp. 576–589.e18, 2018, doi: 10.1016/j.cell.2018.06.003.
- [215] C. H. Liu *et al.*, “Resonance Raman and Raman spectroscopy for breast cancer detection,” *Technol. Cancer Res. Treat.*, vol. 12, no. 4, pp. 371–382, 2013, doi: 10.7785/tcrt.2012.500325.
- [216] X. Yang *et al.*, “Diagnosis of Lung Cancer by ATR-FTIR Spectroscopy and Chemometrics,” *Front. Oncol.*, vol. 11, no. September, pp. 1–7, 2021, doi: 10.3389/fonc.2021.753791.
- [217] S. Sato *et al.*, “All-in-one Raman spectroscopy approach to diagnosis of colorectal cancer: analysis of spectra in the fingerprint regions,” *J. Anus, Rectum Colon*, vol. 3, no. 2, pp. 84–90, 2019, doi: 10.23922/jarc.2018-039.
- [218] A. Ghita, P. Matousek, and N. Stone, “Sensitivity of Transmission Raman Spectroscopy Signals to Temperature of Biological Tissues,” *Sci. Rep.*, vol. 8, no. 1, pp. 1–7, 2018, doi: 10.1038/s41598-018-25465-x.
- [219] M. Z. Vardaki *et al.*, “Defocused Spatially Offset Raman Spectroscopy in Media of Different Optical Properties for Biomedical Applications Using a Commercial Spatially Offset Raman Spectroscopy Device,” *Appl. Spectrosc.*, vol. 74, no. 2, pp. 223–232, 2020, doi: 10.1177/0003702819884625.

ANNEXE A CURRICULUM VITAE

Cheminement Universitaire

2017-	<p>Doctorat Génie Biomédical</p> <p>Directeur Frédéric Leblond, Co-directeur Samuel Kadoury</p> <p>Polytechnique Montréal (Montréal QC, Canada)</p>
2012-2016	<p>Diplôme CentraleSupélec</p> <p>Cursus ingénieur Supélec</p> <p>CentraleSupélec (91 Gif-sur-Yvette, France)</p>
2010-2012	<p>Classe préparatoire aux grandes écoles, filière MPSI/MP</p> <p>Lycée Pierre de Fermat (31 Toulouse, France)</p>

Expérience Enseignement Polytechnique Montréal (Montréal QC, Canada)

2018-2021	<p>Encadrant PHS8972 Projet intégrateur final en génie physique</p> <p>Projet 2 : “Développement d’un endoscope Raman basé sur un matériau guide d’onde sans signal de Background”</p> <p>Projet 1 : “Détection et quantification de sang stagnant en contexte opératoire”</p>
2018-2019	<p>Encadrant PHS9870 Projet intégrateur final en génie biomédical</p> <p>Projet : “Conception d’un montage expérimental démontrant la spectroscopie Raman et de fluorescence résolue en temps”</p>

2018-2020	Assistant chargé de laboratoire et correcteur PHS2223 Introduction à l'optique moderne
2016-2017	Chargé de cours de travaux dirigés PHS1101 Mécanique pour ingénieur
2015-2017	Répétiteur et correcteur PHS1101 Mécanique pour ingénieur

Expérience professionnelle

2014	Stage ingénieur. Mise en place d'une station électromécanique de test, évaluation de moteurs pour équipement aéronautique embarqué. Air Support, 32 Pujaudran, France.
2013	Stage ouvrier. Mise au point qualité (réparation/rattrapage), usine d'assemblage de l'A380. Groupe européen Airbus, 31 Blagnac, France.

Bourses et prix

2019-2021	Bourse Canderel – Doctorat – Institut du Cancer de Montréal (10000 CAD/an)
2017	Bourse de voyage – Doctorat – Défi CRChum (700 CAD)
2015	Bourse étudiante du GRSTB - Groupe de Recherche en Sciences et Technologies Biomédicales (9000 CAD)
2010-2013	Bourse au mérite du CROUS - Centre Régional des Œuvres Universitaires et Scolaires sous la tutelle du Ministère de l'Enseignement Supérieur et de la Recherche. (1800 euros/an)

Publications

Grajales, D., **Picot, F.**, Shams, R., Dallaire, F., Sheehy, G., Alley, S., ... & Kadoury, S. (2022) Image-guided Raman spectroscopy navigation system to improve transperineal prostate cancer detection. Part 2: In-vivo tumor-targeting using a classification model combining spectral and MRI-radiomics features., *Journal of biomedical optics*.

Picot, F., Shams, R., Dallaire, F., Sheehy, G., Tran, T., Grajales, D., ... & Leblond, F. (2022) Image-guided Raman spectroscopy navigation system to improve transperineal prostate cancer detection. Part 1: Raman spectroscopy fiber-optics system and *in situ* tissue characterization., *Journal of biomedical optics*.

Picot, F., Daoust, F., Sheehy, G., Dallaire, F., Chaikho, L., Bégin, T., ... & Leblond, F. (2020) Data consistency and classification model transferability across biomedical Raman spectroscopy systems. *Translational Biophotonics*, e202000019.

Shams, R., **Picot, F.**, Grajales, D., Sheehy, G., Dallaire, F., Birlea, M., ... & Kadoury, S. (2020). Pre-clinical evaluation of an image-guided in-situ Raman spectroscopy navigation system for targeted prostate cancer interventions. *International journal of computer assisted radiology and surgery*, 15(5), 867-876.

Dallaire, F., **Picot, F.**, Tremblay, J. P., Sheehy, G., Lemoine, É., Agarwal, R., ... & Leblond, F. (2020). Quantitative spectral quality assessment technique validated using intraoperative in vivo Raman spectroscopy measurements. *Journal of biomedical optics*, 25(4), 040501.

Picot, F., Goyette, A., Obaid, S., Desroches, J., Lessard, S., Tremblay, M. A., ... & Leblond, F. (2019). Interstitial imaging with multiple diffusive reflectance spectroscopy projections for in vivo blood vessels detection during brain needle biopsy procedures. *Neurophotonics*, 6(2), 025003.

Desroches, J., Jermyn, M., Pinto, M., **Picot, F.**, Tremblay, M. A., Obaid, S., ... & Leblond, F. (2018). A new method using Raman spectroscopy for in vivo targeted brain cancer tissue biopsy. *Scientific reports*, 8(1), 1-10.

Pichette, J., Goyette, A., **Picot, F.**, Tremblay, M. A., Soulez, G., Wilson, B. C., & Leblond, F. (2015). Sensitivity analysis aimed at blood vessels detection using interstitial optical tomography during brain needle biopsy procedures. *Biomedical optics express*, 6(11), 4238-4254.

Conférences

Picot, F., Shams, R., Dallaire, F., Sheehy, G., Grajales, D., Ménard, C., ... & Leblond, F. (2022, June). Human in vivo prostate tumor-targeting using a Raman spectroscopy probe and electromagnetic tracking (Conference Presentation). The International Society for Clinical Spectroscopy.

Picot, F., Sheehy, G., Dallaire, F., Tremblay, J. P., Daoust, F., Lemoine, É., ... & Leblond, F. (2020, April). Data compatibility across point probe Raman spectroscopy systems and its impact on statistical models portability (Conference Presentation). In Clinical Biophotonics (Vol. 11362, p. 113620F). International Society for Optics and Photonics.

Desroches, J., Jermyn, M., Pinto, M., **Picot, F.**, Tremblay, M. A., Obaid, S., ... & Leblond, F. (2017, April). High wavenumber Raman spectroscopy to improve diagnostic yield of brain needle biopsies. In Optics and the Brain (pp. BrW4B-7). Optical Society of America.

Shams, R., **Picot, F.**, Sheehy, G., Menard, C., Carrier, J. F., Leblond, F., & Kadoury, S. EM navigation of a Raman spectroscopy needle for prostate cancer confirmation: Preliminary ex-vivo study in 3D Slicer★.

Picot, F., Goyette, A., Pichette, J., Tremblay, M. A., Desroches, J., Obaid, S., ... & Leblond, F. (2018, April). Diffusive Reflectance Spectroscopy to Enhance Safety during Brain Biopsy Procedure. In Optical Tomography and Spectroscopy (pp. OW4C-6). Optical Society of America.

Picot, F., Pichette, J., Desroches, J., Goyette, A., Tremblay, M. A., Ben-Mansour, Y., ... & Wilson, B. C. (2016, May). Imaging system based on diffusive reflectance spectroscopy for blood vessels detection during brain biopsy procedure. In 2016 Photonics North (PN) (pp. 1-1). IEEE.